

# **SANDIA REPORT**

SAND2001-1631  
Unlimited Release  
Printed June 2001

## **Ribbon Surface Pressure and Wake Velocity Data for the Experimental Validation of a Vortex-Based Parachute Inflation Code**

Donald D. McBride, Edward L. Clark, and John F. Henfling

Prepared by  
Sandia National Laboratories  
Albuquerque, New Mexico 87185 and Livermore, California 94550

Sandia is a multiprogram laboratory operated by Sandia Corporation,  
a Lockheed Martin Company, for the United States Department of  
Energy under Contract DE-AC04-94AL85000.

Approved for public release; further dissemination unlimited.



**Sandia National Laboratories**

Issued by Sandia National Laboratories, operated for the United States Department of Energy by Sandia Corporation.

**NOTICE:** This report was prepared as an account of work sponsored by an agency of the United States Government. Neither the United States Government, nor any agency thereof, nor any of their employees, nor any of their contractors, subcontractors, or their employees, make any warranty, express or implied, or assume any legal liability or responsibility for the accuracy, completeness, or usefulness of any information, apparatus, product, or process disclosed, or represent that its use would not infringe privately owned rights. Reference herein to any specific commercial product, process, or service by trade name, trademark, manufacturer, or otherwise, does not necessarily constitute or imply its endorsement, recommendation, or favoring by the United States Government, any agency thereof, or any of their contractors or subcontractors. The views and opinions expressed herein do not necessarily state or reflect those of the United States Government, any agency thereof, or any of their contractors.

Printed in the United States of America. This report has been reproduced directly from the best available copy.

Available to DOE and DOE contractors from  
U.S. Department of Energy  
Office of Scientific and Technical Information  
P.O. Box 62  
Oak Ridge, TN 37831

Telephone: (865)576-8401  
Facsimile: (865)576-5728  
E-Mail: [reports@adonis.osti.gov](mailto:reports@adonis.osti.gov)  
Online ordering: <http://www.doe.gov/bridge>

Available to the public from  
U.S. Department of Commerce  
National Technical Information Service  
5285 Port Royal Rd  
Springfield, VA 22161

Telephone: (800)553-6847  
Facsimile: (703)605-6900  
E-Mail: [orders@ntis.fedworld.gov](mailto:orders@ntis.fedworld.gov)  
Online order: <http://www.ntis.gov/ordering.htm>



SAND2001-1631  
Unlimited Release  
Printed June 2001

# **Ribbon Surface Pressure and Wake Velocity Data for the Experimental Validation of a Vortex-Based Parachute Inflation Code**

Donald D. McBride and Edward L. Clark, Consultants  
and

John F. Henfling  
Thermal/Fluid Experimental Sciences Department  
Sandia National Laboratories  
Albuquerque, New Mexico 87185-0834

## **ABSTRACT**

An experiment to measure surface pressure data on a series of three stainless steel simulated parachute ribbons was conducted. During the first phase of the test, unsteady pressure measurements were made on the windward and leeward sides of the ribbons to determine the statistical properties of the surface pressures. Particle Image Velocimetry (PIV) measurements were simultaneously made to establish the velocity field in the wake of the ribbons and its correlation with the pressure measurements. In the second phase of the test, steady-state pressure measurements were made to establish the pressure distributions. In the third phase, the stainless steel ribbons were replaced with nylon ribbons and PIV measurements were made in the wake.

A detailed error analysis indicates that the accuracy of the pressure measurements was very good. However, an anomaly in the flow field caused the wake behind the stainless steel ribbons to establish itself in a stable manner on one side of the model. This same stability was not present for the nylon ribbon model although an average of the wake velocity data indicated an apparent 2° upwash in the wind tunnel flow field. Since flow angularity upstream of the model was not measured, the use of the data for code validation is not recommended without a second experiment to establish that upstream boundary condition.

## **ACKNOWLEDGEMENTS**

The authors would like to thank the U.S. Army and Dr. James Ross and NASA for making their 7- x 10- Foot, Subsonic Wind Tunnel Number 1 available for us to use in this experiment and for providing an experienced and very capable crew to operate it. We also want to acknowledge the contributions of J. T. Heineck and Dr. Steve Walker for their expertise in setting up and operating the PIV equipment.

We would also like to thank Dr. Walter Wolfe for monitoring the experiment as project manager and for reviewing the manuscript and Dr. Carl Peterson for reviewing the manuscript.

This report was written under Sandia Contracts 5980 and 6074.

## TABLE OF CONTENTS

Nomenclature .....	x
Introduction .....	1
Experiment .....	4
Pressure Model .....	4
Tunnel Installation .....	7
Instrumentation, Data Acquisition, and Data Reduction .....	13
Unsteady Pressure Measurements .....	13
Steady-State Pressure Measurements .....	16
Experimental Uncertainty .....	17
Measurement Uncertainty .....	17
Uncertainty from Flow Dynamics .....	18
Uncertainties in Model Alignment .....	19
Results .....	23
Unsteady Pressure Measurements .....	23
Particle Image Velocimetry Measurements .....	27
Steady-State Pressure Measurements .....	41
Recommendations .....	44
References .....	45
Appendix A – Calculation of Pressure Coefficient, $C_p$ .....	A-1
References .....	A-6
Appendix B – Estimation of Averaging Time .....	B-1
References .....	B-10
Appendix C – Calculation of the Power Spectral Density Function .....	C-1
References .....	C-4
Appendix D – Time-Accurate Pressure Reconstruction .....	D-1
Pressure Reconstruction Using a Transfer Function .....	D-1
Experimental Determination of Transfer Function .....	D-1
Proof of Principle Test .....	D-5
References .....	D-10
Appendix E – Test Conditions .....	E-1
Unsteady Pressure Runs .....	E-1
Steady-State Pressure Runs .....	E-2

Appendix F – Measurement Uncertainty Analysis .....	F-1
Nominal Test Conditions.....	F-2
Differential Pressure Errors (Endevco Transducers) .....	F-3
Calibration error .....	F-3
Zero shifts .....	F-3
Transducer error .....	F-4
Tunnel Freestream Conditions Calibration Errors (Endevco Transducers).....	F-6
Differential Pressure Errors (PSI System) .....	F-8
Calibration error .....	F-8
Zero shifts .....	F-8
Transducer error .....	F-8
Tunnel Freestream Conditions Calibration Errors (PSI System) .....	F-9
Propagation of Error—Pressure Coefficient, $C_p$ .....	F-13
Evaluation—Endevco transducers.....	F-14
Evaluation—PSI system.....	F-15
Propagation of Error—Test Conditions .....	F-15
Dynamic pressure .....	F-15
Static Pressure and Velocity .....	F-16
Evaluation—Endevco transducers.....	F-17
Evaluation—PSI system.....	F-17
Reconstruction Errors.....	F-17
Bibliography.....	F-18
References.....	F-19

## LIST OF FIGURES

1. Cross-section of stainless steel ribbon at centerline.....	4
2. Pressure port identification.....	5
3. Pre-test sketch of tunnel installation.....	8
4. Photograph of tunnel installation.....	9
5. Spring-loaded compression fixture for tensioning ribbons .....	10
6. Photograph of pressure transducer connections on outside surface of splitter plate.....	11
7. Photograph of windshield covering pressure transducers and connections.....	12
8. Center ribbon windward pressure distribution in 2-1-3 vs. 1-2-3 configurations.....	19
9. Tension effects on ribbon deflection under 100 ft/s wind load .....	20
10. Ribbon misalignment with ribbons in 2-1-3 configuration .....	21
11. Ribbon misalignment with ribbons in 1-2-3 configuration .....	22
12. Typical time-accurate pressures on windward side (Run 19).....	25
13. Typical Power Spectral Density (PSD) of pressure on windward side (Port 22, Run 19).....	26
14. Velocity field measured with PIV system ( $t = 0.125$ s, Run 19).....	29
15. Vorticity field measured with PIV system ( $t = 0.125$ s, Run 19) .....	30
16. Average velocity field measured with PIV system (average of 100 fields – Run 19) .....	31
17. Average vorticity field measured with PIV system (average of 100 fields – Run 19) .....	32
18. Dynamic pressure distribution on tunnel centerline with model installed.....	33
19. Average velocity field behind fabric ribbons tensioned to 600 lb total tension.....	35
20. Average velocity field behind fabric ribbons tensioned to 640 lb total tension.....	36
21. Average velocity field behind fabric ribbons tensioned to 680 lb total tension.....	37
22a. Velocity field behind fabric ribbons tensioned to 600 lb ( $t \approx 0.125$ s).....	38
22b. Velocity field behind fabric ribbons tensioned to 600 lb ( $t \approx 0.193$ s).....	39
22c. Velocity field behind fabric ribbons tensioned to 600 lb ( $t \approx 0.260$ s).....	40
23. Comparison of steady-state (PSI) with averaged unsteady (Endevco) $C_p$ 's at a nominal velocity of 80 ft/s.....	42
24. Comparison of steady-state (PSI) with averaged unsteady (Endevco) $C_p$ 's at a nominal velocity of 100 ft/s.....	43
Appendix A	
A-1. Endevco pitot-static tube static pressure calibration.....	A-2

A-2	Endevco pitot-static tube dynamic pressure calibration.....	A-2
A-3	PSI pitot-static tube static pressure calibration .....	A-3
A-4	PSI pitot-static tube dynamic pressure calibration.....	A-3
Appendix B		
B-1	Autocorrelation function, center ribbon, windward ports, Run 9.....	B-3
B-2	Average normalized autocorrelation function, center ribbon, windward ports .....	B-3
B-3	Autocorrelation function, center ribbon, leeward ports, Run 9 .....	B-4
B-4	Average normalized autocorrelation function, center ribbon, leeward ports.....	B-4
B-5	Standard deviation reduction ratio.....	B-5
B-6	Relative error in the mean .....	B-7
B-7	Autocorrelation function for $p_r - p_{sr}$ , Run 9 .....	B-9
B-8	Normalized autocorrelation function for $p_r - p_{sr}$ .....	B-9
Appendix C		
C-1	Hanning weights.....	C-2
Appendix D		
D-1	Schematic of setup for transfer function determination .....	D-2
D-2	Experimentally determined transfer function.....	D-4
D-3	Schematic of experimental setup for proof of principle test .....	D-5
D-4	Reconstruction of pressure during initial moments of positive bias proof of principle test .....	D-7
D-5	Reconstruction of pressure during final moments of positive bias proof of principle test .....	D-8
D-6	Power spectral density for positive bias proof of principle test.....	D-9
D-7	Correlation of error with pressure level for positive bias proof of principle test.....	D-9

## LIST OF TABLES

1.	Pressure Port Locations.....	6
2.	Uncertainty Summary ( $V = 100$ ft/s).....	17
3.	Uncertainty from Flow Dynamics.....	18
4.	Run Schedule for Stainless Steel Ribbons.....	24
5.	Run Schedule for Nylon Ribbons with PIV .....	34
Appendix A		
A-1	Test Conditions Calibration Factors.....	A-4
Appendix B		
B-1	Standardized Normal Random Variable.....	B-6
B-2	$C_p$ Statistics, Center Ribbon, $V = 100$ ft/s.....	B-6
B-3	Relative Uncertainty in $\bar{C}_p$ .....	B-7
B-4	Standard Deviation Reduction Ratios .....	B-10
Appendix C		
C-1.	Confidence Limits on $S_{xx}$ .....	C-3
Appendix D		
D-1	Reconstruction Error Summary.....	D-6
Appendix E		
E-1.	Unsteady Pressure Runs.....	E-1
E-2	Average Test Conditions for Unsteady Pressure Runs.....	E-2
E-3	Steady-State Pressure Runs.....	E-2
E-4	Average Test Conditions for Steady-State Pressure Runs .....	E-3
Appendix F		
F-1	Nominal Test Conditions ( $V = 100$ ft/s) .....	F-3
F-2	Measurement Error Summary .....	F-11

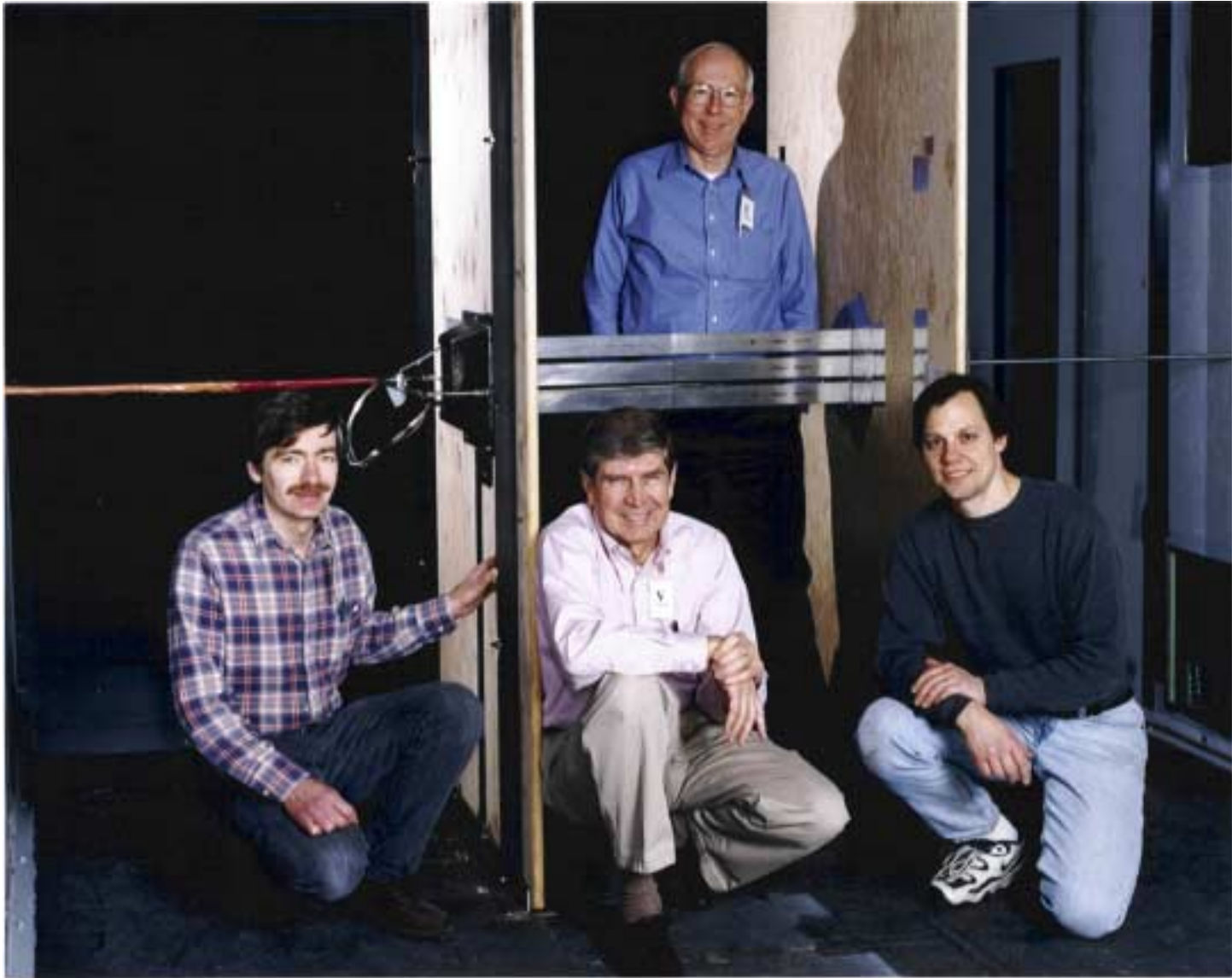
## NOMENCLATURE\*

$A$	Area (in <sup>2</sup> ) (see Equation 15)
$C_{p_i}$	Pressure coefficient at the $i^{\text{th}}$ model orifice
$E$	Youngs modulus (psi) (see Equation 15)
$k_{1,2}$	Calibration factors (see Equation 2)
$L$	Ribbon Length (in) (see Equation 15)
$M$	Mach number
$p_i$	Pressure measured at the $i^{\text{th}}$ model orifice (psi)
$p_r$	Reference pressure measured in the contraction section (psi)
$p_{sp}$	Static pressure measured at the pitot-static probe (psi)
$p_{sr}$	Static pressure measured at a reference ring at the test section entrance (psi)
$p_{tp}$	Total pressure measured at the pitot-static probe (psi)
$q$	Dynamic pressure (psf)
$q_p$	Dynamic pressure at the pitot-static probe (psf)
$R$	Gas constant (1716 ft <sup>2</sup> /s <sup>2</sup> -°R for air)
$Re$	Reynolds number
$T$	Static temperature in the free stream (°R)
$T$	Tension applied to ribbon (lb) (see Equation 15)
$T_o$	Total temperature measured in the free stream (°R)
$u$	Horizontal velocity component (ft/s)
$v$	Vertical velocity component (ft/s)
$V$	Tunnel velocity (ft/s)
$x$	Streamwise coordinate for PIV data (+ downstream, origin at center of front face of center ribbon) (ft)
$y$	Vertical coordinate for PIV data (+ upwards) (ft)
$X$	Streamwise model coordinate (+ upstream, origin at center of front face of center ribbon)
$Y$	Horizontal model coordinate (+ left looking upstream)
$Z$	Vertical model coordinate (+ upwards)
$\delta$	Ribbon elongation due to tensioning (in) (see Equation 15)

---

\* Symbols used in appendices are defined at time of first use.

$\Delta p_i$	$p_i - p_{sr}$
$\Delta p_r$	$p_r - p_{sr}$
$\varepsilon$	Strain (in/in of length) (see Equation 15)
$\gamma$	Ratio of specific heats (1.4 for air)
$\mu$	Viscosity (lb s/ft <sup>2</sup> )
$\rho$	Density (sl/ft <sup>3</sup> )
$\sigma$	Stress (psi) (see Equation 15)
$\omega_z$	Vorticity in the cross tunnel direction (s <sup>-1</sup> ) (defined by Equation 18)



**Frontispiece. The Test Team (Standing – Ed Clark, Kneeling – John Henfling, Don McBride, J. T. Heineck)**

## INTRODUCTION

The absence of a DOE parachute design mission has resulted in the atrophy of Sandia National Laboratories' parachute technology base, a significant reduction in the number of annual Joint Test Assembly (JTA) flight tests, and the loss of experienced staff. As a result, Sandia can no longer rely upon an experience- and test-based approach to stockpile parachute stewardship. In order to fulfill its responsibilities to science-based stockpile stewardship, Sandia has undertaken an ambitious, multiyear effort to move from our present empirically-based parachute system modeling and analysis to a computationally-based, predictive methodology. As part of DOE's Accelerated Strategic Computing Initiative (ASCI), we are developing the VIPAR (Vortex-based Inflation Code for Parachute Simulation) parachute performance prediction code. VIPAR's purpose is to provide a simulation capability for accurate modeling of the inflation process of nuclear weapon parachutes. Such a simulation requires modeling of fluid mechanics in both the incompressible and transonic flight regimes, structural dynamics of light-weight fabric materials undergoing rapid accelerations and shape changes, and tight, numerical coupling between the fluid and structural computations. Our intention is that VIPAR be

- a *predictive tool* to enable parachute engineers to predict the future behavior of stockpile parachute systems,
- a *design tool* to assist future parachute engineers in developing new or modified parachute systems, and
- a *certification tool* to help establish that any new parachute designs meet systems requirements.

The process of demonstrating that VIPAR can accurately simulate the physics of parachute inflation is termed Verification and Validation (V&V). In order to prevent confusion regarding these terms, we provide the following definitions<sup>1</sup>:

- **Verification:** *“The process of determining that a model implementation accurately represents the developers’ conceptual description of the model and the solution to the model.”*

Informally: *The equations are solved correctly.*

The verification process demonstrates that the software implementation is correct and verifies the formal accuracy of the discretization schemes. Verification procedures consist of analytical solutions to the mathematical model equations, established numerical benchmark solutions, and derived analytical solutions based on an equivalent source-term generation procedure.

- **Validation:** *“The process of determining the degree to which a model is an accurate representation of the real world from the perspective of the intended uses of the model.”*

Informally: *The correct equations are solved.*

The validation process consists of comparing the numerical solutions produced by the *verified* analysis code with test data or observations of real physical events and drawing conclusions about the applicability of the models for the intended simulations.

Taken as a set, the verification and validation process ensures that the computer code correctly solves the right set of equations and, therefore, models the physical phenomena of interest with a known accuracy.

Obtaining quality data for code validation can be a difficult and expensive process, especially for problems involving coupled physics, such as fluid/structure interactions of lightweight, flexible structures. The goal of VIPAR is the accurate simulation of high-performance parachutes from inflation to impact. A significant database of parachute flight test data exists. Data from these tests include body trajectory, parachute drag, and inflated shape versus time; however, the quality of these data is not as precise as we would like. Accurate simulations of these tests are required for use of the code but are not sufficient for code validation. Unfortunately, it is practically impossible (both physically and financially) to fully instrument a high-performance parachute and obtain the required quality of data.

The alternative is to design a series of simpler benchmark experiments, each of which provides data to validate a portion or subsystem of the code's physics. Taken as a set they will completely cover the code's required physical range. Upon establishing the validity of the code subsystems in modeling these separate benchmark cases, the validity of the code in modeling the entire system then depends on the correct modeling of the interaction of these subsystems. These data sets can be existing or from experiments explicitly designed for validation of a specific code. In either case the quality of the data must be known. One must have accurate measurements of the geometry of the test, the boundary conditions, and the initial conditions, as well as the test data. The uncertainty in all of these measurements must be quantified. Data sets without an uncertainty analysis are useless for code validation. An additional requirement on the test geometry is that it can be accurately modeled within the code. The simplest geometry that incorporates all of the salient fluid dynamic effects is optimum for validation of the fluids modeling. A complex geometry that is beyond the code's modeling capabilities does not provide a useful validation data set.

This paper will report on an experiment in which the two-dimensional flow through three adjacent "parachute ribbons" at constant freestream velocity was measured. The primary objectives were to obtain measurements of the surface pressure on the ribbons at the same time we were measuring instantaneous velocities in the wake. Surface pressure is of paramount importance since it is the only force acting to inflate the parachute. Since VIPAR is a vortex-based code, wake velocities provide a primary source of information for the validation process. A critical problem could exist with the code if substantially correct pressures were being calculated with erroneous wake velocities. Since no known method existed for the accurate determination of surface pressure on fabric ribbons, thin stainless steel ribbons were used instead. Further, we decided to obtain field measurements of nearly instantaneous velocity over the entire span of the wake behind the set of three ribbons using PIV (Particle Image Velocimetry) techniques, as opposed, for instance, to obtaining continuous, time-varying velocity at a small number of discrete points by other means such as laser Doppler velocimetry or hot-wire techniques.

The test was divided into three phases. In the first phase selected pressure ports were connected to high response transient pressure transducers to provide information on the unsteady nature of the flow. During this phase of the test, the PIV data provided wake velocity fields. In the second phase of the test, all pressure ports were connected to a pressure scanner to provide average, steady-state, pressure distributions on the ribbons. During this phase of the test, it was intended that pressure sensitive paint (PSP) data be taken on the leeward side of the

ribbons. While a significant amount of PSP data was, in fact, obtained, resources did not exist for the complete reduction and analysis of this data due to time overruns in the rest of the test. It is not recommended that additional funding be pursued for this purpose. The third phase of the test was devoted to PIV measurements behind actual 1000 lb fabric ribbons arranged in the same pattern as the stainless steel ribbons. During this phase of the test, no pressure data was taken.

## EXPERIMENT

The test was conducted in March, 1999, in the NASA 7- x 10- Foot, Subsonic Wind Tunnel Number 1, which was the first experimental facility built at the Ames Research Center in Mountain View, CA. The tunnel has been operational since 1941. It is a closed-circuit atmospheric wind tunnel with a 14-to-1 contraction ratio and with a 7-foot high by 10-foot wide by 20-foot long test section. The airflow is produced by a fixed-pitch fan, powered by a variable-speed 1800 hp electric motor. Maximum airspeed is 220 knots. The test section, control room, and adjacent mezzanine work area are all enclosed in a pressurized containment building. It is presently managed by the Army and is used primarily for helicopter rotor studies.

### Pressure Model

The pressure model consisted of three instrumented, simulated parachute ribbons arranged adjacent to each other and perpendicular to the airflow.

Each of the three stainless steel “ribbons” is 2" wide by 3' long by 3/32" thick with the upper and lower edges fully rounded. The choice of these dimensions was based upon two factors — (1) similarity to actual parachute ribbons of interest and (2) fabrication necessities. In the MC3468 (B83 parachute), ribbons 21 through 50 are 1000 lb, 2"-wide ribbons with a selvage that is approximately 3/32" thick. Fifteen to seventeen 0.045" x 0.045" grooves were milled into the three 3/32"-thick stainless steel plates to accommodate the pressure transmission tubes. This left enough cross section that the steel plate was still sufficiently strong to withstand the wind loading. 0.040"-O.D. x 0.030"-I.D., thin-walled, stainless steel tubes were epoxied into these grooves and provided an adequate diameter for the transmission of pressure to the remotely located transducers. Excess epoxy was sanded off to provide an aerodynamically smooth surface. One end of each tube extended through the end of the ribbon for connection to the transducers. The stainless steel tubing was sealed at the other end where a 0.020"-diameter pressure orifice connected the interior of the tubing to either the ribbon front or rear surface (see Figure 1).

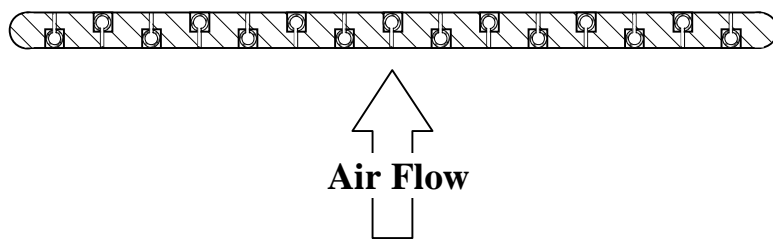


Figure 1. Cross section of stainless steel ribbon at centerline.

These orifices were machined using the electrical discharge machining (EDM) technique, thus ensuring sharp orifices with no internal burrs.

Figure 2 and Table 1 show the exact locations of these ports relative to a right-hand coordinate system that has its origin at the upstream center of the center ribbon with the *X*-axis extending upstream and the *Z*-axis extending vertically upward. It should be noted that the pressure port identification numbers stayed with the ribbons whenever the position of the ribbons was changed.

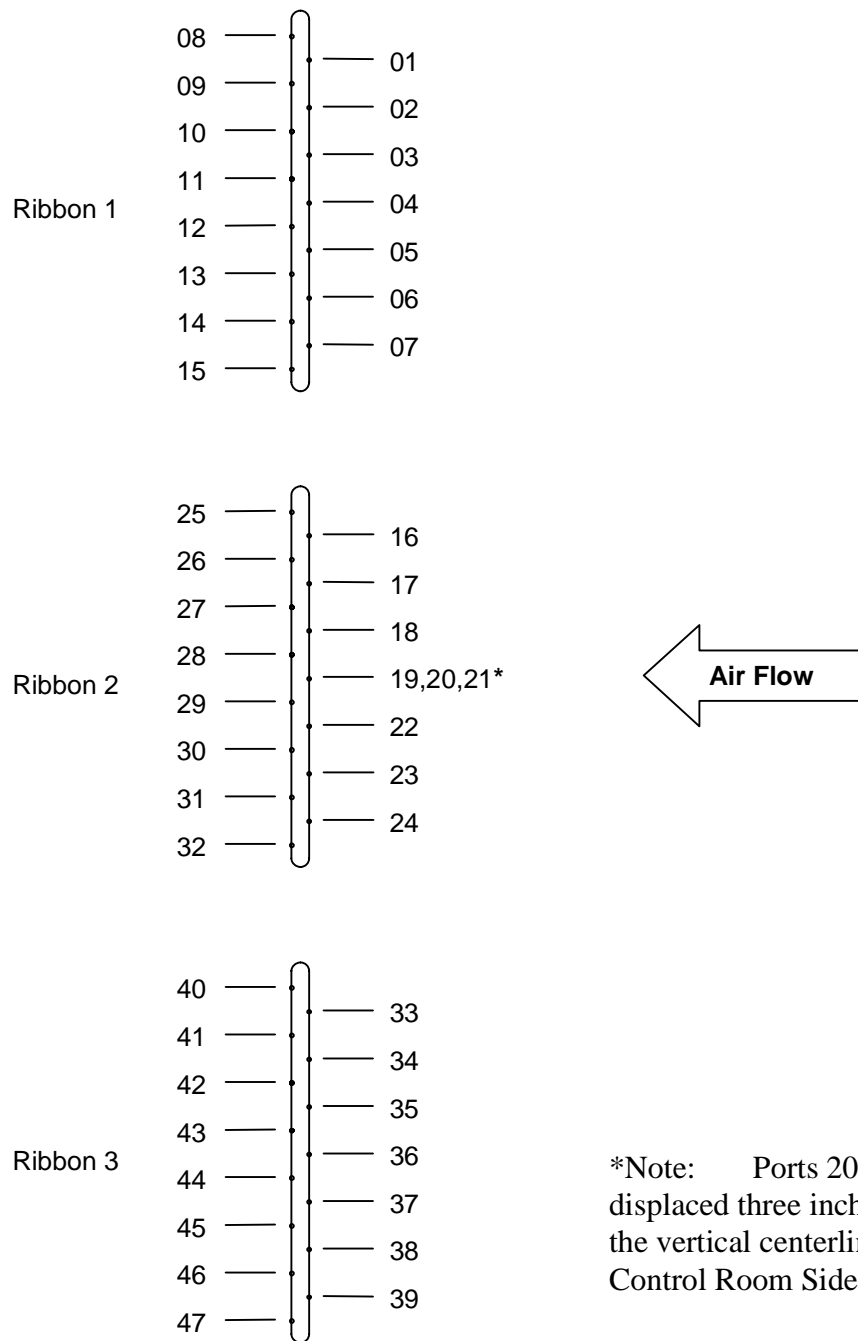


Figure 2. Pressure port identification.

Table 1. Pressure Port Locations

Pressure Port Identification Number	Ribbon Number	Windward Side	Leeward Side	Z Location (inches from centerline)	Y Location (inches from centerline)
1	1	✓		0.75	0
2	1	✓		0.5	0
3	1	✓		0.25	0
4	1	✓		0	0
5	1	✓		-0.25	0
6	1	✓		-0.5	0
7	1	✓		-0.75	0
8	1		✓	0.875	0
9	1		✓	0.625	0
10	1		✓	0.375	0
11	1		✓	0.125	0
12	1		✓	-0.125	0
13	1		✓	-0.375	0
14	1		✓	-0.625	0
15	1		✓	-0.875	0
16	2	✓		0.75	0
17	2	✓		0.5	0
18	2	✓		0.25	0
19	2	✓		0	0
20	2	✓		0	-3.0
21	2	✓		0	3.0
22	2	✓		-0.25	0
23	2	✓		-0.5	0
24	2	✓		-0.75	0
25	2		✓	0.875	0
26	2		✓	0.625	0
27	2		✓	0.375	0
28	2		✓	0.125	0
29	2		✓	-0.125	0
30	2		✓	-0.375	0
31	2		✓	-0.625	0
32	2		✓	-0.875	0
33	3	✓		0.75	0
34	3	✓		0.5	0
35	3	✓		0.25	0
36	3	✓		0	0
37	3	✓		-0.25	0
38	3	✓		-0.5	0
39	3	✓		-0.75	0
40	3		✓	0.875	0
41	3		✓	0.625	0
42	3		✓	0.375	0
43	3		✓	0.125	0
44	3		✓	-0.125	0
45	3		✓	-0.375	0
46	3		✓	-0.625	0
47	3		✓	-0.875	0

## **Tunnel Installation**

Floor-to-ceiling splitter plates 4' long by 1" thick, and rounded on the leading edge, were spaced 3' apart in the center of the tunnel. The ribbons spanned this "two-dimensional" section. Figure 3 is a pre-test sketch of the tunnel installation while Figure 4 is a photograph of the actual installation inside the wind tunnel. The ribbons were spaced 1/2" apart and were tightly mounted into rigid frames which passed (with 0.005" total clearance) through the splitter plates. Thus the splitter plates provided surfaces to react any loads in the downstream direction while not reacting any loads in the cross-stream (tension) direction. These frames were, in turn, connected to 1/2" threaded rods which passed through small holes in the wind tunnel walls to structural beams external to the wind tunnel envelope. It should be noted that since the control room and adjacent mezzanine work area were sealed from atmospheric pressure, the pressure in the control room equalized with the static pressure in the test section. Thus there was no significant air flow through the tension rod clearance holes. The tension rods were tensioned to approximately 700 lb total tension by means of a spring-loaded compression fixture (see Figure 5) on the outside of the control-room side beam. The tension load was measured with a load washer. Each stainless steel pressure tube extended through the control-room side splitter plate where an 11.5" length of 0.030"-I.D. Tygon<sup>®</sup> tubing connected it to one of the pressure transducers (see Figure 6). To shield the tubing and transducers from wind and thermal effects, a plastic windshield covered the entire transducer area (see Figure 7).

Windows in the control-room side splitter plate and wind tunnel wall allowed visual access to the 1'-square area immediately aft of the ribbons for PIV measurements while a window in the wind tunnel ceiling allowed access for the illuminating laser sheet. The particles were injected into the tunnel airflow through an aerodynamic fairing located on the wind tunnel floor approximately 6 ft downstream of the 2-D test section.

Lighting for the PSP measurements, taken during the steady-state portion of the test, was provided with floodlights mounted in a box approximately 1 ft tall x 1 ft deep x 2 ft wide. This box was located on the wind tunnel floor at least 9 ft downstream of the test section. Test runs indicated no effect from its presence on either the airflow in the 2-D test section or on the pressures measured on the ribbons.

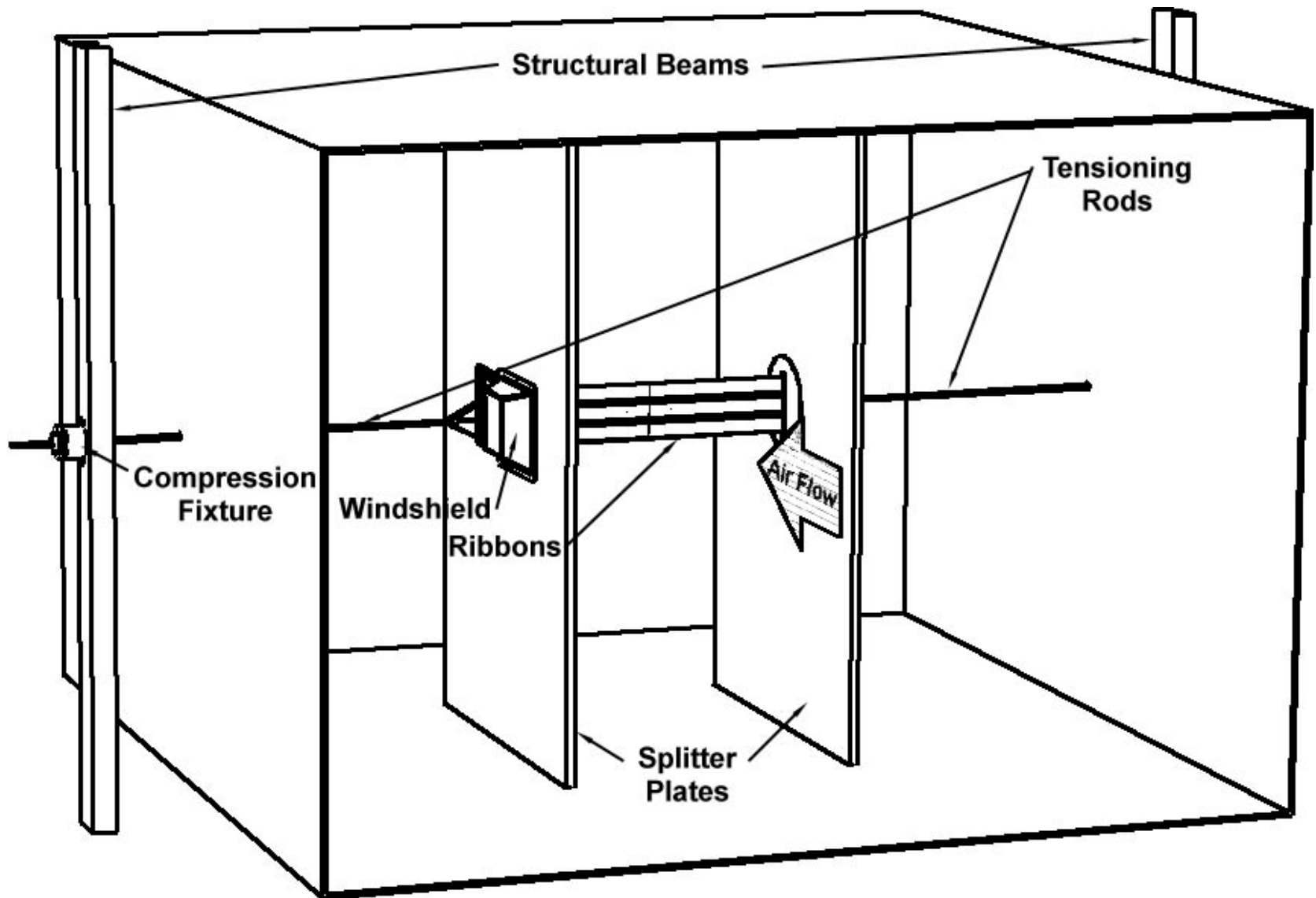


Figure 3. Pre-test sketch of tunnel installation.



Figure 4. Photograph of tunnel installation.

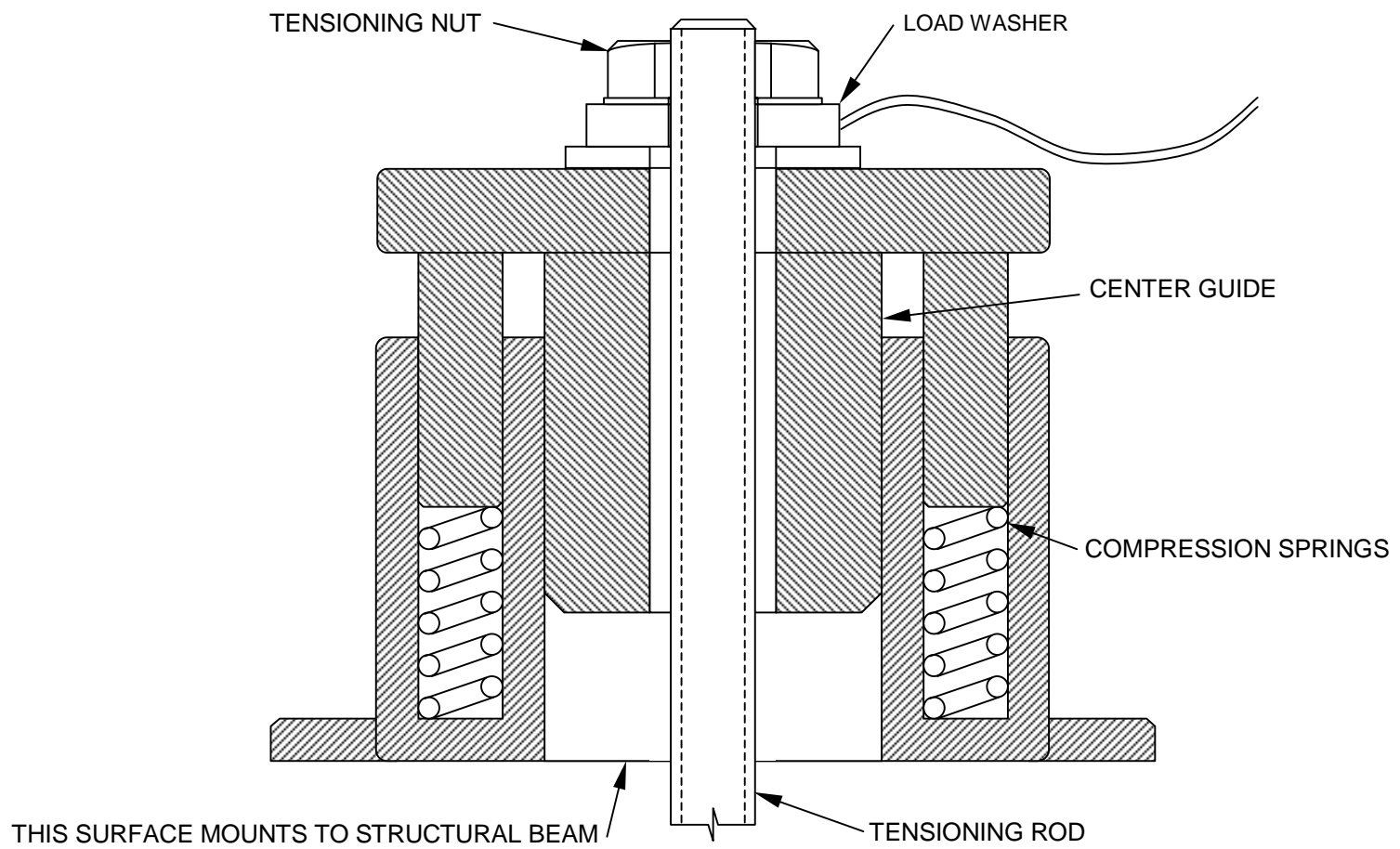


Figure 5. Spring-loaded compression fixture for tensioning ribbons

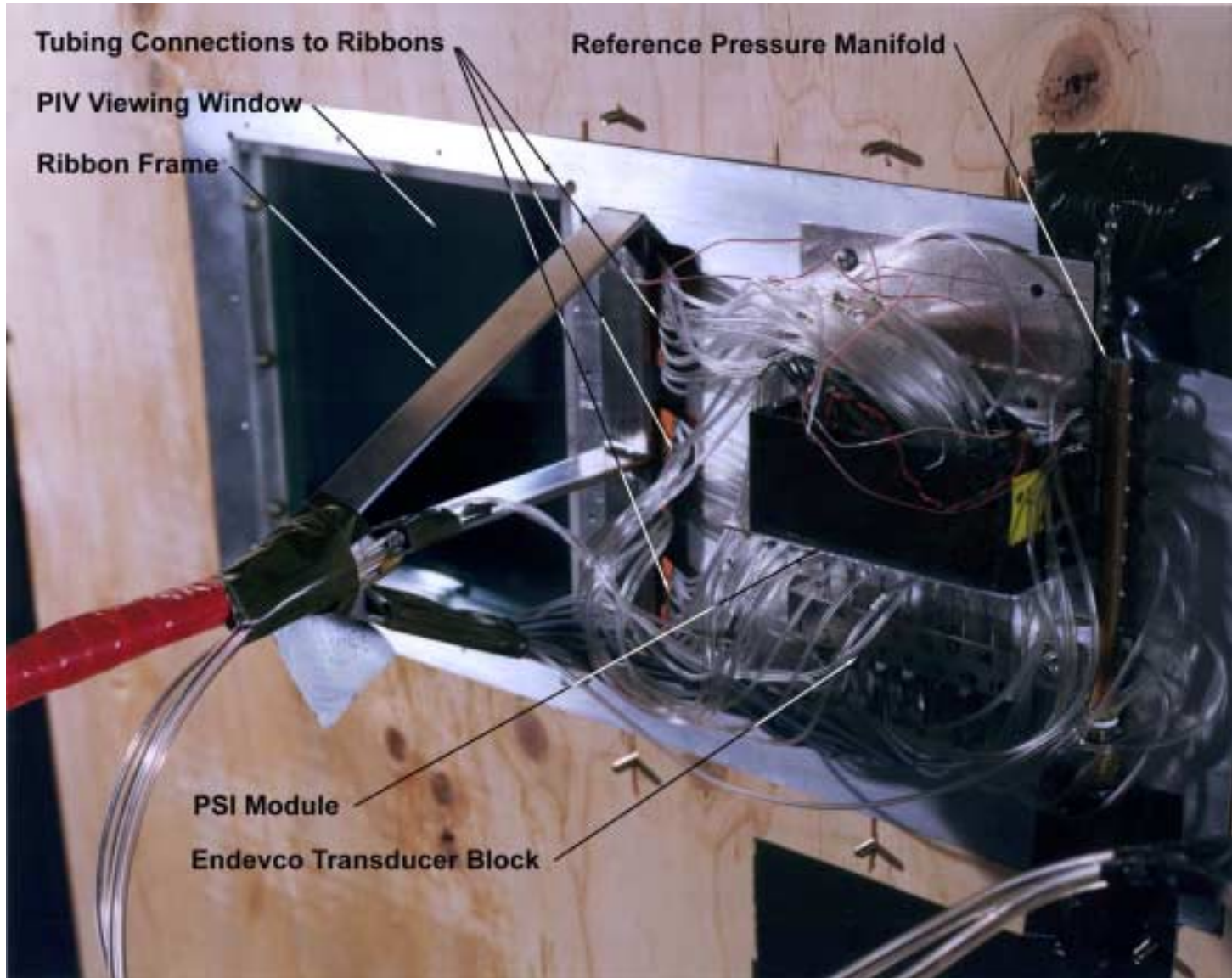


Figure 6. Photograph of pressure transducer connections on outside surface of splitter plate



Figure 7. Photograph of windshield covering pressure transducers and connections.

## INSTRUMENTATION, DATA ACQUISITION, AND DATA REDUCTION

### Unsteady Pressure Measurements

The 15 differential pressures of interest during the unsteady data (time series) phase of the test were measured with Endevco<sup>®\*</sup> piezoresistive pressure transducers, Model 8510B-1. These transducers have a flush diaphragm with a resonant frequency of 55,000 Hz, and are rated for 0 to 1 psig. Although not a true differential transducer, these transducers are bi-directional and have a reference vent tube. For this test, the vent tubes were connected to a manifold which was connected to the tunnel static ring manifold, thereby providing a reference pressure equal to  $p_{sr}$ . One transducer was connected to the tunnel reference pressure manifold, giving a “tunnel conditions” differential pressure,  $p_r - p_{sr}$ . These reference pressures are discussed in detail in Appendix A. The remaining 14 transducers were attached with Tygon<sup>®</sup> tubing to the model pressure tubes as described earlier. The transducers have a threaded body and o-ring seal. All 15 transducers were threaded into a stainless steel block which was designed to provide a minimal cavity above the diaphragm and a 0.040 inch O.D. stainless steel tubing interface to the Tygon tubing. The transducer block provided thermal mass and was shielded with foam and the plastic cover to reduce the effects of temperature changes during lengthy runs. Signal conditioning for the transducers was provided by an Endevco Model 136 Three-Channel Differential Voltage Amplifier which incorporated a four-pole, Butterworth anti-aliasing filter. The filter had a 3-db (voltage gain = 0.707) cutoff frequency of 600 Hz. The filter characteristics were measured and found to be satisfactory. A National Instruments<sup>®</sup> AT-MIO-16X A/D converter (16-bits, 100 kHz scan rate) was used to convert the analog signal to digital form. Transducers which measured the model pressures were calibrated over a pressure range of  $-0.2$  to  $+0.2$  psid, using a Paroscientific<sup>®</sup> Digiquartz Model 760 portable standard with a full-scale range of 15 psia. Numerous calibrations were made to establish the accuracy of the transducers. Scale factors from the last four pretest calibrations and the two post-test calibrations were averaged and used in the data reduction. A single calibration, over a pressure range of 0 to 0.2 psid, was used to estimate the scale factor for the differential reference pressure,  $p_r - p_{sr}$ .

A Paroscientific Digiquartz Model 760 (15 psia) was also used to measure the absolute pressure in the static ring manifold,  $p_{sr}$ .

Tunnel total temperature was measured with an electronic sensor (Radio Shack<sup>®</sup> cat. no. 63-1009A) located on the leading edge of the tensioning rod, approximately half way between the control-room-side splitter plate and the tunnel wall. The temperature was recorded at the beginning of each run and manually input to the data reduction code.

Data were acquired with a sampling rate of 800 samples/second and the number of samples for each transducer was 8192 giving a total acquisition time of 10.24 seconds. The acquisition parameters were selected to satisfy requirements for confidence interval on the mean  $C_p$  and frequency response. These requirements are discussed in Appendices B and C, respectively. The inter-channel delay for the A/D was 10  $\mu$ s (100 kHz scan rate), giving a slew time from

---

\* The use of manufacturer's names is only for the purpose of fully documenting the test procedure. No evaluation or endorsement of the product is intended.

first to last transducer of 0.15 ms. The inter-channel delay was dictated by A/D board capability.

Data reduction was accomplished with a Labview<sup>®</sup> code. A switch in the code allowed the user to reduce the data in either pressure (used primarily for diagnostic purposes) or pressure coefficient form. A detailed description of the pressure coefficient,  $C_p$ , calculations is given in Appendix A and will only be summarized here. We define  $C_p$  as,

$$C_{p_i} = \frac{P_i - P_{sp}}{q_p}, \quad (1)$$

where  $p_i$  is the  $i^{\text{th}}$  measured model pressure,  $p_{sp}$  is the tunnel static pressure measured with a pitot-static probe 18 inches upstream of the model center, and  $q_p$  is the tunnel dynamic pressure at the same location. Because  $p_{sp}$  and  $q_p$  could not be measured at the same time as model measurements, these pressures were calculated from the tunnel reference differential pressure,  $p_r - p_{sr}$ . Since the transducers actually measured differential pressures,  $p_i - p_{sr}$ , the data reduction equation for  $C_p$  was,

$$C_{p_i} = \frac{(p_i - p_{sr}) - k_1(p_r - p_{sr})_{avg}}{k_2(p_r - p_{sr})_{avg}}, \quad (2)$$

where  $k_1$  and  $k_2$  are calibration factors described in Appendix A. As noted in Equation (2), the value of the reference differential pressure,  $p_r - p_{sr}$ , used in calculating  $C_p$  was an average of the 8192 samples from the test run. The reason for not using reference pressures measured at the same time as model pressures was a concern for transport time errors. The static ring orifices were almost ten feet upstream of the model and the reference orifices were even further upstream. At a tunnel velocity of 100 feet/second, it would take a flow nonuniformity (periodic or random) at the static ring almost 0.1 second to reach the model. At a sampling rate of 800 samples/second, the static ring measurement would lag the model measurement by 80 samples. Therefore, it was felt that an average value should be used for the reference differential pressure. This was almost certainly an overly conservative decision since fluctuations in both  $p_r$  and  $p_{sr}$  are heavily damped in the large manifolds associated with these measurements. Comparison of the standard deviation for reference pressure with those for model pressures shows that fluctuations in reference pressure are much smaller than those in the model pressures (standard deviation of the reference pressure is two to three percent of that for the windward model pressures). For each transducer, in addition to instantaneous values of  $C_p$ , the mean and standard deviation of  $C_p$  were calculated from the 8192 samples.

The pressure measurement system — orifice, steel tubing, Tygon tubing, and transducer block cavity — acts as a pneumatic filter, reducing fluctuations in the pressure measurements. For validation purposes, it is necessary to estimate the unfiltered pressures from the measurements. The procedure used to reconstruct the true pressures is described in Appendix D. Pressure coefficients calculated from the reconstructed pressures were tabulated for each sample.

Power spectral density (PSD) function calculations were essential to identify significant frequency components in the data. PSD calculations are described in Appendix C and were tabulated for both the measured and reconstructed pressures. Mean and standard deviation values were calculated for the pressure coefficients calculated from the reconstructed pressures. The mean values of the measurements and the reconstructed estimates were the same. This is

because the reconstruction process does not change the DC ( $f = 0$ ) level since the transfer function gain is equal to 1.0 at  $f = 0$ . However, the standard deviation of the reconstructed data was significantly larger than that for the measurements. This would be expected since the pneumatic filtering reduces the variance in the data.

Calculation of various test conditions used the following equations with average values. The static pressure ahead of the model,  $p_{sp}$ , was calculated from measured absolute and differential pressures,  $p_{sr}$  and  $(p_r - p_{sr})$  as follows:

$$p_{sp} = p_{sr} + (p_{sp} - p_{sr}) = p_{sr} + k_1 (p_r - p_{sr})_{avg}. \quad (3)$$

The dynamic pressure,  $q_p$ , ahead of the model is given by

$$q_p = k_2 (p_r - p_{sr})_{avg}. \quad (4)$$

A thermally perfect gas is one which obeys the thermal equation of state,

$$p = \rho R T, \quad (5)$$

where  $\rho$  is the density and  $R$  is the gas constant for air, 1716 ft<sup>2</sup>/s<sup>2</sup> °R. For a thermally perfect gas, the dynamic pressure,  $q$ , is given by

$$q = \frac{\gamma}{2} \rho M^2, \quad (6)$$

where  $\gamma$  is the ratio of specific heats, 1.4. Solving for Mach number,  $M$ ,

$$M = \sqrt{\frac{q_p}{0.7 p_{sp}}}. \quad (7)$$

The static temperature,  $T$ , is related to the measured total temperature,  $T_o$ , by

$$T = \frac{T_o}{\left(1 + \frac{\gamma - 1}{2} M^2\right)} = \frac{T_o}{(1 + 0.2 M^2)}. \quad (8)$$

From the definition of dynamic pressure,

$$q = \frac{\rho V^2}{2}, \quad (9)$$

then,

$$V = \sqrt{\frac{2RqT}{p}} \quad (10)$$

and

$$V_p = \sqrt{\frac{2Rq_p T}{p_{sp}}}. \quad (11)$$

The Reynolds number,  $Re$ , is given by,

$$Re = \frac{\rho V h}{\mu}, \quad (12)$$

where  $h = 2$  inches, the density,  $\rho$ , is given by

$$\rho = \frac{P_{sp}}{RT} \quad (13)$$

and viscosity,  $\mu$ , is given by Sutherland's equation,

$$\mu = \frac{2.27 \times 10^{-8} T^{1.5}}{T + 198.72}. \quad (14)$$

A summary of the test conditions is presented in Appendix E.

### **Steady-State Pressure Measurements**

For steady-state measurements, a Pressure Systems, Inc.® (PSI), 48-channel Electronically Scanned Pressure module (ESP-48, 10" water column or 0.36 psi full-scale) with associated Pressure Calibration Unit (PCU, 1.0 psi Digiquartz standard — calibration range was -0.25 to +0.25 psi in 5 steps) and signal conditioning hardware was used. The module was placed in a heated box, protected from the flow, to provide a stable operating temperature. Forty seven of the channels were dedicated to model measurements and one was used for the differential reference pressure,  $p_r - p_{sr}$ . Acquisition nomenclature for the PSI is somewhat critical to understanding how the data are acquired. First, there is a "frame" of data, which contains one sample each of the pressure measured at each of the 48 ports. Several frames are averaged to provide a "set." Within a set, data were scanned at 20kHz, that is, a sample interval of 50 $\mu$ s per port. There are two start up intervals (during which no data is acquired), 48 acquisition intervals (13  $\mu$ s for acquisition and 37  $\mu$ s for analog settling time), followed by two end intervals in each frame. Thus, a frame requires  $(2+48+2)*50 \mu\text{s} = 0.0026$  second to complete. The following frame starts immediately (zero delay), so the sampling frequency is  $1/0.0026 = 385$  Hz. This is approximately half the sampling rate for the unsteady data. For this test, 127 frames were included in a set. Individual pressures from each frame are not available, only the mean pressures for the entire set. The acquisition time for a set is then  $127*0.0026 = 0.33$  second, followed by a 0.67-second delay. Therefore, the time between sets was exactly 1.00 second. Finally, 200 sets were acquired for a total acquisition time of 200 seconds. Only mean values for each set are available with the PSI system, so time-series analysis was not possible with this data. Mean and standard deviation of the mean pressures were computed for the 200 sets.

Test conditions were calculated from the differential reference pressure,  $p_r - p_{sr}$ , using the equations in the previous section.

## EXPERIMENTAL UNCERTAINTY

### Measurement Uncertainty

The measurement uncertainty analysis is described in detail in Appendix F. The traditional procedure endorsed by such organizations as the American Society of Mechanical Engineers and the American Institute of Aeronautics and Astronautics was used. With this approach, measurement source errors are identified and quantified. They are then categorized as bias or precision errors. The errors are then combined by a root-sum-square calculation to give an estimate of the total error in a measurement. Finally, if calculated results, such as pressure coefficient  $C_p$ , are involved, a Taylor series error propagation method is used to estimate the uncertainty in the result due to the measurement errors.

A summary of the measurement uncertainties for  $V = 100$  ft/s is presented in Table 2 below. Because the uncertainty in  $C_p$  was nearly the same for windward and leeward ports, an average value is given in the table. Also, since many of our presented results are averages of multiple measurement samples, the uncertainty for both unaveraged and averaged values is listed. Finally, because the pressure reconstruction process is so vital to our unsteady pressure results, the effects of reconstruction errors are included in the uncertainties for  $\Delta p_i$  and  $C_p$ .

Table 2. Uncertainty Summary ( $V = 100$  ft/s)

	Endevco Data	PSI Data
$\Delta p_i$	0.00142 psid	0.00073 psid
$\Delta p_i^*$	0.00144 psid	NA
$\Delta p_r$ (avg.)	0.00108 psid	0.00010 psid
$C_p$	0.0205	0.00374
$C_p^*$	0.0262	NA
$C_p$ (avg.)	0.0184	0.00161
$C_p$ (avg.)*	0.0186	NA
$q$ (avg.)	0.00087 psi	0.00008 psi
$p_{sp}$ (avg.)	0.00152 psia	0.00150 psia
$V$ (avg.)	0.555 ft/s	0.179 ft/s

$\Delta p_i^*$ ,  $C_p^*$ ,  $C_p$  (avg.)\* = measurement error plus reconstruction error

For  $V = 80$  ft/s: the uncertainty in  $\Delta p_i$  is unchanged; the uncertainty in  $C_p$  values is increased by a factor of 1.54; the uncertainty in  $V$  is increased by 1.18 for Endevco measurements and decreased by 0.85 for PSI measurements. For  $q$  and  $p_{sp}$ , the change in uncertainty is insignificant.

## Uncertainty from Flow Dynamics

In addition to measurement uncertainties, there was uncertainty in  $C_p$  (avg) which resulted from data variance created by the flow dynamics (see Appendix B). These uncertainties are summarized in the table below. For this uncertainty source, the windward and leeward values are significantly different as a result of the much greater variance in the leeward data. Also, the uncertainty is greater for reconstructed data because the variance in this data is greater than that in the basic data.

Table 3. Uncertainty From Flow Dynamics

	Endevco Data	PSI Data
Basic data:		
$C_p$ (avg.) – windward	0.00210	0.00078
$C_p$ (avg.) – leeward	0.00954	0.00358
Reconstructed data:		
$C_p$ (avg.) – windward	0.00273	NA
$C_p$ (avg.) – leeward	0.01113	NA

## Uncertainties in Model Alignment

The primary uncertainty in model alignment resulted from the fact that the model designer (the senior author of this report) did not realize the necessity for allowing for independent tensioning of the ribbons. Only upon analysis of the data did this oversight become evident. As shown in Figure 8, switching ribbons 1 and 2 introduced relatively significant differences in the center ribbon pressure windward-side distribution (order of 8% pressure differences at the center ribbon edges — or  $\Delta C_p = 0.08$ ).

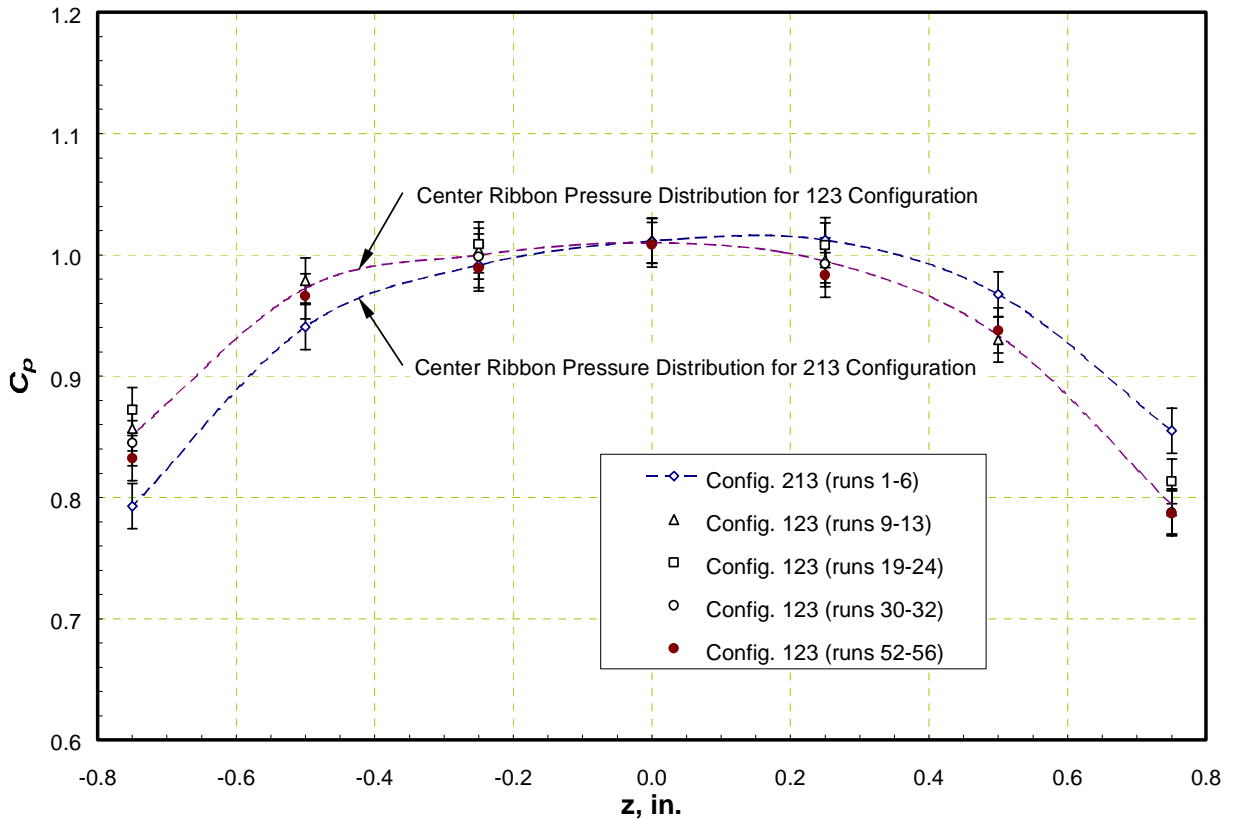


Figure 8. Center ribbon windward pressure distribution in 2-1-3 vs. 1-2-3 configurations

While these differences could have been due to other problems, it is known that the tension was not necessarily equalized across the ribbons. It should be noted that the reason tension would affect model alignment derives from the difference in ribbon deflection under wind load. During tunnel installation, ribbon alignment with vertical was checked with a bubble level and several measurements of ribbon position were made with regard to the PIV setup. No misalignment was noted. Therefore, we feel very confident that the ribbons, as installed and with no wind loading, were properly aligned. However, under wind load the ribbons can be expected to deflect considerably with the deflection being a strong function of the tension in the ribbon (see Figure 9).

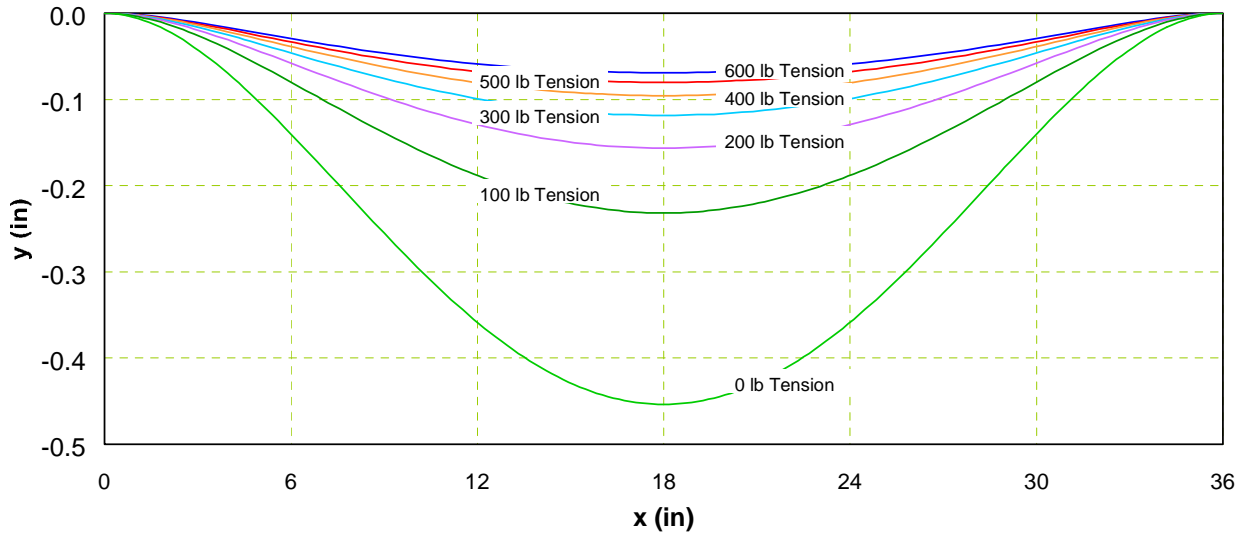


Figure 9. Tension effects on ribbon deflection under 100 ft/s wind load.

The test was run with a total tension load on the three ribbons of 690 lb. If all ribbons were tensioned equally, this would result in a ribbon elongation of only 0.0018 in (well within the manufacturing tolerances on ribbon length.) i.e.,

$$\delta = \epsilon L = \frac{\sigma L}{E} = \frac{TL}{AE} = \frac{230lb}{0.150in^2} \frac{36in}{30(10)^6 psi} = 0.0018in . \quad (15)$$

To get a better grasp on the amount of misalignment that might have been experienced in the tunnel, we reassembled the hardware in the lab and loaded it in a manner similar to what might have been expected in the tunnel. We mounted the ribbons and frames in an Instron<sup>®</sup> Tensile Testing machine and applied 690 lb total tension. We then measured the horizontal deflection resulting from a total horizontal load of 25 lb applied equally to the ribbons which simulated the wind loading at 100 ft/s. These measurements were made with the ribbons both in the 2-1-3 configuration (see Figure 10) which was in place for runs 1 through 6, and for the 1-2-3 configuration (see Figure 11) which was in place for the remainder of the runs. It is evident from Figure 10 that the overall flow field would be strongly influenced by this type of misalignment and could account for the variant surface pressure distribution previously seen in Figure 8. While we made no exhaustive analysis of the accuracy of the measurements, a reasonable estimate of confidence would be that the results are good to  $\pm 0.010$  in.

It is recommended that any computer simulation of the pressure data should use a model based on Figure 11. However, perturbations of this geometry by displacing each ribbon as much as 0.010 in. should be made to assure that the results are not strongly influenced by possible errors in the misalignment.

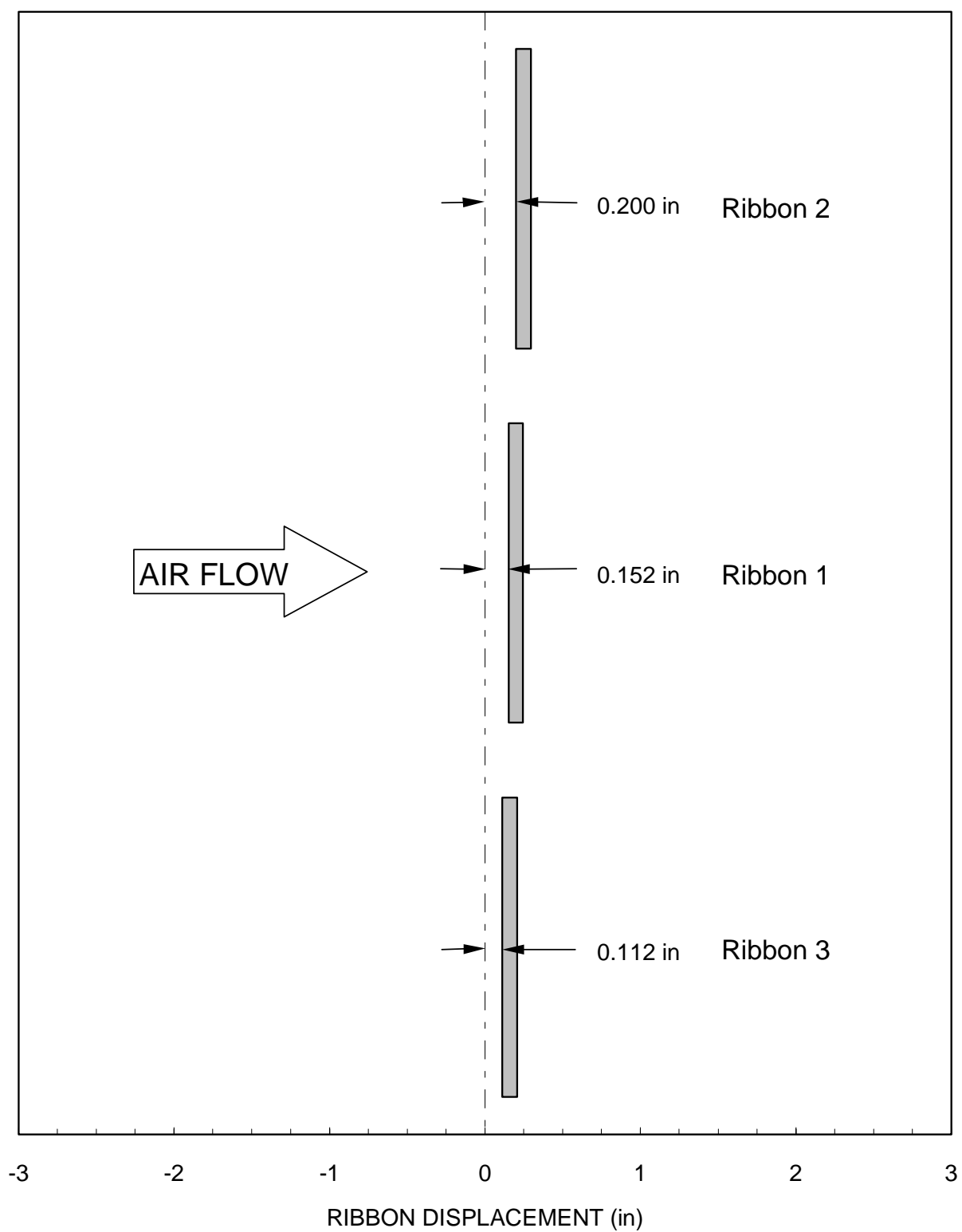


Figure 10. Ribbon misalignment with ribbons in 2-1-3 configuration.

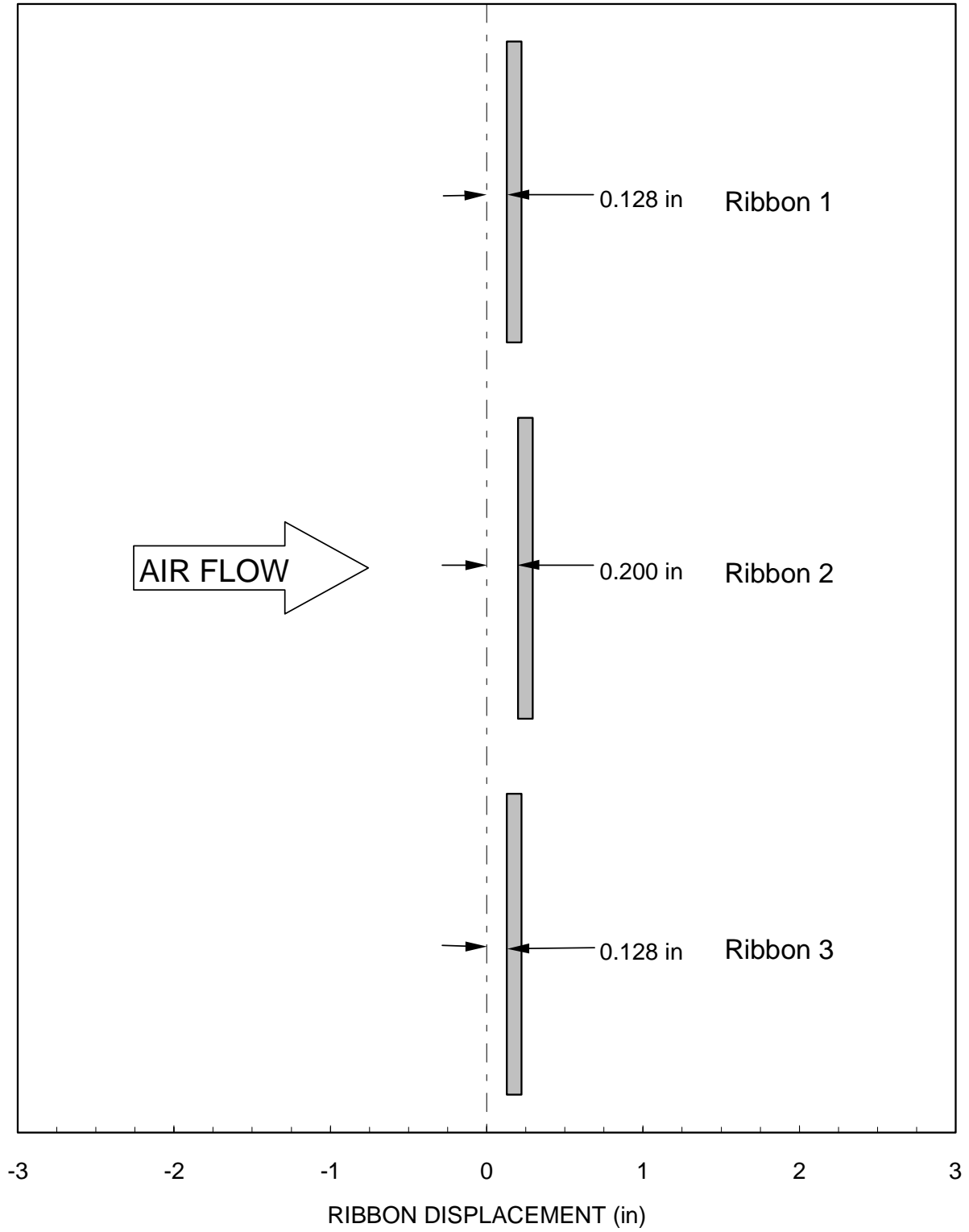


Figure 11. Ribbon misalignment with ribbons in 1-2-3 configuration.

## RESULTS

### Unsteady Pressure Measurements

Only 15 transducers and associated instrumentation were available, so during this phase of the test only a subset of the total number of ports was connected at any one time. To assure ourselves that the pressures measured were not dependent on the specific ribbons, the initial ribbon configuration was with ribbons 1 and 2 switched from the intended nominal configuration shown in Figure 2. Thus, “production” runs 1 through 6 were made with the ribbons arranged in a 2-1-3 pattern (i.e., ribbon 1 was located in the center with ribbon 2 above and ribbon 3 below it). The unsteady pressures at ports 1 through 15 (except for port 11) were recorded. The fifteenth transducer was used to measure  $p_r - p_{sr}$  for calculation of  $C_p$ .

Table 4 presents a run log for the pressure measurement phase of the test showing which pressure ports were connected to which transducers for each run. It also indicates (\*) whether synchronized PIV data was taken. Reduced data from these runs is archived in a CD labeled “Unsteady Pressure Data” in a tab-delineated format that can be opened directly into MS Excel<sup>®</sup> for analysis or graphing. (This CD has been delivered to Steven Kempka, 9111.) The file header gives the run information (Run Number,  $q_{avg}$ ,  $T_o$ ,  $p_{sp}$ ,  $M$ , and  $V$ ). The first column gives the time associated with the  $C_p$  data for each channel, while the second column gives the frequency associated with the power spectral density data for each channel. Following these two columns are 14 groups (labeled “Cp 0” through “Cp13”) of four columns each. These four columns consist of: (1) the  $C_p$  as measured (labeled “Presp.”), (2) the  $C_p$  as reconstructed (labeled “Precon.”), and (3) and (4) the power spectral density of those two functions, respectively (labeled “Sxx” and “Sxx of Precon.”). The 15<sup>th</sup> group (labeled “qts”) of four columns contains the measurement of  $p_r - p_{sr}$ . However, the only meaningful column in this group is the first and it contains the actual measurement of  $p_r - p_{sr}$  in psi. The reconstruction is meaningless as the measurement was not done through the same tubing system as the other 14 channels (and, at any rate, the mean value was the only significant value). It was simply more convenient to carry the columns along in the data reduction program than to treat them differently. The last column contains the PIV sync signal which went high at the moment the PIV data was taken. Following the 8192 rows of data are computed means and standard deviations for the  $C_p$  and  $p_r - p_{sr}$  measurements and the integrals of the PSD data. It should be noted that the “frequency column” and the “PSD columns”, while only 512 rows long and located at the top of the data sheets, do not simply refer to the PSD during this time span. Rather, they represent an average of the PSD over the entire run as explained in Appendix C.

A representative time series plot of the front face reconstructed pressures is shown in Figure 12. It is apparent that a strong oscillation of approximately 100 Hz is mirrored in all of the pressures. Figure 13, the power spectral density for pressure port 22 (near the center of the ribbon and the highest pressure in Figure 12), shows this oscillation quite clearly and identifies the frequency as 94.5 Hz. Prior to tunnel entry we had anticipated a vortex shedding frequency of around 70 Hz. At first glance, we felt we had found the vortex shedding frequency. However, in subsequent runs at tunnel velocities of only 80 ft/s, this same frequency continued to dominate. Since vortex shedding frequency is nearly linear with velocity, it therefore appeared that this frequency spike was from some other phenomenon. A calculation of organ pipe frequency for a total tubing length of 32 in. turned out to be very close (105 Hz). However, we had not seen any organ pipe resonance in the transfer function experiment.

Table 4. Run Schedule for Stainless Steel Ribbons (\* indicates PIV data taken)

Run #	Config #	Nominal V (fps)	Nominal Q (psf)	Trans #1 Chan#0	Trans #2 Chan#1	Trans #3 Chan#2	Trans #4 Chan#3	Trans #5 Chan#4	Trans #6 Chan#5	Trans #7 Chan#6	Trans #8 Chan#7	Trans #9 Chan#8	Trans #10 Chan#9	Trans #11 Chan#10	Trans #12 Chan#11	Trans #13 Chan#12	Trans #14 Chan#13	Chan#14	PSP Box	Remarks	
1	213	100	11.890	01	02	03	04	05	06	07	08	09	10	12	13	14	15	P <sub>R</sub> -P <sub>SR</sub>			
2	213	100	11.890	01	02	03	04	05	06	07	08	09	10	12	13	14	15	P <sub>R</sub> -P <sub>SR</sub>			
3	213	100	11.890	01	02	03	04	05	06	07	08	09	10	12	13	14	15	P <sub>R</sub> -P <sub>SR</sub>			
4	213	100	11.890	01	02	03	04	05	06	07	08	09	10	12	13	14	15	P <sub>R</sub> -P <sub>SR</sub>			
5	213	100	11.890	01	02	03	04	05	06	07	08	09	10	12	13	14	15	P <sub>R</sub> -P <sub>SR</sub>			
6	213	100	11.890	01	02	03	04	05	06	07	08	09	10	12	13	14	15	P <sub>R</sub> -P <sub>SR</sub>			
7	123	80	7.610	All Pressure Ports Taped																	
8	123	90	9.631	All Pressure Ports Taped																	
9	123	100	11.890	16	17	18	19	22	23	24	25	26	27	29	30	31	32	P <sub>R</sub> -P <sub>SR</sub>		Repeat of Run # 1 with ribbons switched	
10	123	100	11.890	16	17	18	19	22	23	24	25	26	27	29	30	31	32	P <sub>R</sub> -P <sub>SR</sub>			
11	123	100	11.890	16	17	18	19	22	23	24	25	26	27	29	30	31	32	P <sub>R</sub> -P <sub>SR</sub>			
12	123	100	11.890	16	17	18	19	22	23	24	25	26	27	29	30	31	32	P <sub>R</sub> -P <sub>SR</sub>			
13	123	100	11.890	16	17	18	19	22	23	24	25	26	27	29	30	31	32	P <sub>R</sub> -P <sub>SR</sub>			
14	123	80	7.610	16	17	18	19	22	23	24	25	26	27	29	30	31	32	P <sub>R</sub> -P <sub>SR</sub>			
15	123	80	7.610	16	17	18	19	22	23	24	25	26	27	29	30	31	32	P <sub>R</sub> -P <sub>SR</sub>			
16	123	80	7.610	16	17	18	19	22	23	24	25	26	27	29	30	31	32	P <sub>R</sub> -P <sub>SR</sub>			
17	123	80	7.610	16	17	18	19	22	23	24	25	26	27	29	30	31	32	P <sub>R</sub> -P <sub>SR</sub>			
18	123	80	7.610	16	17	18	19	22	23	24	25	26	27	29	30	31	32	P <sub>R</sub> -P <sub>SR</sub>			
19	123*	100	11.890	01	07	16	18	22	24	33	39	08	15	25	32	40	47	P <sub>R</sub> -P <sub>SR</sub>			
20	123*	100	11.890	01	07	16	18	22	24	33	39	08	15	25	32	40	47	P <sub>R</sub> -P <sub>SR</sub>			
21	123*	100	11.890	01	07	16	18	22	24	33	39	08	15	25	32	40	47	P <sub>R</sub> -P <sub>SR</sub>			
22	123*	100	11.890	01	07	16	18	22	24	33	39	08	15	25	32	40	47	P <sub>R</sub> -P <sub>SR</sub>			
23	123	100	11.890	01	07	16	18	22	24	33	39	08	15	25	32	40	47	P <sub>R</sub> -P <sub>SR</sub>			
24	123*	100	11.890	01	07	16	18	22	24	33	39	08	15	25	32	40	47	P <sub>R</sub> -P <sub>SR</sub>			
25	123*	80	7.610	01	07	16	18	22	24	33	39	08	15	25	32	40	47	P <sub>R</sub> -P <sub>SR</sub>			
26	123*	80	7.610	01	07	16	18	22	24	33	39	08	15	25	32	40	47	P <sub>R</sub> -P <sub>SR</sub>			
27	123*	80	7.610	01	07	16	18	22	24	33	39	08	15	25	32	40	47	P <sub>R</sub> -P <sub>SR</sub>			
28	123*	80	7.610	01	07	16	18	22	24	33	39	08	15	25	32	40	47	P <sub>R</sub> -P <sub>SR</sub>			
29	123*	80	7.610	01	07	16	18	22	24	33	39	08	15	25	32	40	47	P <sub>R</sub> -P <sub>SR</sub>			
30	123*	100	11.890	01	07	16	18	22	24	33	39	08	15	25	32	40	47	P <sub>R</sub> -P <sub>SR</sub>		Removed shims (left ribbon 2 not as tight)	
31	123*	100	11.890	01	07	16	18	22	24	33	39	08	15	25	32	40	47	P <sub>R</sub> -P <sub>SR</sub>			
32	123*	100	11.890	01	07	16	18	22	24	33	39	08	15	25	32	40	47	P <sub>R</sub> -P <sub>SR</sub>			
33	123*	80	7.610	01	07	16	18	22	24	33	39	08	15	25	32	40	47	P <sub>R</sub> -P <sub>SR</sub>			
34	123*	80	7.610	01	07	16	18	22	24	33	39	08	15	25	32	40	47	P <sub>R</sub> -P <sub>SR</sub>			
35	123*	80	7.610	01	07	16	18	22	24	33	39	08	15	25	32	40	47	P <sub>R</sub> -P <sub>SR</sub>			
36	123	100	11.890	All Pressure Ports Connected to PSI System except Port 48 measured PR-PSR.																	
37	123	100	11.890	All Pressure Ports Connected to PSI System except Port 48 measured PR-PSR.																	
38	123	100	11.890	All Pressure Ports Connected to PSI System except Port 48 measured P <sub>R</sub> -P <sub>SR</sub> .																	
39	123	100	11.890	All Pressure Ports Connected to PSI System except Port 48 measured P <sub>R</sub> -P <sub>SR</sub> .																	
40	123	70	5.826	All Pressure Ports Connected to PSI System except PSI Port 27 measured P <sub>T</sub> -P <sub>SR</sub> , Port 30 measured P <sub>SP</sub> -P <sub>SR</sub> , Port 48 measured P <sub>R</sub> -P <sub>SR</sub> .															x	Evaluating PSI System Parameters	
41	123	80	7.610	All Pressure Ports Connected to PSI System except PSI Port 27 measured P <sub>T</sub> -P <sub>SR</sub> , Port 30 measured P <sub>SP</sub> -P <sub>SR</sub> , Port 48 measured P <sub>R</sub> -P <sub>SR</sub> .															x		
42	123	90	9.631	All Pressure Ports Connected to PSI System except PSI Port 27 measured P <sub>T</sub> -P <sub>SR</sub> , Port 30 measured P <sub>SP</sub> -P <sub>SR</sub> , Port 48 measured P <sub>R</sub> -P <sub>SR</sub> .															x		
43	123	100	11.890	All Pressure Ports Connected to PSI System except PSI Port 27 measured P <sub>T</sub> -P <sub>SR</sub> , Port 30 measured P <sub>SP</sub> -P <sub>SR</sub> , Port 48 measured P <sub>R</sub> -P <sub>SR</sub> .															x		
44	123	110	14.387	All Pressure Ports Connected to PSI System except PSI Port 27 measured P <sub>T</sub> -P <sub>SR</sub> , Port 30 measured P <sub>SP</sub> -P <sub>SR</sub> , Port 48 measured P <sub>R</sub> -P <sub>SR</sub> .															x		
45	123	110	14.387	All Pressure Ports Connected to PSI System except PSI Port 27 measured P <sub>T</sub> -P <sub>SR</sub> , Port 30 measured P <sub>SP</sub> -P <sub>SR</sub> , Port 48 measured P <sub>R</sub> -P <sub>SR</sub> .															x		
46	123	110	14.387	All Pressure Ports Connected to PSI System except PSI Port 27 measured P <sub>T</sub> -P <sub>SR</sub> , Port 30 measured P <sub>SP</sub> -P <sub>SR</sub> , Port 48 measured P <sub>R</sub> -P <sub>SR</sub> .															x		
47	123	80	7.610	All Pressure Ports Connected to PSI System except Port 48 measured P <sub>R</sub> -P <sub>SR</sub> .															x		
48	123	80	7.610	All Pressure Ports Connected to PSI System except Port 48 measured P <sub>R</sub> -P <sub>SR</sub> .															x		
49	123	80	7.610	All Pressure Ports Connected to PSI System except Port 48 measured P <sub>R</sub> -P <sub>SR</sub> .															x		
50	123	80	7.610	All Pressure Ports Connected to PSI System except Port 48 measured P <sub>R</sub> -P <sub>SR</sub> .															x		
51	123	80	7.610	All Pressure Ports Connected to PSI System except Port 48 measured P <sub>R</sub> -P <sub>SR</sub> .															x		
52	123	100	11.890	All Pressure Ports Connected to PSI System except Port 48 measured P <sub>R</sub> -P <sub>SR</sub> .															x	PSI Data Pressure Sensitive Paint Data	
53	123	100	11.890	All Pressure Ports Connected to PSI System except Port 48 measured P <sub>R</sub> -P <sub>SR</sub> .															x		
54	123	100	11.890	All Pressure Ports Connected to PSI System except Port 48 measured P <sub>R</sub> -P <sub>SR</sub> .															x		
55	123	100	11.890	All Pressure Ports Connected to PSI System except Port 48 measured P <sub>R</sub> -P <sub>SR</sub> .															x		
56	123	100	11.890	All Pressure Ports Connected to PSI System except Port 48 measured P <sub>R</sub> -P <sub>SR</sub> .															x		

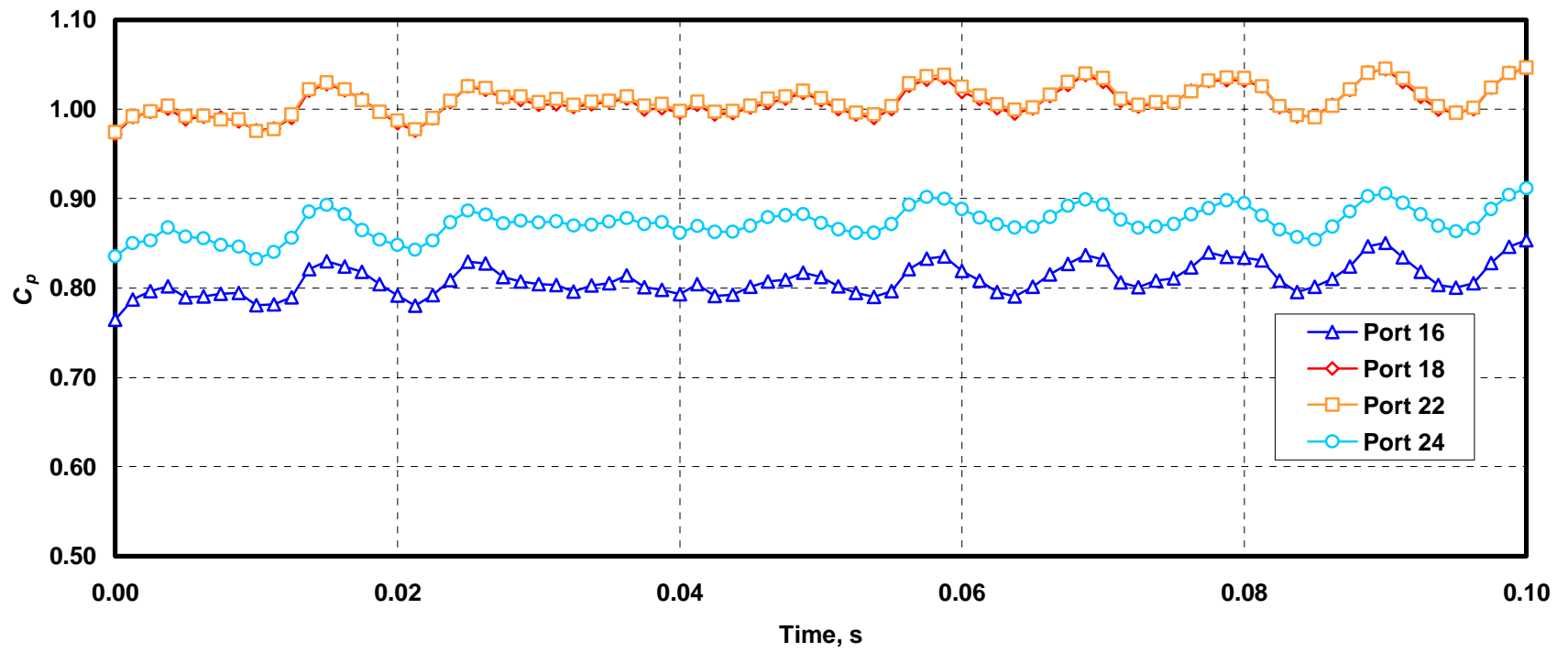


Figure 12. Typical time-accurate pressures on windward side (Run 19).

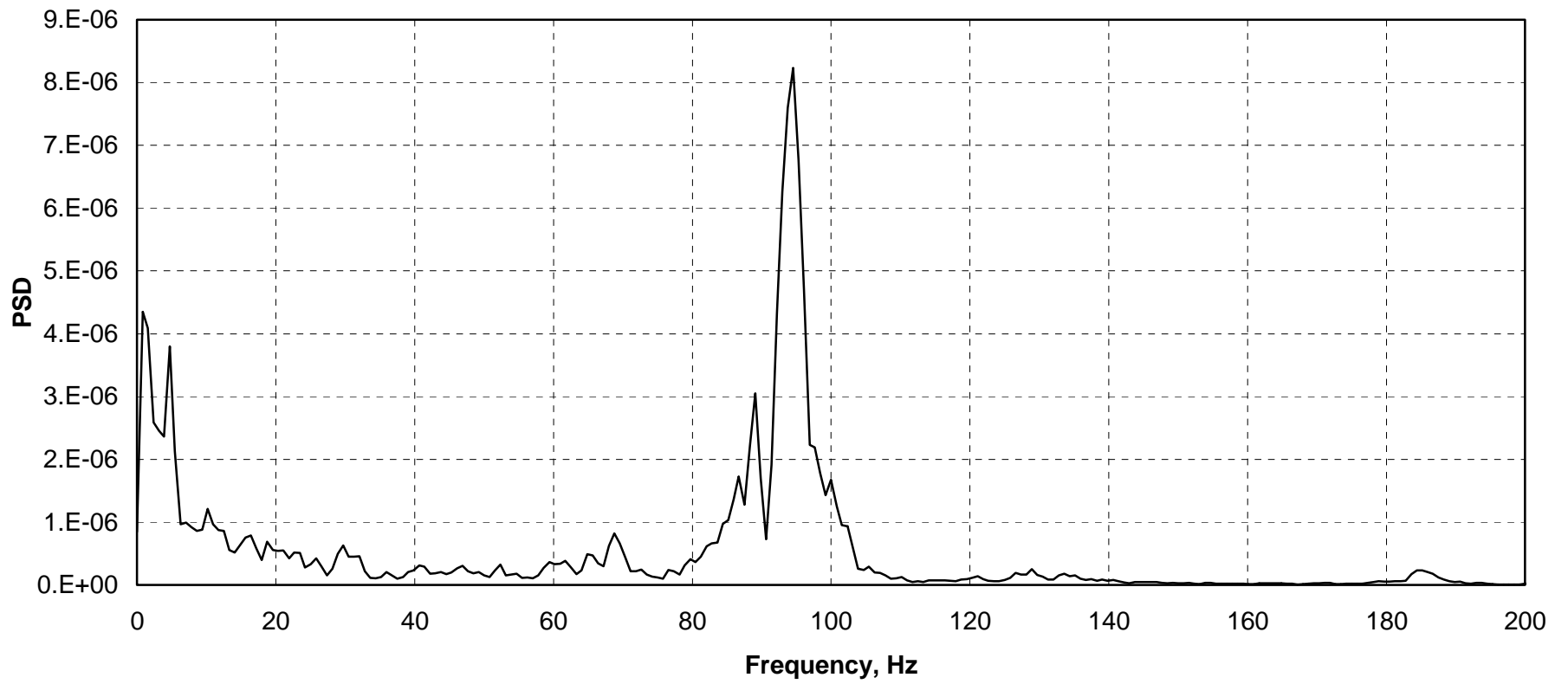


Figure 13. Typical Power Spectral Density (PSD) of pressure on windward side (Port 22, Run 19).

A subsequent experiment was conducted, back at Sandia, on the actual stainless steel ribbon with the same Tygon tubing connections to the transducer. An air hose was discharged at the pressure port from all angles without exciting such a resonance. It was concluded that friction in the very small I.D. tubing dissipated any organ pipe resonances.

A wind-off measurement was made in which the ribbon was “twanged” to determine if the frequency spike was due to the mechanical resonant frequency of the installation (recall that the tension was applied by compressing springs). No frequency spike was encountered.

We now believe that the frequency spike at approximately 95 Hz (we found it at various frequencies between 93.8 and 96.1 Hz on various runs) was due to the primary wind tunnel resonance which can be calculated using a formula for room resonance due to Kuttruff<sup>2</sup>,

$$f = (c/2) \left[ (l/L)^2 + (w/W)^2 + (h/H)^2 \right]^{1/2} \quad (16)$$

$$l, w, h = 0, 1, 2, \dots$$

where for our case,

$f$  = Resonant frequency, Hz

$c$  = Speed of sound (1117.4 ft/s at 60°F)

$W$  = Width of room (10 ft)

$H$  = Height of room (7 ft)

$L$  = Length of room (very large number for a wind tunnel, assumed to be  $\infty$ )  
(Note that while the length of the test section was 20 ft, this figure is not applicable since the test section has open ends.)

Using Equation 16 with  $w$  and  $h$  set to 1 (fundamental harmonic for both width and height), we found the primary resonance for the tunnel to be 97.4 Hz.

Two other significant frequency spikes that continually reoccurred but were independent of velocity and, therefore, probably tunnel related, were found at approximately 32 and 70 Hz.

A careful, and perhaps imaginative, perusal of the PSD curves including the set of runs used to calibrate the tunnel which included the velocity range from 70 to 110 ft/s showed only one frequency spike which seemed to be linearly dependent on velocity and it varied from approximately 11 Hz at 70 ft/s to approximately 25 Hz at 110 ft/s. While we initially thought this indicated vortex shedding from the 7-inch wide three-ribbon configuration at a Strouhal number of 0.104, subsequent PSD analysis of the pitot pressure measured on those same runs indicates the same frequency spike. Since the pitot probe was located two ft ahead of the ribbons, we became convinced that this frequency spike was also tunnel related (associated with the fan or possible vortex shedding off the tunnel turning vanes).

### **Particle Image Velocimetry Measurements**

On runs 19 through 35, Particle Image Velocimetry (PIV)<sup>3,4,5</sup> measurements were made of the flow field immediately downstream of the ribbons. These measurements were made at a frequency of 14.8 measurements/s. The laser light sheet was introduced through a window in the top of the wind tunnel and directed, on centerline, to an area that spanned approximately 1 ft downstream of the ribbons. The digital camera that recorded the particle movement viewed the field through a window in the control room side splitter plate and viewed a field that

spanned from approximately 0.15 in. downstream of the ribbons to 9.65 in. downstream and from 1.75 in. above the top ribbon to 1.40 in. below the bottom ribbon. The PIV analysis software analyzed this field at 20,139 points on a 137 x 147 grid equally spaced at 0.06963 in. in both  $x$  and  $y$  dimensions respectively (It should be noted here that the PIV analysis assumed a different coordinate system than that previously mentioned. The PIV coordinate system assumed an  $x$  axis that started at the windward surface of the ribbons and extended downstream and a  $y$  axis that started at the midpoint of the center ribbon and extended upwards.)

The data, after being analyzed at NASA Ames was shipped to us as “zipped” files on CD’s. (These CD’s have been delivered to Steven Kempka, 9111, who presently has them on file.) Each CD has a collection of libraries, each of which contain approximately 101 zipped files. One hundred of these files, when unzipped, contain instantaneous velocity data at each of the 100 times at which data was taken over a 6.75 s span at about the beginning of each run. The PIV system sent a pulse to the pressure measuring system at each instant data was taken. Thus this pulse (referred to above, and recorded in the last column of the unsteady pressure data files) correlated the velocity field data with the unsteady pressure data. The other file, when unzipped, contains averages of the velocity data taken in the 100 instantaneous data runs.

Each data file is written in ASCII Tecplot<sup>®</sup> “point” input file format with IJ-ordered data and corresponds to one time-specific velocity field. It should be noted that there is no time identification associated with the file, other than its name which establishes a rather arcane method of identifying the time signature. This identification method is as follows:

“**runAABBB\_X\_AACCC.VEC**” is the PIV data file taken  $t$  seconds from the beginning of run  $AA$ , where  $BBB$  and  $CCC$  refer to the sequential PIV digital photographs taken nanoseconds apart,

$$t = [(BBB/2)/14.8] + t_i \quad (17)$$

where  $t_i$  = time when PIV sync signal first went high on run  $AA$ .

Following two rows of header information, which is in the proper format for Tecplot use, 8 columns x 20,139 rows contain the following data:  $x$ ,  $y$ ,  $u$ ,  $v$ ,  $\partial u/\partial x$ ,  $\partial u/\partial y$ ,  $\partial v/\partial x$ ,  $\partial v/\partial y$ . We found that the last four columns of partial derivative data is in error by a factor of approximately 1000. Subsequent communications with NASA Ames personnel have shed no light on the cause of the error except to appraise us of the fact that the raw data was smoothed onto a surface in a manner due to Lourenco and Krothapalli<sup>6</sup>. We used a simple centered-differencing scheme to obtain the values used in subsequent plots.

Figure 14 displays the velocity vector plot taken at 0.125 seconds in Run 19 (the run whose pressure is plotted in Figure 12. This plot was created in Excel through the use of a macro which has been delivered to Steven Kempka, 9111. The velocity vectors are plotted as lines which are blue if the  $u$  component is positive and red if it is negative. A velocity scale is shown on the plot and the geometric scale can be obtained from the ribbons which are 2" wide.

Figure 15 displays the vorticity field,  $\omega_z$ , calculated from the previous velocity field by,

$$\omega_z = \frac{\partial v}{\partial x} - \frac{\partial u}{\partial y} \quad (18)$$

The color scale is shown to the right and has been scaled by the maximum (or minimum) vorticity. Figures 16 and 17 are velocity vector and vorticity field plots for the average of all the PIV data files (100) taken during Run 19.

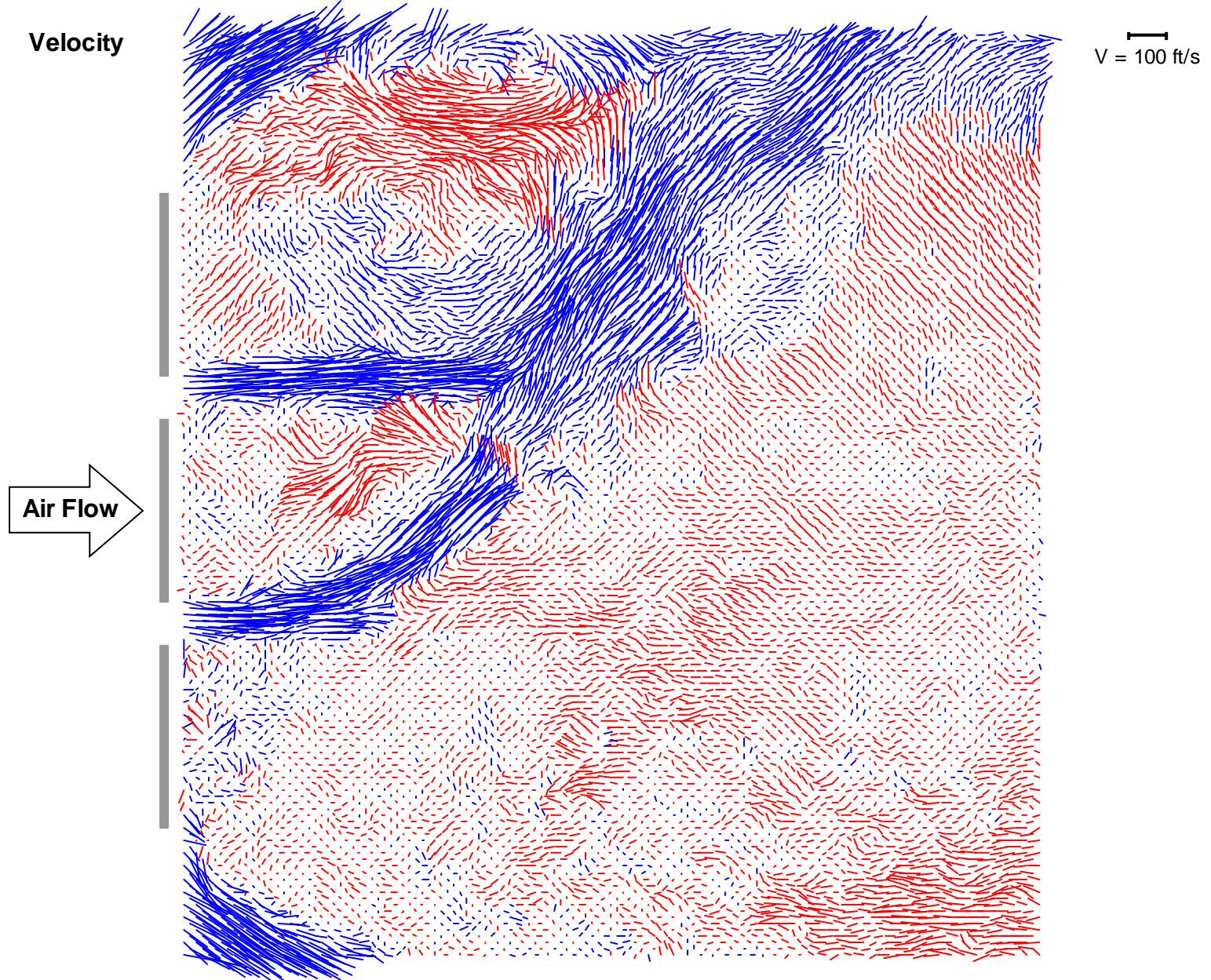


Figure 14. Velocity field measured with PIV system ( $t = 0.125$  s, Run 19).

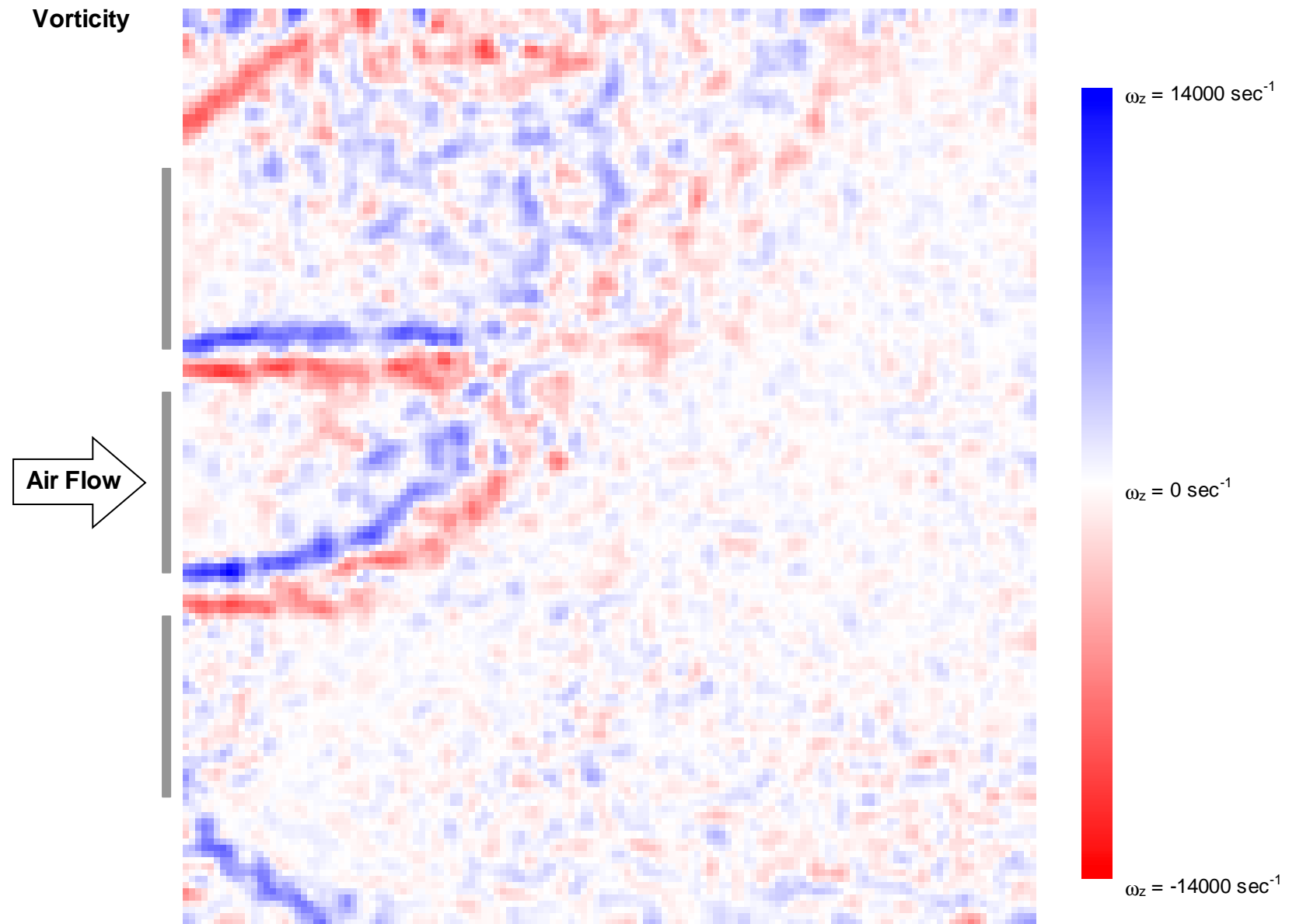


Figure 15. Vorticity field measured with PIV system ( $t = 0.125 \text{ s}$ , Run 19).

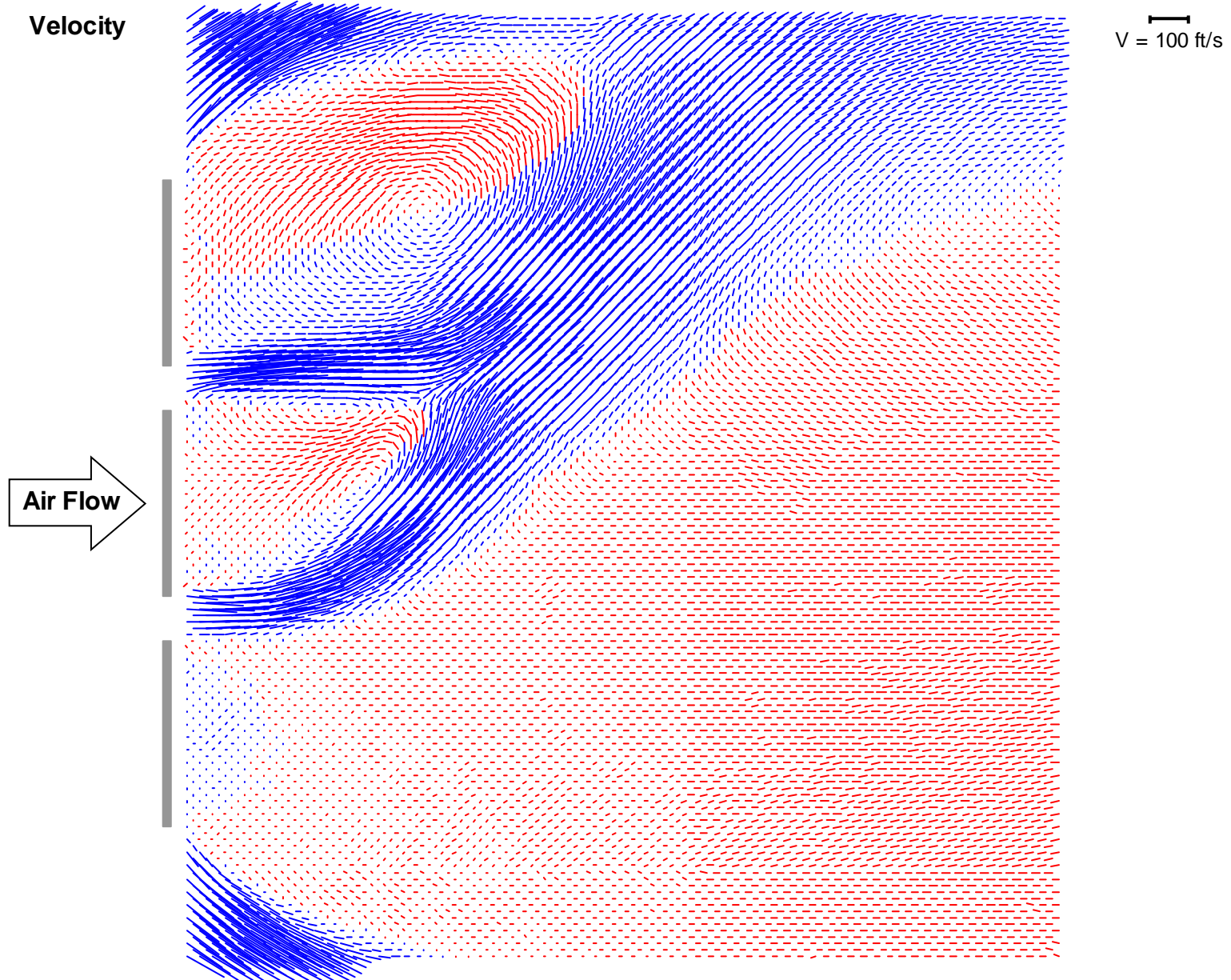


Figure 16. Average velocity field measured with PIV system (average of 100 fields, Run 19).

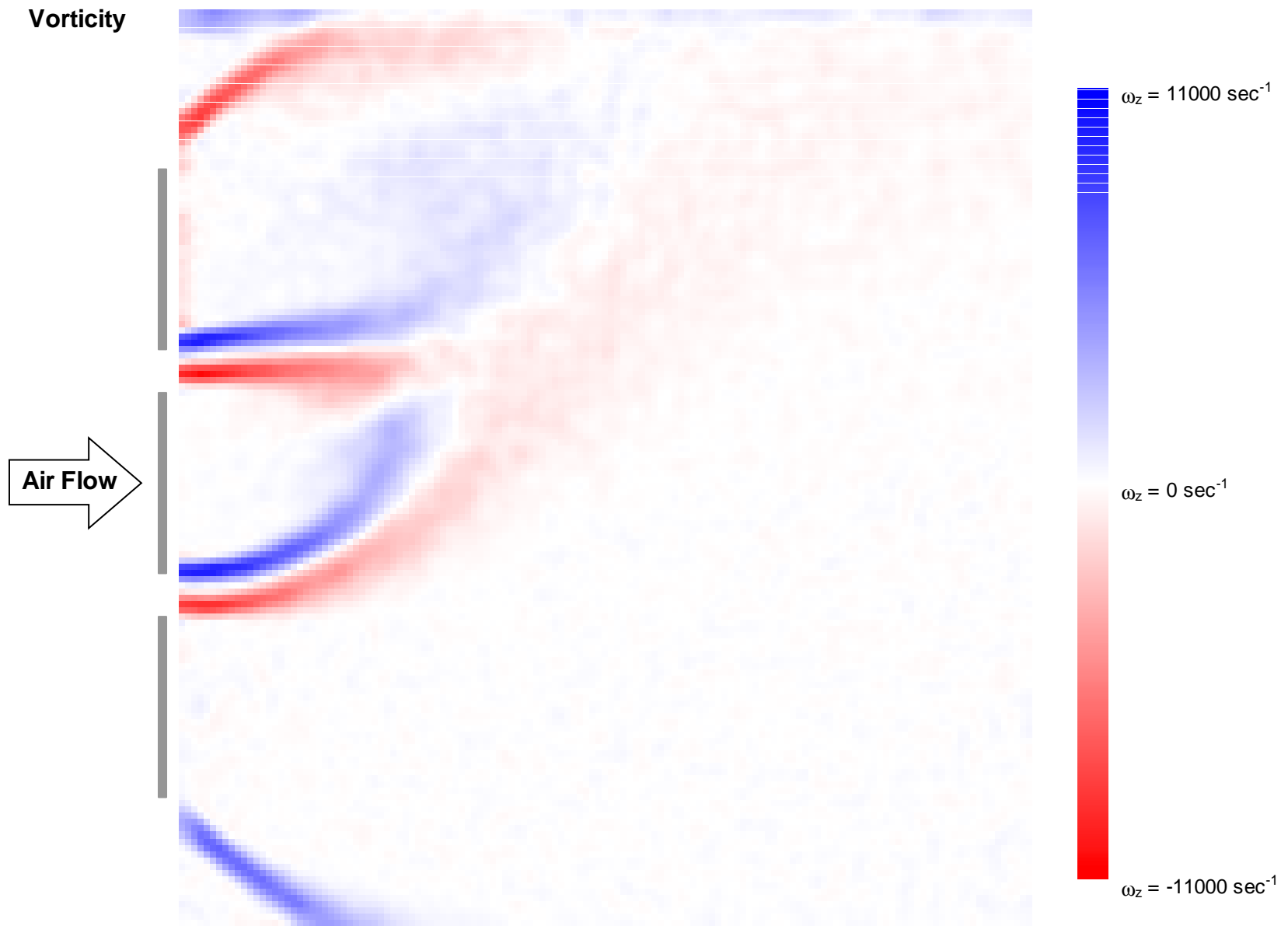


Figure 17. Average vorticity field measured with PIV system (average of 100 fields, Run 19).

It can be seen from Figure 14 that the flow field was asymmetrical. The jet issuing from the bottom slot attached itself to the jet issuing from the upper slot and the resulting jet moved to the high velocity field at the top of the wake. We had expected that this might happen, but thought that the jet would flip from the upper edge of the wake to the lower in a periodic manner, establishing a vortex-street type of wake. This did not happen. The wake veered upwards for the entire test as can be established by looking at Figure 16. The reason for this bias is not known. It is speculated that some very minor asymmetry in the tunnel flow caused the wake to assume the stable configuration in the upward direction.

This asymmetry seemed to feed back into the overall dynamic pressure,  $q$ . Figure 18 shows a 4<sup>th</sup> order polynomial fit to the values of  $q$  measured on the vertical centerline of the tunnel at the leading edge of the splitter plates with the stainless steel ribbons installed.

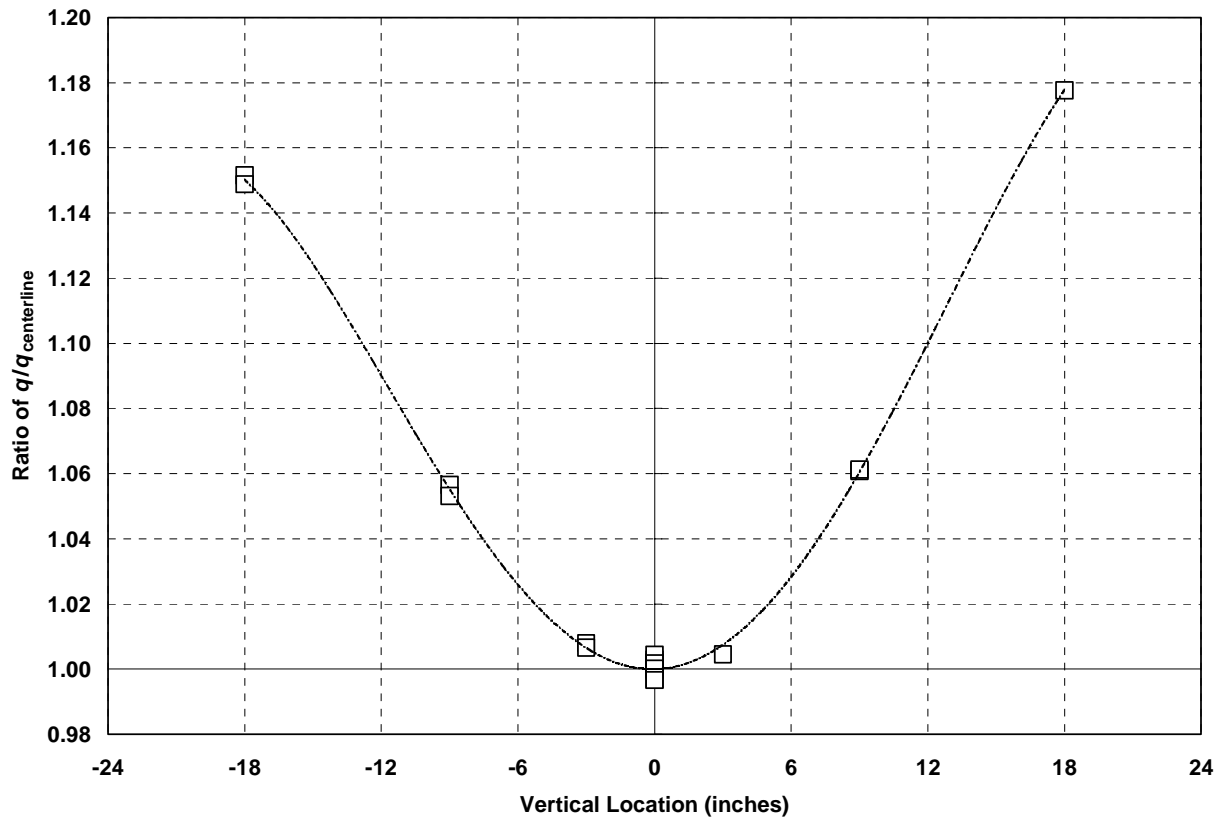


Figure 18. Dynamic pressure distribution on tunnel centerline with model installed.

It can be seen that there is a definite bias of about 2% on the upper side of the ribbons. We feel that this nonuniformity is due to the upward sweeping wake rather than vice-versa. While we did not run a tunnel  $q$  calibration with the ribbons removed, we feel confident that the distribution would have been much more symmetric. We did not check flow angularity at the front edge of the splitter plates, either with or without the ribbons installed, although in retrospect it would have been very valuable information.

Additional information is obtained by looking at the PIV data from a later series of runs in which the stainless steel ribbons were replaced with regular 1000 lb nylon ribbons. This was done in runs 57, 58, and 59. Table 5 lists the run schedule for this series of runs.

Table 5. Run Schedule for Nylon Ribbons with PIV

Run #	Config #	V (ft/s)	$q$ (psf)	Ribbon Total Tension (lb)	Remarks
57	Nylon	80	7610	490	Ribbons broke
58a	Nylon	100	11890	600	
58b	Nylon	100	11890	640	
58c	Nylon	100	11890	680	
59a	Nylon	80	7610	640	
59b	Nylon	80	7610	720	
59c	Nylon	80	7610	750	

Run 57, conducted at 80 ft/s tunnel velocity, was aborted when the ribbons broke at the mounting fixture. Some data was obtained prior to breakage, but it will not be reported since the test was rerun with a revised mounting procedure. Inspection of the torn ribbons indicated they had abraded at the mounting point, so the clamping fixture was smoothed prior to Run 58.

Run 58, conducted at 100 ft/s tunnel velocity, shows a much more symmetrical wake. Figures 19 through 21 show the average velocity field associated with the 100 instantaneous PIV measurements for each of three ribbon tensions — 600 lb, 640 lb, and 680 lb total tension, respectively. It is interesting to note that the ratio of the average  $v$  component of velocity (over the entire wake area) to the average  $u$  component indicates a flow angularity of approximately  $+2^\circ$ . This amount of flow angularity in the 7- by 10-ft Wind Tunnel is certainly possible in the presence of the 7% flow blockage in the part of the test section between the two splitter plates and the initial establishment of the wake in the upward condition, and could account for the continuously upwardly-biased wake seen with the stainless steel ribbons. The “fluttering” nylon ribbons, however, added enough instability to the flow to cause the wake to flip from side to side (see Figure 22a-c).

It should be noted that the PIV data was displaced downwards by 0.306 in. for Runs 58 and 59. The reason for this was that we noted that the jets issuing from the ribbon gaps did not line up with the gaps themselves. Upon examining Run 57 we found that the jets did, in fact, line up with the gaps for that run. We surmised that something in the PIV setup must have been disturbed during the time that the broken ribbons were being replaced. To account for this, we added a displacement factor into the  $y$  position that aligned the center of the gaps with the average center for the jets in all the runs subsequent to Run 57.

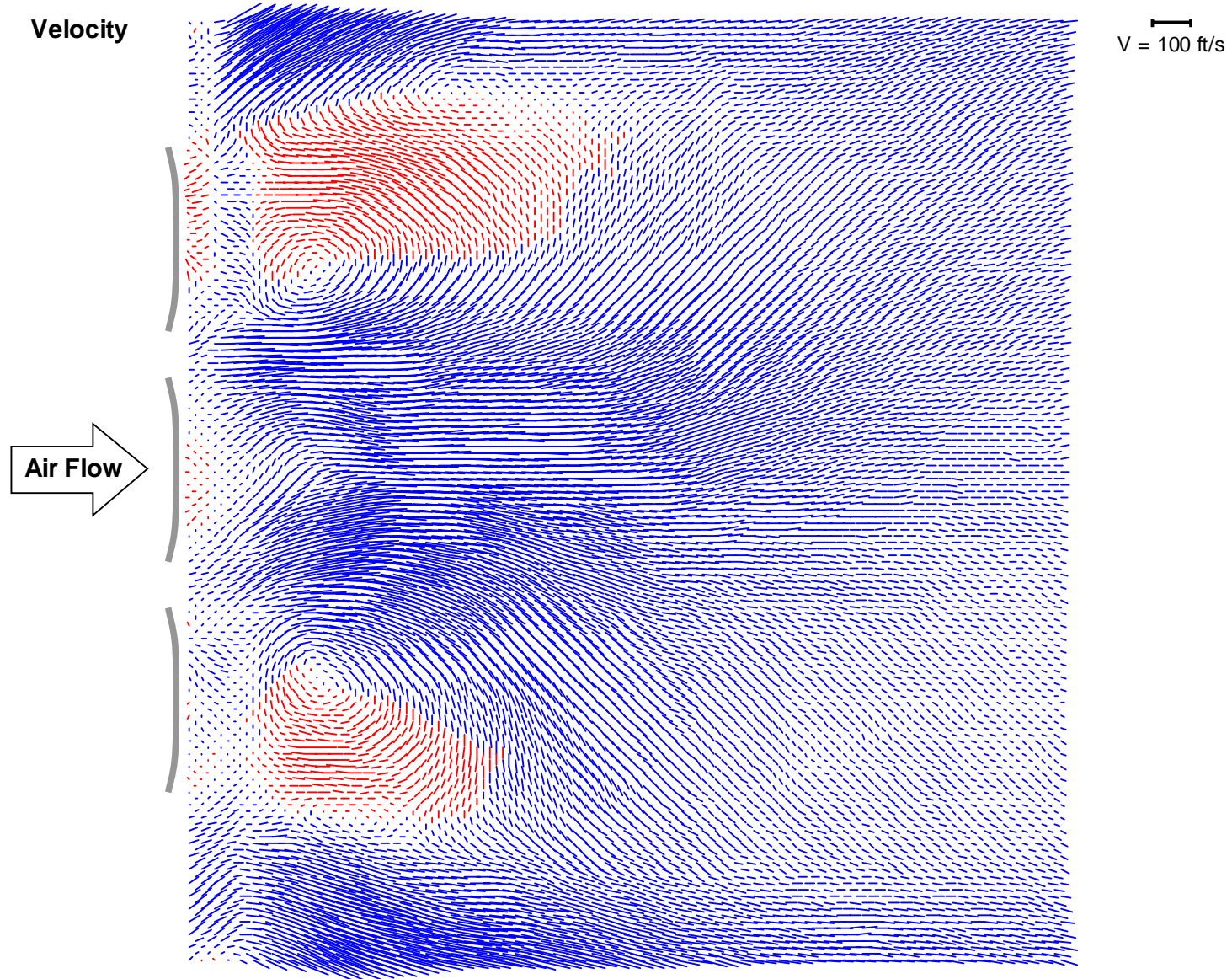


Figure 19. Average velocity field behind fabric ribbons tensioned to 600 lb total tension.

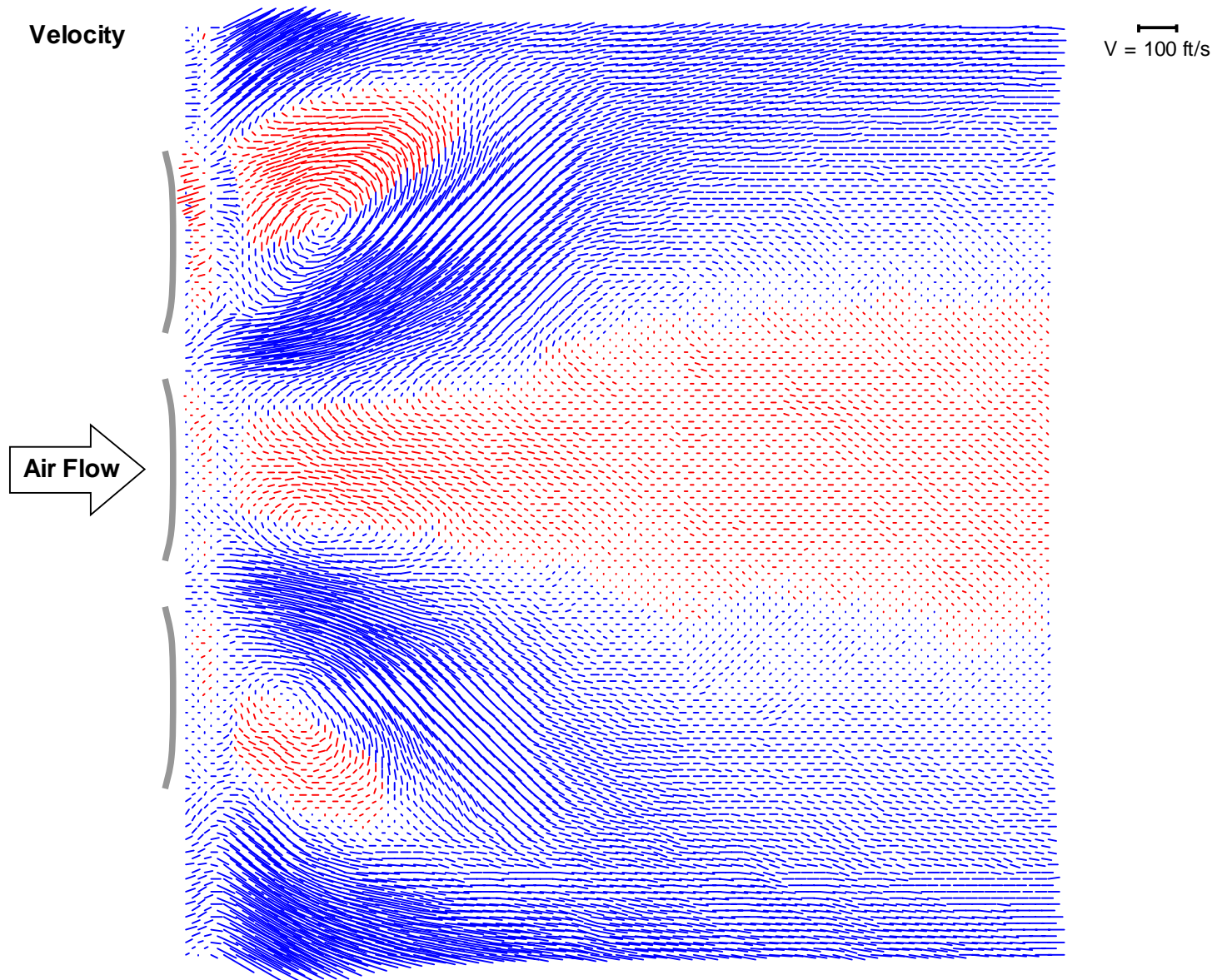


Figure 20. Average velocity field behind fabric ribbons tensioned to 640 lb total tension.

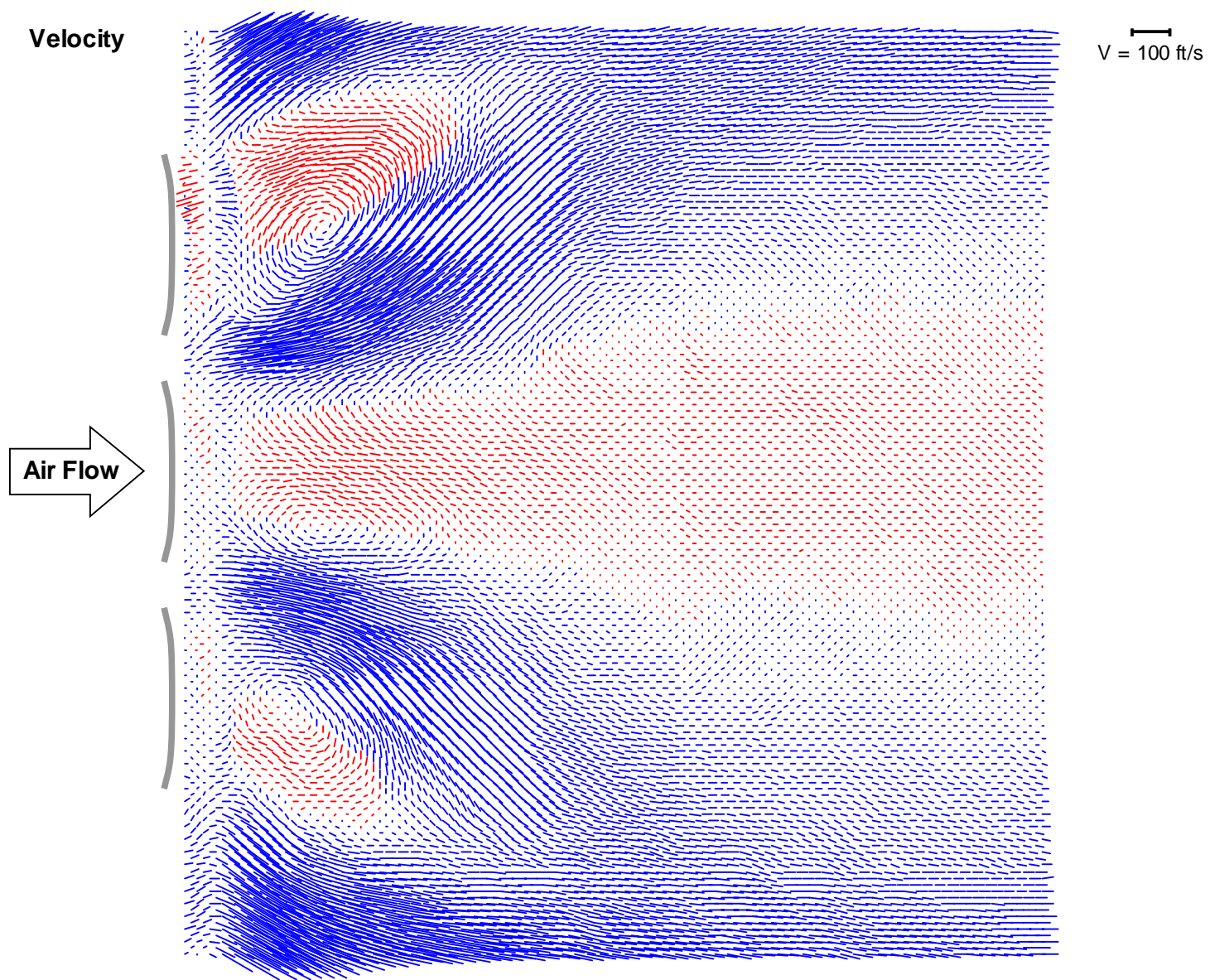


Figure 21. Average velocity field behind fabric ribbons tensioned to 680 lb total tension.

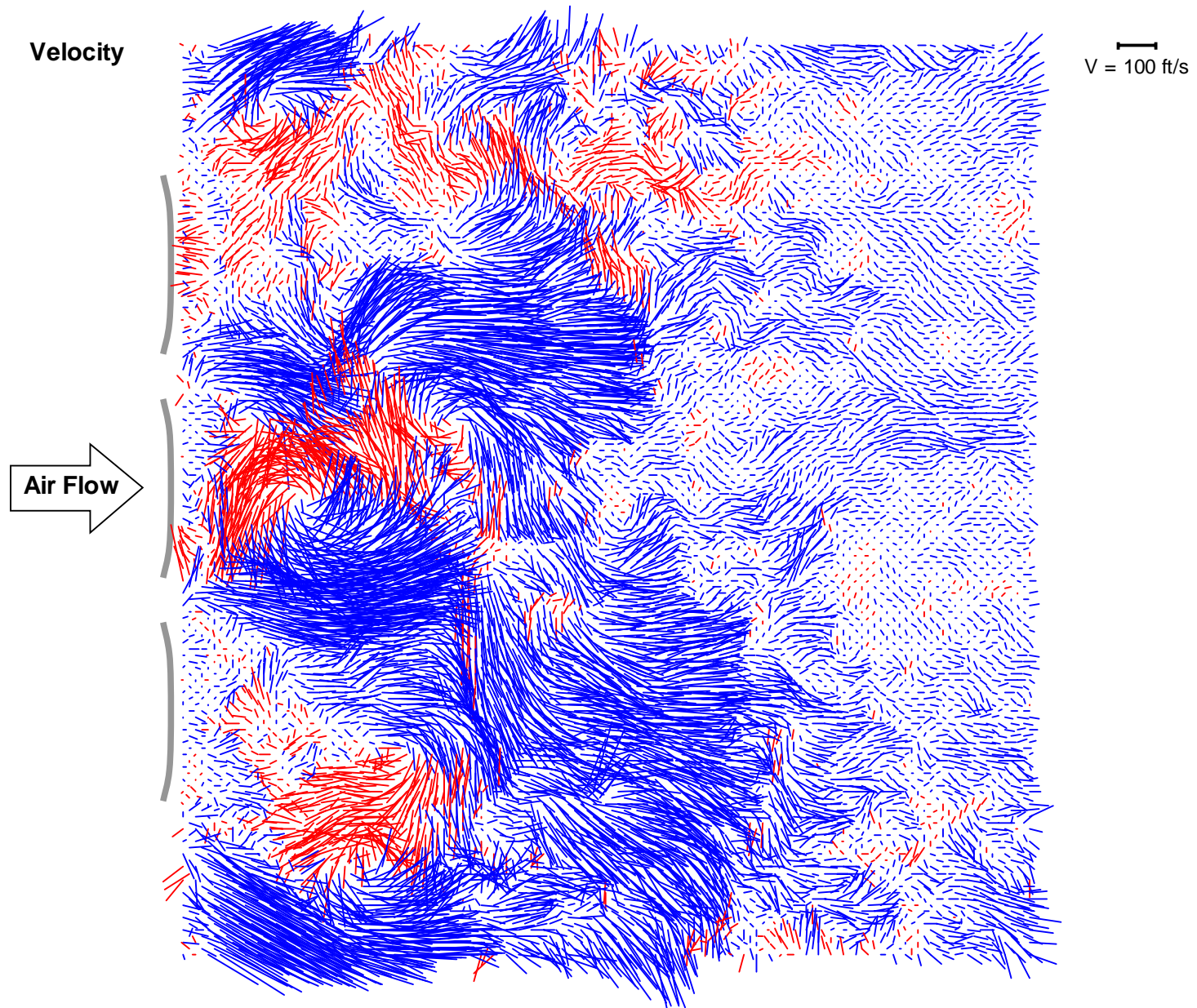


Figure 22a. Velocity field behind fabric ribbons tensioned to 600 lb ( $t \approx 0.125$  s).

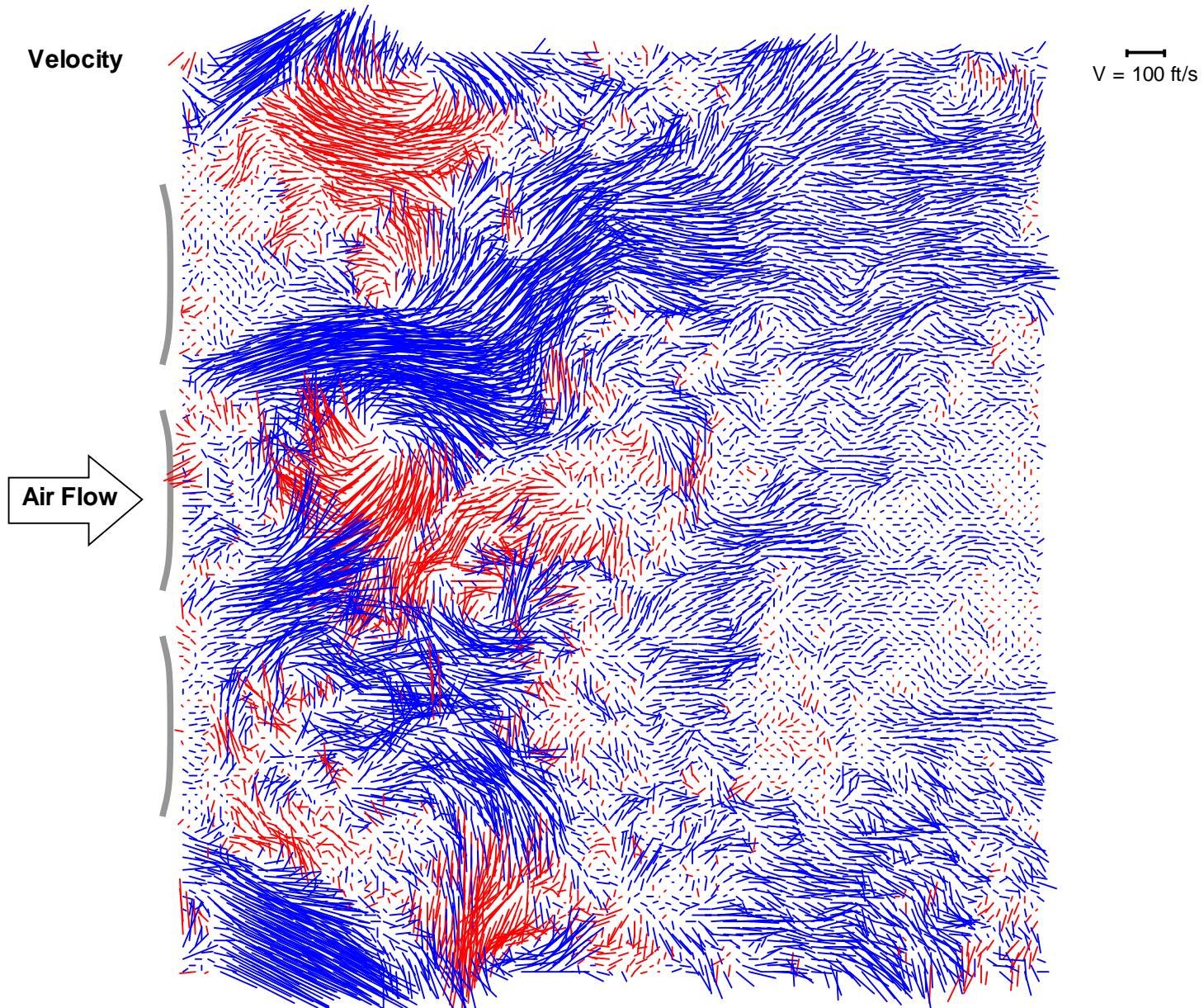


Figure 22b. Velocity field behind fabric ribbons tensioned to 600 lb ( $t \approx 0.193$  s).

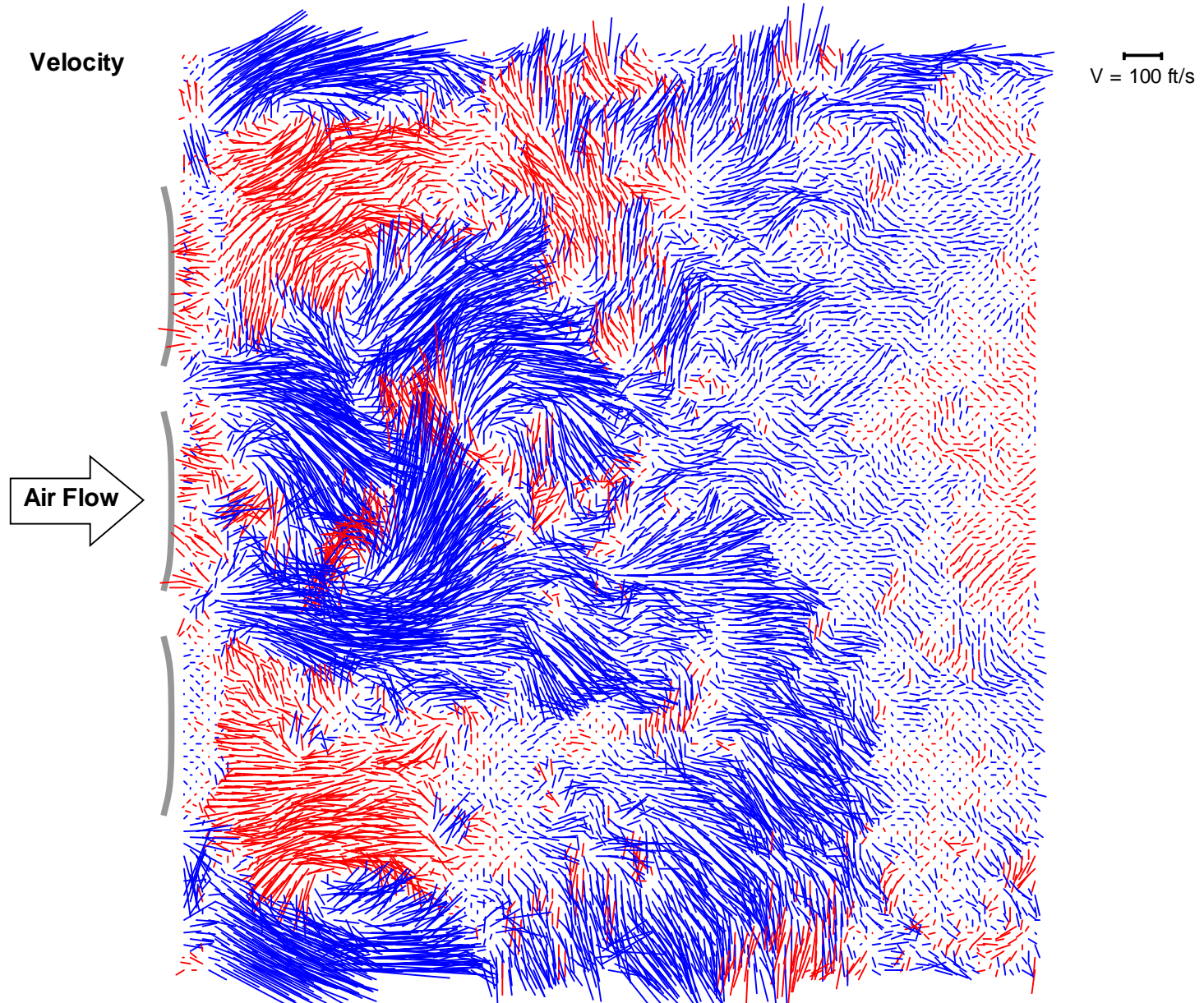


Figure 22c. Velocity field behind fabric ribbons tensioned to 600 lb ( $t \approx 0.260$  s).

## Steady-State Pressure Measurements

This portion of the test was comprised of Runs 47 through 56, in which the time-averaged pressure was measured at all 47 pressure ports. Five runs were made at each of the two nominal wind tunnel test velocities, 80 and 100 ft/s. Figures 23 and 24 show plots of the average measured  $C_p$ 's for these runs. The effect of the asymmetric wakes are clearly seen in the data with substantially higher leeward pressures (lower *negative*  $C_p$ 's) being measured in the wake of ribbon 3 (the bottom ribbon). While error bars on the PSI data are plotted in these figures, they are obscured by the data symbols. Averages of the unsteady Endevco data are also plotted in these figures, with their error bars, and show exceptional agreement with the steady-state PSI data.

It is obvious that any attempt to duplicate these results with a computer code must assume a small flow angularity. As flow angularity was not measured during the setup of the test, a validation calculation does not make much sense (as indicated in the Introduction, accurate measurements of the boundary conditions is a prerequisite for validation purposes.) Another short tunnel entry, made primarily for the purpose of measuring flow angularity in the presence of the model (with the flow blockage it causes) should give valid boundary conditions for such a validation effort. In the absence of such measurements, it is suggested that a flow angle of  $+2^\circ$  might be a reasonable estimate for calculations for informative (as opposed to validation) purposes.

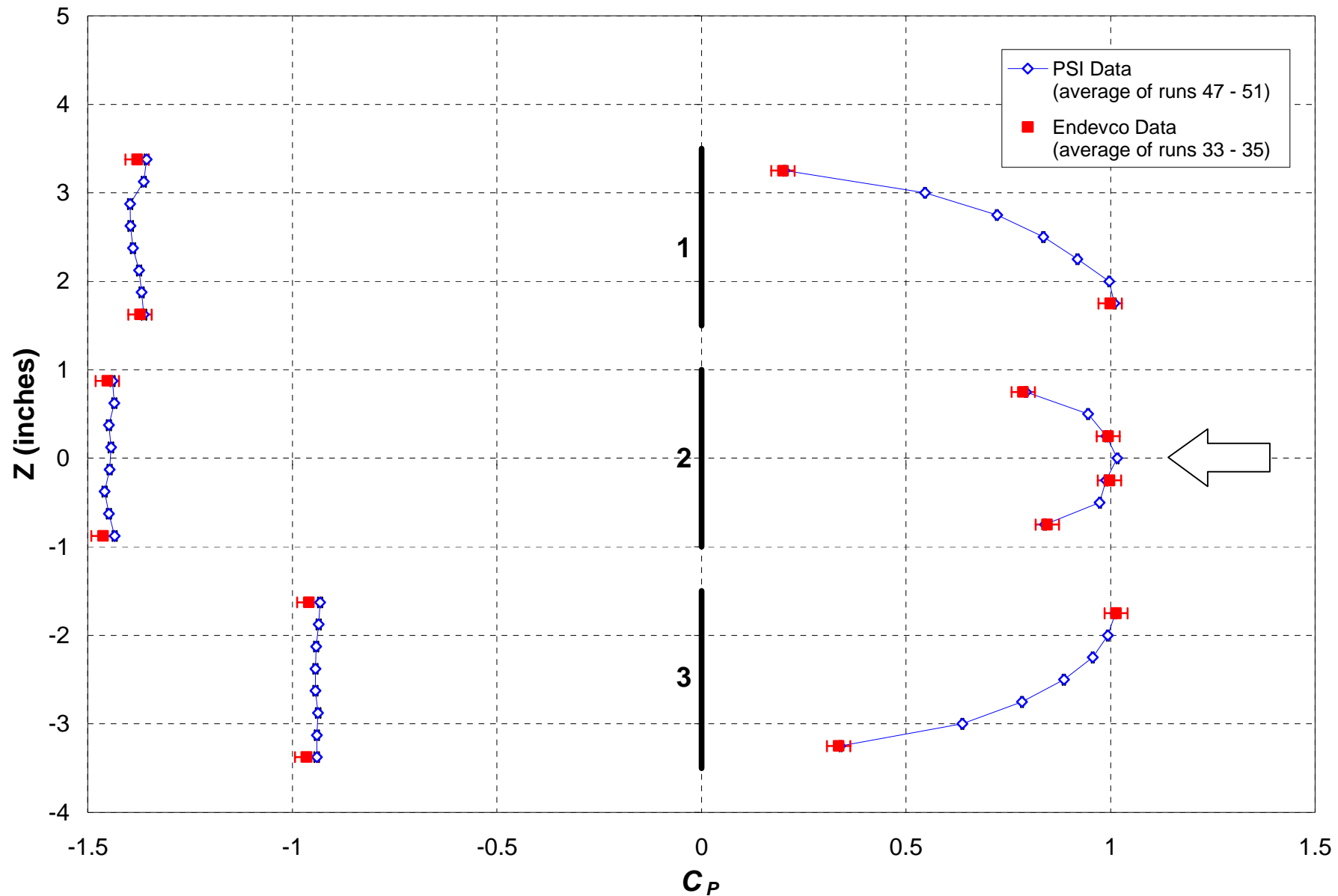


Figure 23. Comparison of steady-state (PSI) with averaged unsteady (Endevco)  $C_p$ 's at a nominal velocity of 80 ft/s.

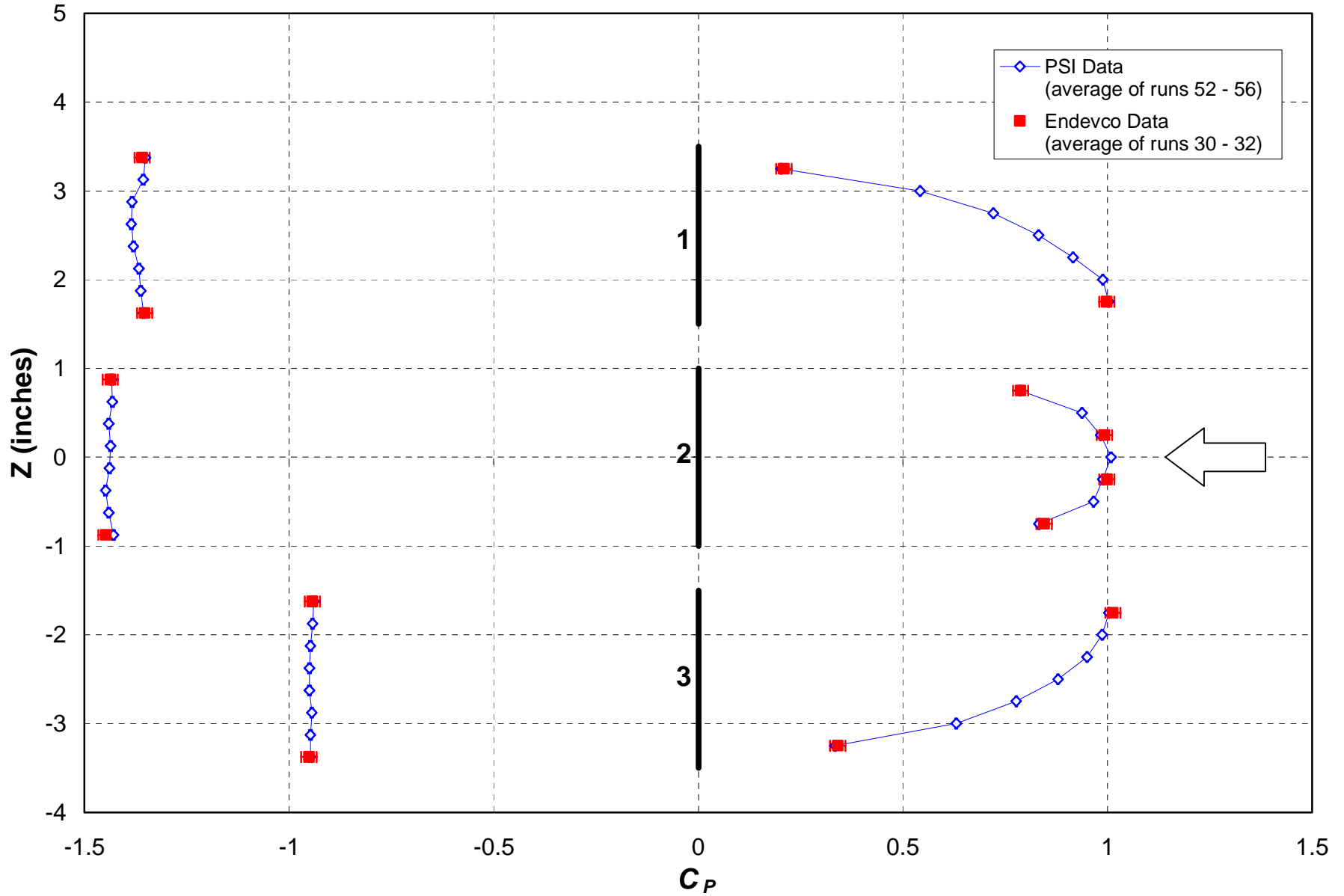


Figure 24. Comparison of steady-state (PSI) with averaged unsteady (Endevco)  $C_p$ 's at a nominal velocity of 100 ft/s.

## RECOMMENDATIONS

The asymmetry of the wake, shown by both the steady-state pressure measurements and the PIV results along with the skewed distribution of tunnel dynamic pressure, indicate a flow angularity at the inlet to the two-dimensional section. Since one of the prerequisites for using data for validation purposes is an accurate knowledge of the boundary conditions, it is NOT recommended that the steady-state data reported here be used for validation purposes. It is, however, recommended that additional funding be sought to reenter the NASA 7- x 10- Foot, Subsonic Wind Tunnel Number 1 for the purpose of establishing the boundary conditions extant at the time of this test. All of the hardware is still available, as are two very sensitive and accurate flow angularity probes. These probes could be used to map the flow angularity at the plane established by the leading edges of the two splitter plates in the presence of the stainless steel ribbon model. We further recommend the ribbon mounting frames be redesigned to allow for independent tensioning of the ribbons to assure equality of tension across the three ribbons. Retaking some of the steady-state data would then establish the error in the present data set that could be attributed to misalignment due to unequal tension.

Due to the fact that the primary use of the NASA 7- x 10- Foot, Subsonic Wind Tunnel Number 1 by the Army is for acoustic studies on helicopters, we find it surprising that the unsteady surface pressures on the stainless steel ribbons were apparently so extremely sensitive to the tunnel acoustics (if tunnel acoustics were, indeed, the cause of the spikes in the PSD data, as discussed above). However, in the face of that data, it is NOT recommended that any of the unsteady pressure data be used to infer frequency content or statistical variation of flow over ribbons for either the purpose of code validation or even knowledge base. If the validity of VIPAR is felt to depend upon its capability to predict not only average ribbon pressures but their correct statistical properties as well (i.e., variance, frequency content, etc.), any validation tests oriented toward obtaining these properties should be run in a wind tunnel whose acoustical properties have been shown to be compatible with that objective.

## REFERENCES

- <sup>1</sup> “Guide for the Verification and Validation of Computational Fluid Dynamics Simulations,” AIAA G-077-1998, Reston, VA, 1998.
- <sup>2</sup> Kuttruff, Heinrich, *Room Acoustics*, Elsevier Applied Science, New York, 1991.
- <sup>3</sup> Heineck, J. T., “3D PIV in Wind Tunnel Applications: Measurements of a Truck Wake,” *SAE/AIAA World Aviation Congress*, San Francisco, CA, 1999.
- <sup>4</sup> Heineck, J. T., “The Application of Three-Component PIV to a Hovering Rotor Wake” *AHS Forum 56*, Virginia Beach, VA, 2000.
- <sup>5</sup> Walker, Steve, “Large Scale Three Dimensional Particle Image Velocimetry Study of Wing Tip Vortices,” PhD Dissertation, Stanford University, 1999.
- <sup>6</sup> Lourenco, L. M. and Krothapalli, A., “Mesh-free, Second-Order Accurate Algorithm for PIV Processing,” *Proceedings of VSJ-SPIE98*, Yokohama, Japan, 1998.



## APPENDIX A

### CALCULATION OF PRESSURE COEFFICIENT, $C_P$

The pressure coefficient,  $C_p$ , is defined as

$$C_{p_i} = \frac{P_i - P_\infty}{q_\infty} \quad (\text{A-1})$$

where  $p_i$  is the  $i^{\text{th}}$  pressure,  $p_\infty$  is the freestream static pressure, and  $q_\infty$  is the freestream dynamic pressure. For this test, we defined the freestream quantities directly from pitot-static probe measurements 18 inches upstream of the center of the model ( $X = 18$  in.,  $Y = 0$ ,  $Z = 0$ ). The pitot-static probe is shown in Figures 4 and 7, and was removed prior to model testing. This approach compensated for local dynamic pressure variations due to model blockage. Then,  $p_\infty \equiv p_{sp}$ , where  $p_{sp}$  was the pitot-static probe static pressure and  $q_\infty \equiv q_p = p_{tp} - p_{sp}$ , where  $p_{tp}$  was the probe total pressure. Thus,

$$C_{p_i} = \frac{P_i - P_{sp}}{q_p} \quad (\text{A-2})$$

Because the pitot-static probe could not be on the centerline of the model during testing, the centerline probe measurements were correlated with the differential pressure measurement,  $p_r - p_{sr}$ , which is used to define tunnel operating dynamic pressure. The reference pressure,  $p_r$ , is measured in the contraction section, with six manifolded wall static ports. The static ring pressure,  $p_{sr}$ , is measured in the test section, 117 inches upstream of the model, with four manifolded wall static ports. This pressure was also used as the reference pressure for all of the model differential pressure measurements. Modifying the pressure coefficient to incorporate these measurements gives,

$$C_{p_i} = \frac{(p_i - p_{sr}) - (p_{sp} - p_{sr})}{q_p} \quad (\text{A-3})$$

Calibrations were performed with both pressure systems to define the relationship between the centerline test conditions and the reference pressure,  $p_r - p_{sr}$ , that is,

$$p_{sp} - p_{sr} = k_1 (p_r - p_{sr}) \quad (\text{A-4})$$

and

$$q_p = k_2 (p_r - p_{sr}) \quad (\text{A-5})$$

Finally, Equation (A-3) becomes

$$C_{p_i} = \frac{(p_i - p_{sr}) - k_1 (p_r - p_{sr})}{k_2 (p_r - p_{sr})} \quad (\text{A-6})$$

Results of the  $k_1$  and  $k_2$  calibrations are presented in Figures A-1 through A-4 and are summarized in the table below:

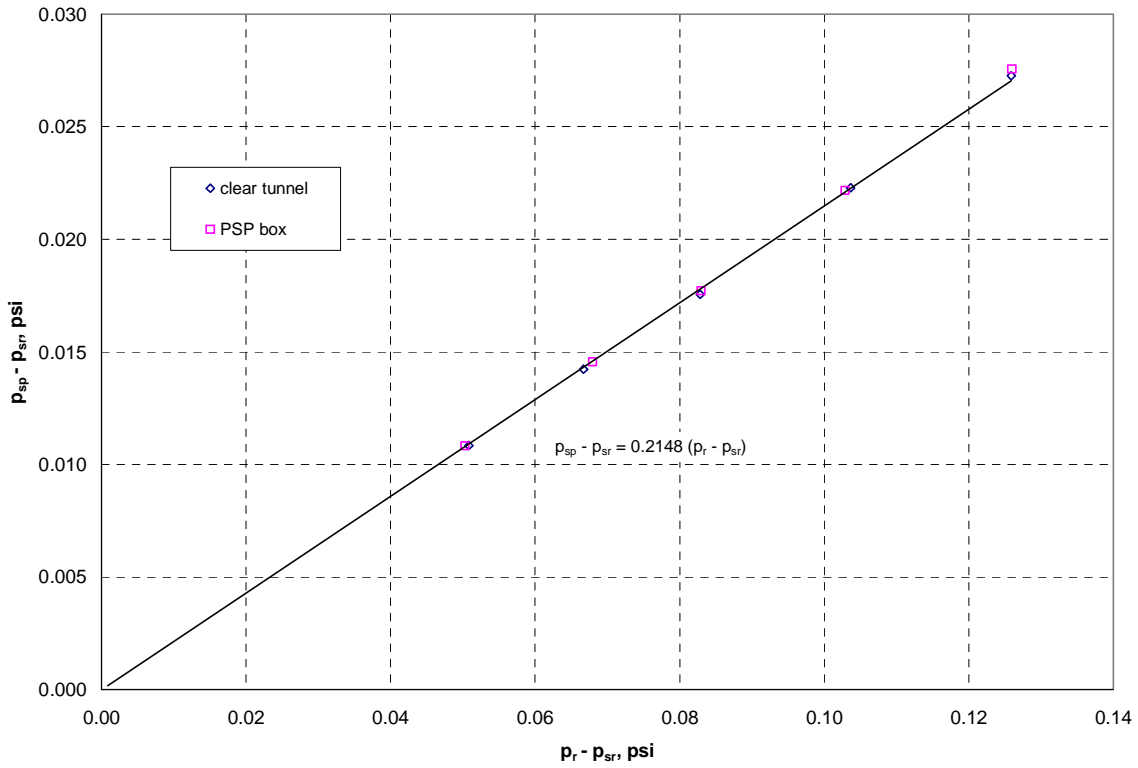


Figure A-1. Endeveco pitot-static tube static pressure calibration

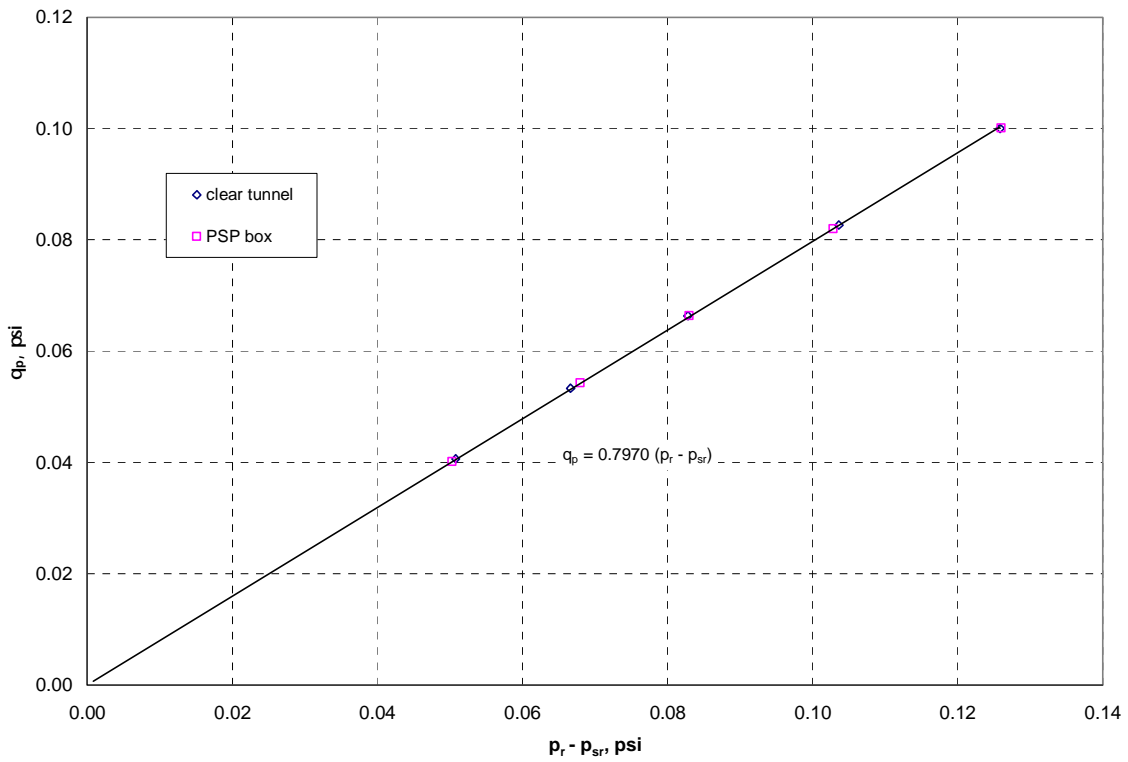


Figure A-2. Endeveco pitot-static tube dynamic pressure calibration

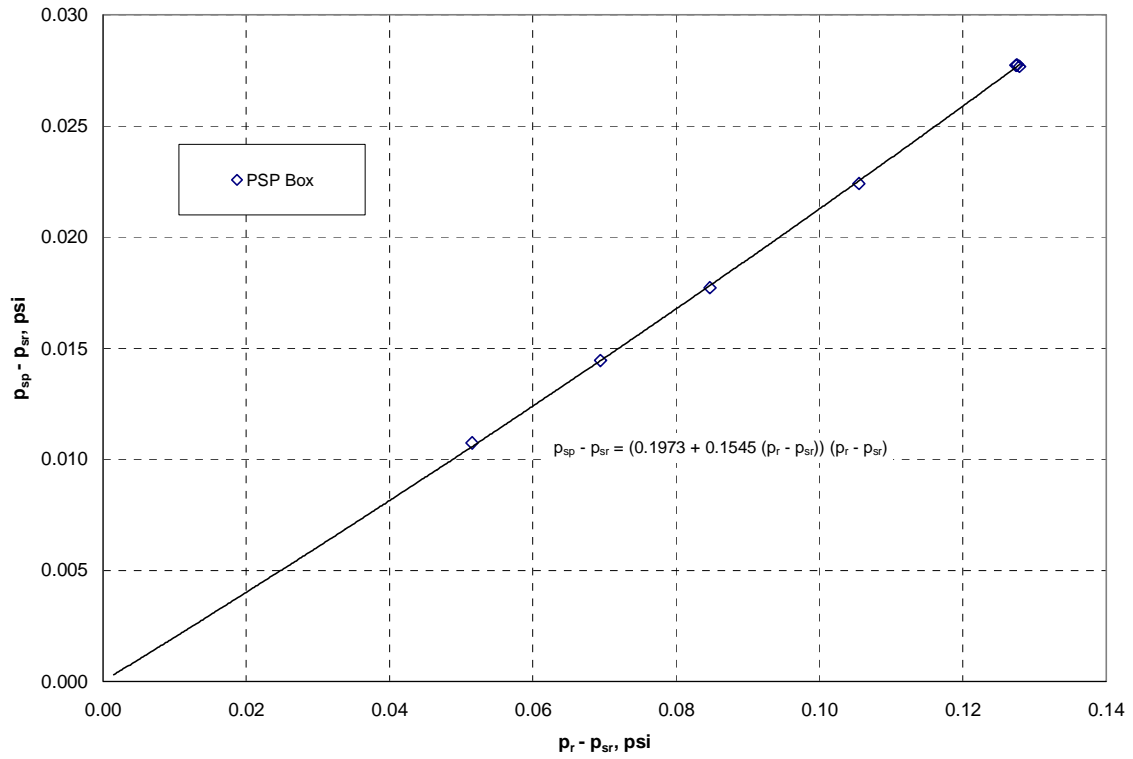


Figure A-3. PSI pitot-static tube static pressure calibration

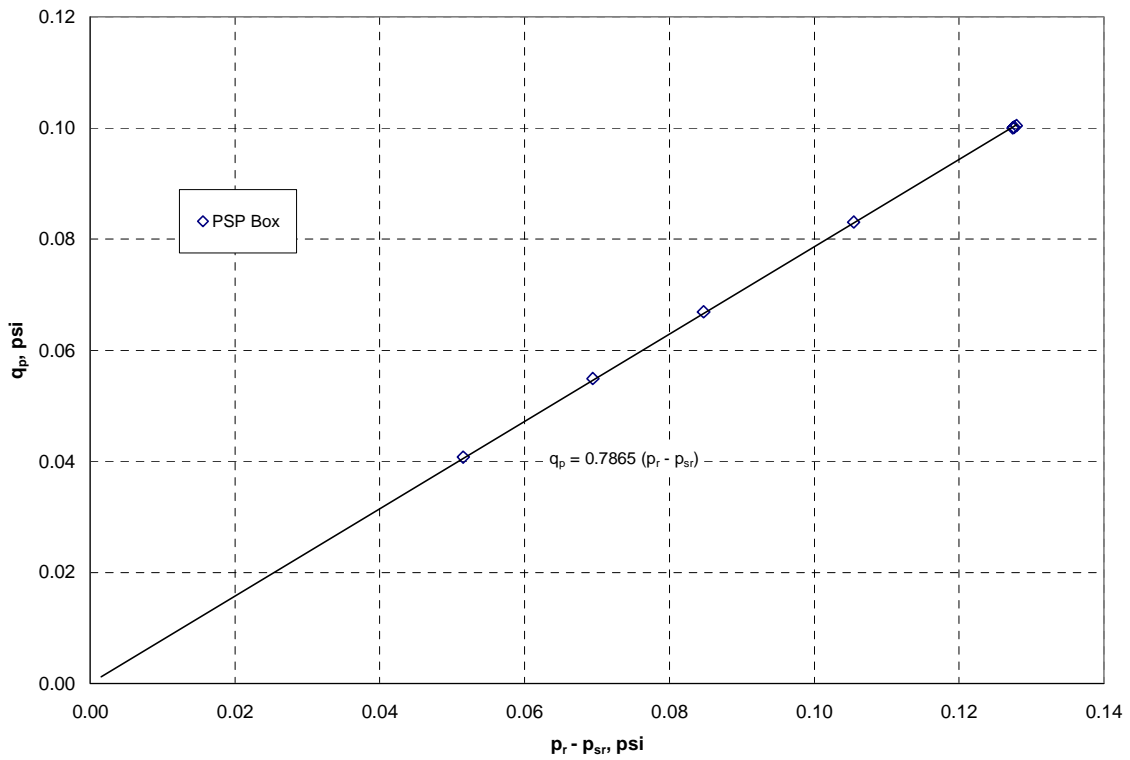


Figure A-4. PSI pitot-static tube dynamic pressure calibration

Table A-1. Test Conditions Calibration Factors

	$k_1$	$k_2$
Endevco transducers	0.2148	0.7970
PSI transducers	0.2148*	0.7865

\*This value of  $k_1$  is for a linear fit of the data, forced through the origin (0,0), and is included only as a comparison to the Endevco calibration. Because the PSI calibration data were slightly nonlinear, a better fit was obtained with the relation,

$$k_1 = 0.1973 + 0.1545 (p_r - p_{sr}).$$

Test data obtained with the PSI system were reduced with this expression.

The calibration of tunnel test conditions, using the Endevco transducers, was run first with only the model and support hardware present in the tunnel. The calibration was repeated with the pressure-sensitive paint (PSP) hardware box on the floor of the tunnel downstream of the model. No significant effects of the PSP box were seen. When the test parameters were calibrated using the PSI transducers, all data were acquired with the PSP box in place.

It is possible to obtain theoretical estimates of  $k_1$  and  $k_2$ . The primary purpose of these derivations is not to replace the calibrations with theoretical results, but to show that the calibrations should be linear as hypothesized. From Bernoulli's relation for incompressible flow, the total pressure,  $p_t$ , which is constant along a streamline, is equal to the sum of the local dynamic pressure,  $q$ , and the static pressure,  $p$ . That is,

$$p_t = q + p. \quad (\text{A-7})$$

Then, at the static ring, "sr",

$$\begin{aligned} q_{sr} &= p_t - p_{sr} \\ &= (p_r - p_{sr}) + (p_t - p_r) \\ &= (p_r - p_{sr}) + q_r \\ &= (p_r - p_{sr}) + q_{sr} \left( \frac{V_r}{V_{sr}} \right)^2 \\ &= \frac{(p_r - p_{sr})}{1 - (V_r/V_{sr})^2}. \end{aligned}$$

Letting

$$k_0 = \left[ 1 - (V_r/V_{sr})^2 \right]^{-1}, \quad (\text{A-8})$$

then

$$q_{sr} = k_0 (p_r - p_{sr}). \quad (\text{A-9})$$

For incompressible flow (density,  $\rho = \text{constant}$ ),

$$V_r A_r = V_{sr} A_{sr}$$

$$V_r / V_{sr} = A_{sr} / A_r$$

where  $A_r$  and  $A_{sr}$  are the cross-sectional areas of the tunnel at the reference and static ring stations, respectively. Substituting this relation into Equation (A-8) gives

$$k_0 = \left[ 1 - (A_{sr}/A_r)^2 \right]^{-1}. \quad (\text{A-10})$$

For the NASA ARC 7 x 10-Foot Tunnel,  $A_r/A_{sr} \approx 14$ . Then,  $k_0 \approx 1.005$ .

To estimate the value of  $k_I$ , again use Bernoulli's relation to relate the pressures at two different locations in the tunnel,

$$q_p + p_{sp} = q_{sr} + p_{sr}.$$

Solving for  $p_{sp} - p_{sr}$ ,

$$p_{sp} - p_{sr} = q_{sr} - q_p$$

$$= q_{sr} \left[ 1 - \frac{q_p}{q_{sr}} \right].$$

Introducing the definition of dynamic pressure,  $q = \rho V^2 / 2$ ,

$$p_{sp} - p_{sr} = q_{sr} \left[ 1 - \left( \frac{V_p}{V_{sr}} \right)^2 \right].$$

Substituting Equation (A-9) for  $q_{sr}$ ,

$$p_{sp} - p_{sr} = k_0 \left[ 1 - \left( \frac{V_p}{V_{sr}} \right)^2 \right] (p_r - p_{sr}). \quad (\text{A-11})$$

The term,  $V_p/V_{sr}$ , is a "model influence" factor which relates the velocity at the probe to the "freestream" velocity at the static ring. This term is difficult to evaluate theoretically since it is influenced by two factors. First, the presence of the model reduces the test section area, resulting in an increased test section velocity<sup>A-1</sup>. Second, there is a local influence of the model on the flowfield which increases the static pressure, thereby reducing the velocity, in the vicinity of the probe. The value of  $V_p/V_{sr}$  is a function of the model geometry, probe location, and tunnel geometry. However, it should be a constant for a given test geometry. Therefore, we define  $k_1$  as

$$k_1 = k_0 \left[ 1 - \left( \frac{V_p}{V_{sr}} \right)^2 \right]. \quad (\text{A-12})$$

Substituting this relation in Equation (A-11) gives,

$$p_{sp} - p_{sr} = k_1 (p_r - p_{sr}). \quad (\text{A-13})$$

Values of  $k_1$  obtained from the two calibrations are given in Table A-1.

Finally, a relation for the dynamic pressure measured by the probe can be developed.

$$\begin{aligned}
q_p &= p_{tp} - p_{sp} = p_t - p_{sp} \\
&= q_{sr} + p_{sr} - p_{sp} \\
&= k_0(p_r - p_{sr}) - k_1(p_r - p_{sr}) \\
&= (k_0 - k_1)(p_r - p_{sr}) \quad .
\end{aligned}$$

Letting

$$k_2 = k_0 - k_1, \tag{A-14}$$

then,

$$q_p = k_2(p_r - p_{sr}). \tag{A-15}$$

For the present test,  $k_2 \approx 1.005 - 0.2148 = 0.7903$ , which agrees closely with the calibration values in Table A-1.

## REFERENCES

- <sup>A-1</sup> J. M. Macha and R. J. Buffington, "Wall-Interference Corrections for Parachutes in a Closed Wind Tunnel," *Journal of Aircraft*, Vol. 27, No. 4, pp. 320-325, April 1990.

## APPENDIX B

### ESTIMATION OF AVERAGING TIME

The purpose of averaging data is to obtain a mean value which has less variance than the data samples. When data samples are independent, that is, uncorrelated, the standard deviation of the mean is related to the standard deviation of the samples by the relation

$$\frac{s_{\bar{x}}}{s_x} = \frac{1}{\sqrt{n}} \quad (\text{B-1})$$

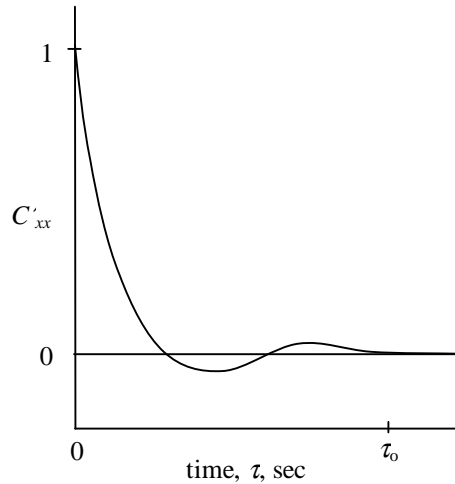
where  $n$  is the number of samples averaged. However, most experimental data are correlated, either through physical processes or data acquisition. In the present test, air turbulence, pneumatic filtering in the pressure system, and electronic filtering in the data acquisition all contribute to data correlation. Estimating the standard deviation of the mean is much more difficult for correlated data than for independent data. The procedure used here is described in Refs. B-1 and B-2. In Ref. B-1, Bendat and Piersol show that, for correlated data,

$$\left( \frac{s_{\bar{x}}}{s_x} \right)^2 = \frac{2}{T} \int_0^{\tau_0} \left( 1 - \frac{\tau}{T} \right) C'_{xx}(\tau) d\tau \quad (\text{B-2})$$

where  $T$  is the total averaging time,  $C'_{xx}$  is the normalized autocorrelation function,  $\tau$  is delay time, and  $\tau_0$  is the time at which  $C'_{xx}$  goes to zero. The autocorrelation function,  $C_{xx}$ , is normalized by dividing each element by the value at  $\tau = 0$ , that is,

$$C'_{xx}(\tau) = C_{xx}(\tau) / C_{xx}(0). \quad (\text{B-3})$$

A typical normalized autocorrelation function for filtered turbulent data is shown in the sketch below, where the parameters discussed above are shown.



Normalized autocorrelation function

If  $\tau_0/T \ll 1$ , then, Equation (B-2) reduces to

$$\left( \frac{s_{\bar{x}}}{s_x} \right)^2 = \frac{2}{T} \int_0^{\tau_0} C'_{xx}(\tau) d\tau \quad , \quad (\text{B-4})$$

which is easier to evaluate. The autocorrelation function,  $C_{xx}$ , was calculated in the Labview data reduction software from the average power spectral density function (see Appendix C) of the pressure coefficients calculated from the measured pressures (the autocorrelation function was not calculated for the reconstructed pressure coefficients). For the present test, data from runs 9 and 14 were selected to represent typical results. This is time-series data acquired with the Endevco transducers and reduced as pressure coefficients. For run 9, pressures were measured on the center ribbon with  $q=11.89$  psf ( $V = 100$  ft/s). Windward and leeward ports are analyzed separately because variance in the data is significantly different for the two sides. In Figure B-1, the autocorrelation function is plotted for the seven windward ports, 16 through 24. Two features are apparent. First,  $C_{xx}$  is very similar for all of the ports, and second, it is highly oscillatory. In Figure B-2, the normalized average of  $C_{xx}$  for the seven ports is plotted. It is still oscillatory with the frequency of oscillation approximately 94 Hz. This oscillatory behavior makes integration more difficult and less accurate, so the data were smoothed with a 9-point simple moving average. The number of points in a moving average is defined by<sup>B-3</sup>

$$n = \frac{1}{f \Delta t} \quad (\text{B-5})$$

where  $f$  is the “notch frequency”, that is, the frequency at which the moving average attenuates the signal to a gain of zero.  $\Delta t$  is the sampling interval of the data. For  $f = 94$  Hz and  $\Delta t = 1/800$  s,  $n = 8.5$ . To avoid phase shifts in the smoothed average, the nearest odd integer is used—in this case, 9.

For the leeward side of the ribbon, the autocorrelation functions for ports 25 through 32 are presented in Figure B-3. The 94 Hz oscillatory component is much smaller for these ports, but the extent of correlation is larger as a result of the wake structure. A normalized average of these ports is presented in Figure B-4 with its 9-point moving average.

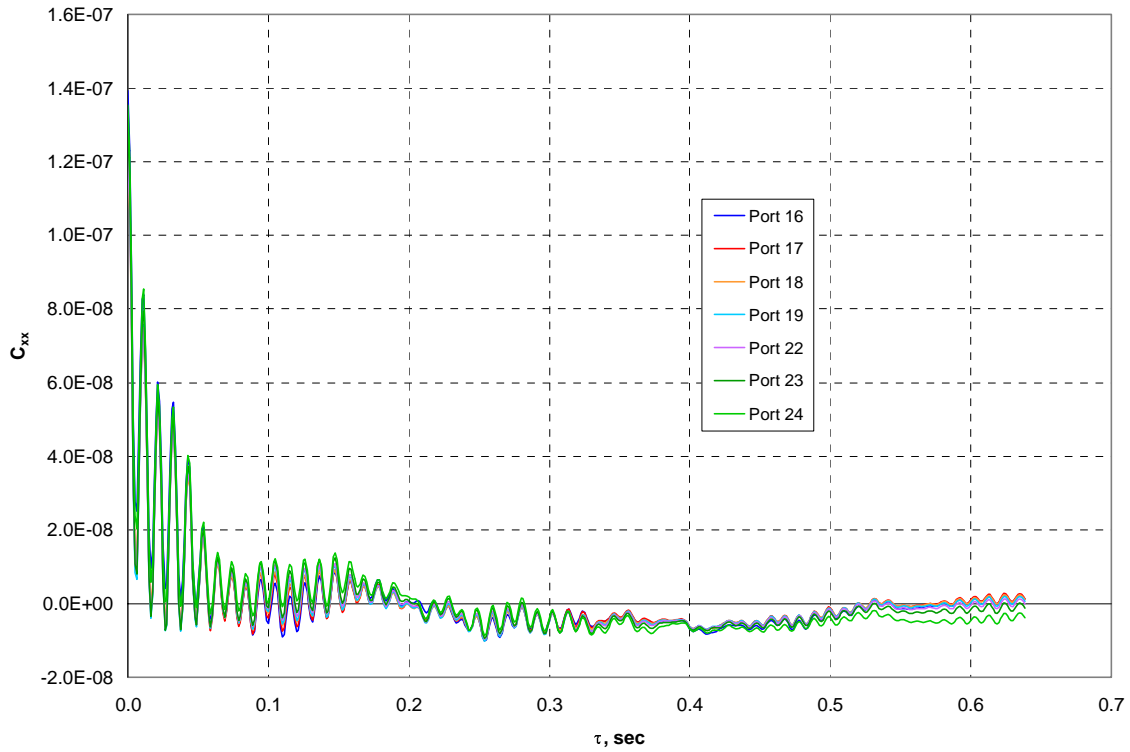


Figure B-1. Autocorrelation function, center ribbon, windward ports, Run 9

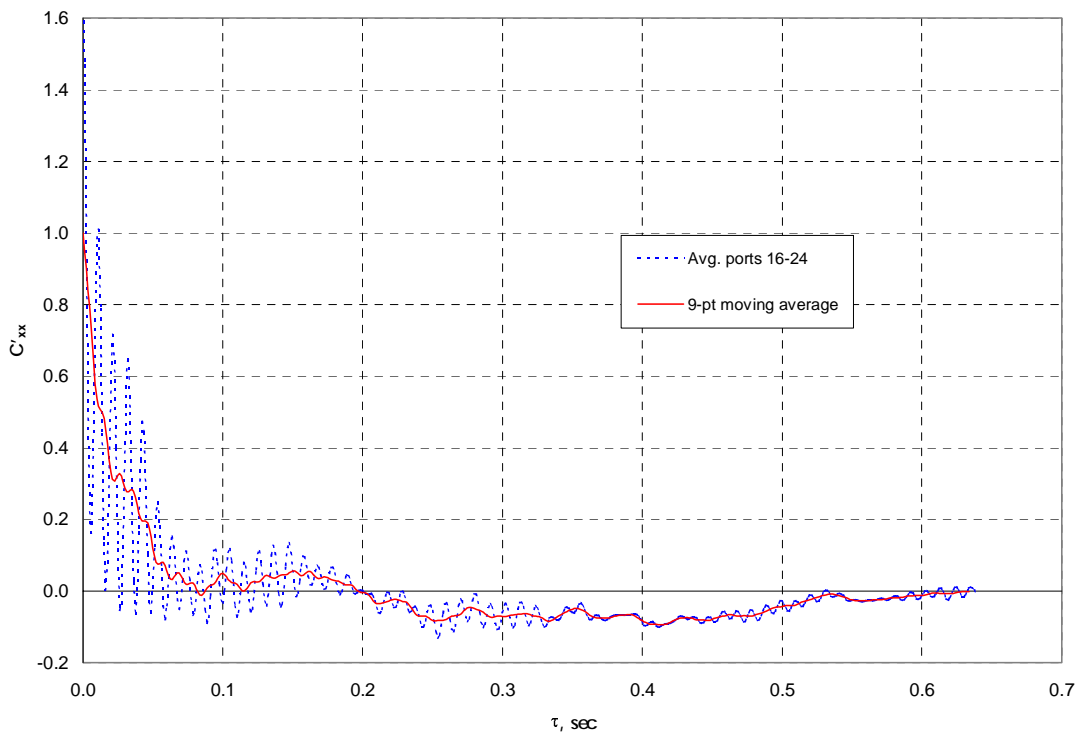


Figure B-2. Average normalized autocorrelation function, center ribbon, windward ports

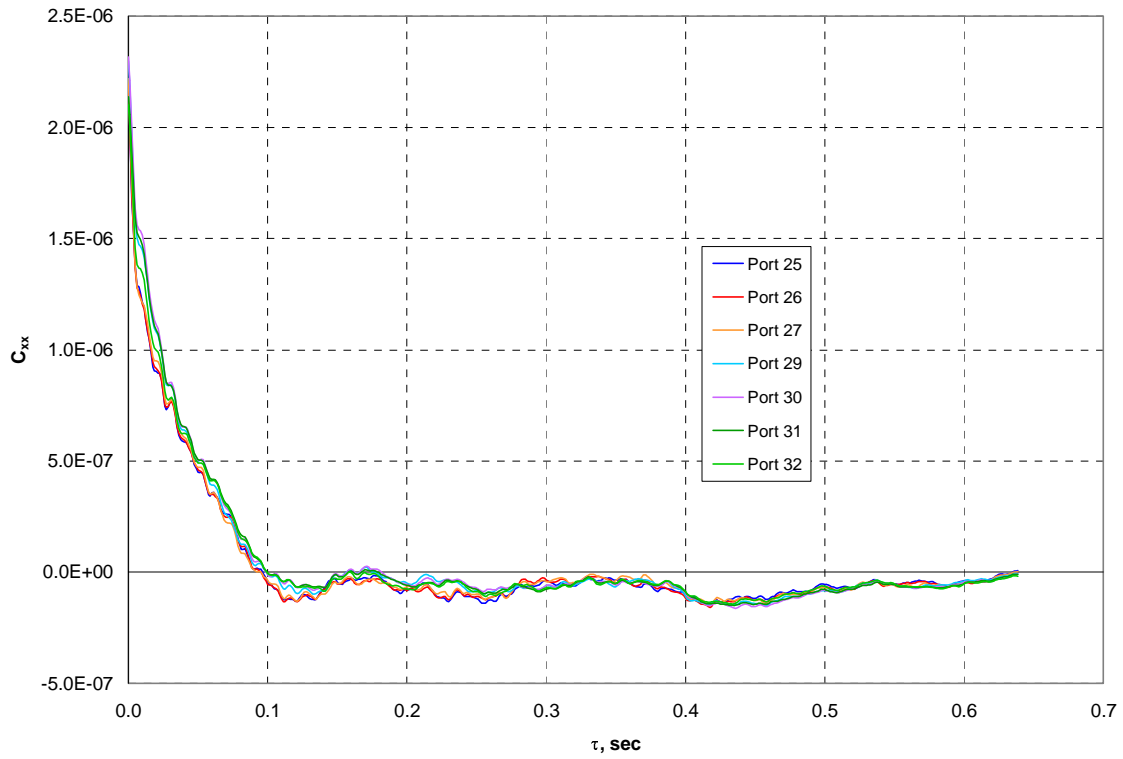


Figure B-3. Autocorrelation function, center ribbon, leeward ports, Run 9

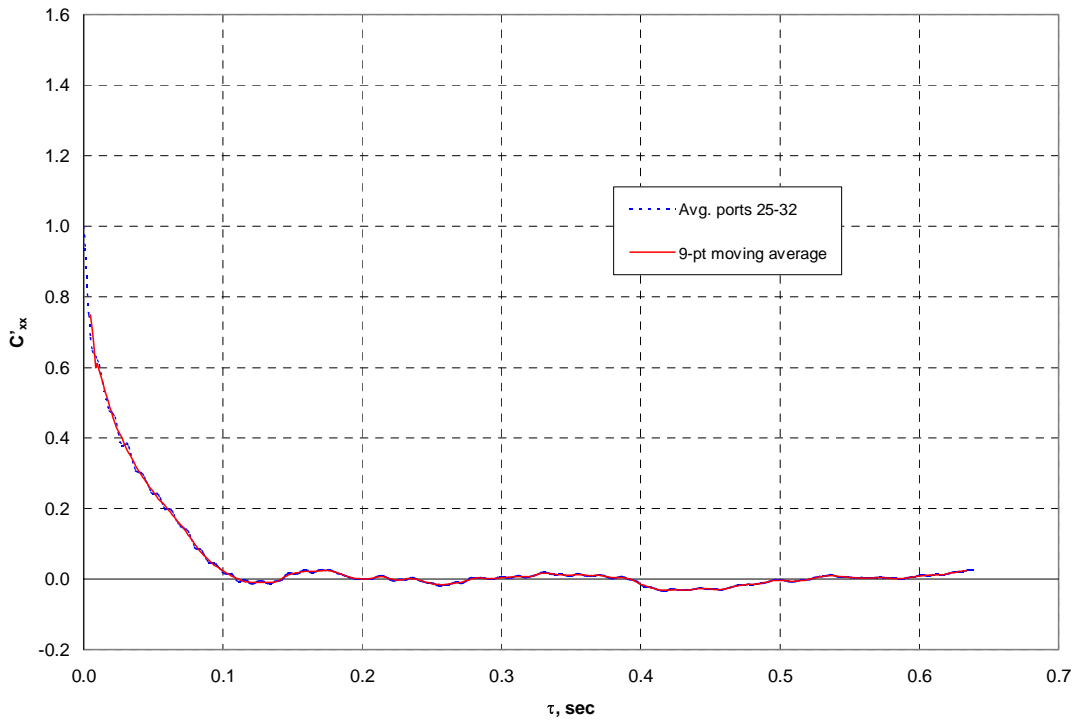


Figure B-4. Average normalized autocorrelation function, center ribbon, leeward ports

The estimated reduction in the standard deviation of mean values,  $s_{\bar{x}}/s_x$ , was calculated with Equations (B-2) and (B-4) for the two sets of data and is presented in Figure B-5. For this data, the approximate integral, Equation (B-4), is adequate. Also shown in Figure B-5 is the reduction in standard deviation for independent samples calculated with Equation (B-1). The significant effect of correlation on variance reduction is obvious. To estimate the effect of dynamic pressure on the data correlation, data from Run 14, with  $q = 7.81$  psf ( $V = 80$  ft/s), were analyzed and the results were essentially the same as those for the higher dynamic pressure. It was assumed that the pressure measuring system contributed significantly to the data correlation. However, examination of data from ports 16 (windward) and 25 (leeward) from run 19 showed that the measured and reconstructed pressures had essentially the same autocorrelation functions. As a further check, autocorrelation functions for the reference and response pressures from one of the proof of principle tests (run 26, random noise input signal) were examined. Although the response pressure showed a slightly increased correlation when compared to the reference pressure, this would have a less than 10% effect on the standard deviation reduction factor. Therefore, the factors calculated for measured pressures can also be applied to reconstructed pressures.

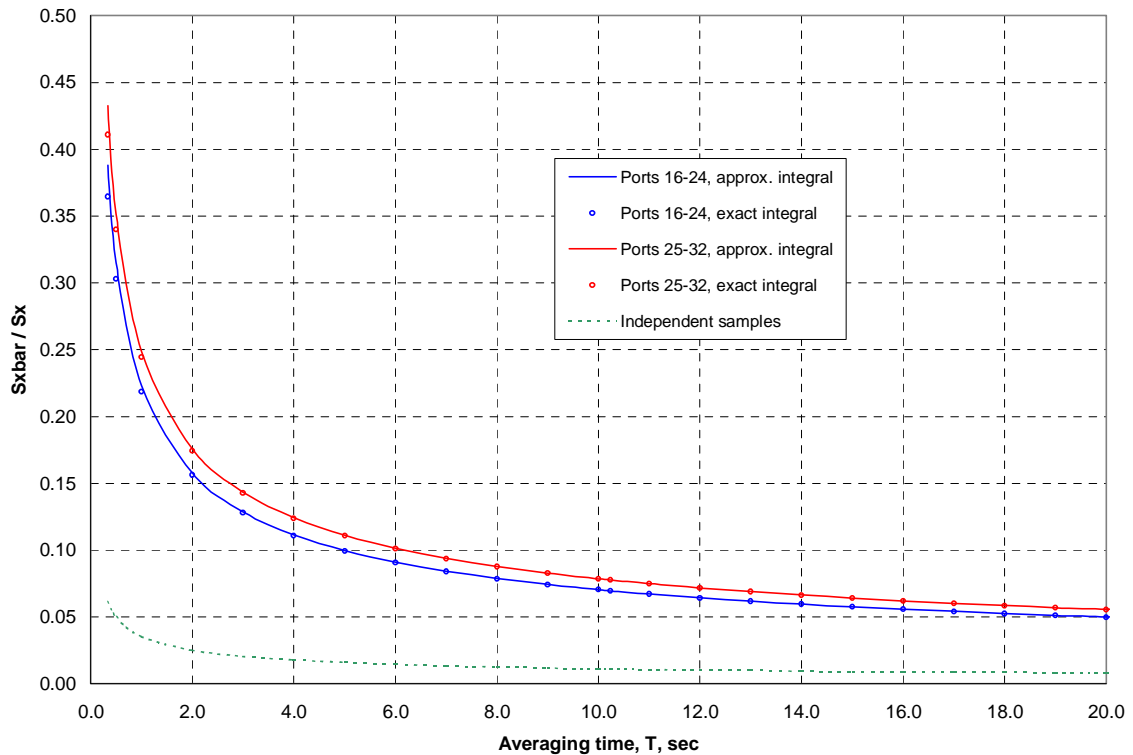


Figure B-5. Standard deviation reduction ratio

The final step in determining an acceptable averaging time is to estimate the relative uncertainty in the mean values. The confidence interval on the mean,  $\mu$ , is given by

$$P \left[ \bar{x} - z_{\alpha/2} s_{\bar{x}} \leq \mu \leq \bar{x} + z_{\alpha/2} s_{\bar{x}} \right] = 1 - \alpha \quad (\text{B-6})$$

where  $z_{\alpha/2}$  is the standardized normal random variable for a confidence level of  $1 - \alpha$ . Typical values of  $z_{\alpha/2}$  are given in the table below:

Table B-1. Standardized Normal Random Variable

probability of uncertainty, $\alpha$	confidence level, $1-\alpha$	$z_{\alpha/2}$
0.10	0.90	1.64
0.05	0.95	1.96
0.01	0.99	2.58

On the average, in  $100(1-\alpha)$  out of 100 samples, an interval calculated from Equation (B-6) will include the true population mean,  $\mu$ . The absolute uncertainty in the mean is determined from the confidence interval to be,

$$\varepsilon_{\bar{x}} = \bar{x} - \mu = z_{\alpha/2} s_{\bar{x}} \quad (\text{B-7})$$

The relative uncertainty is then,

$$RE_{\bar{x}} \equiv \frac{\varepsilon_{\bar{x}}}{\bar{x}} = \frac{s_{\bar{x}} z_{\alpha/2}}{\bar{x}} \quad (\text{B-8})$$

or

$$RE_{\bar{x}} \equiv \frac{\varepsilon_{\bar{x}}}{\bar{x}} = \frac{s_{\bar{x}} z_{\alpha/2}}{s_x} \frac{s_x}{\bar{x}} \quad (\text{B-9})$$

From the data of Runs 9 through 13, the average values of mean and standard deviation for  $C_p$  are listed in Table B-2:

Table B-2.  $C_p$  Statistics, Center Ribbon,  $V = 100$  ft/s

Runs 9 - 13	Ports 16 – 24 (windward)	Ports 25-32 (leeward)
Basic data:		
$\bar{C}_p$	0.9380	-1.428
$s_{C_p}$	0.01169	0.04769
Reconstructed data:		
$\bar{C}_p$	0.9380	-1.428
$s_{C_p}$	0.01522	0.05567

For this test, it was decided to use a confidence level of 0.99. Then, with  $z_{\alpha/2} = 2.58$ , values of the data mean and standard deviation from the above table, and  $s_{\bar{x}}/s_x(T)$  from Figure B-5, the relative uncertainty in  $\bar{x}$  was calculated from Equation (B-9) and is presented in Figure B-6.

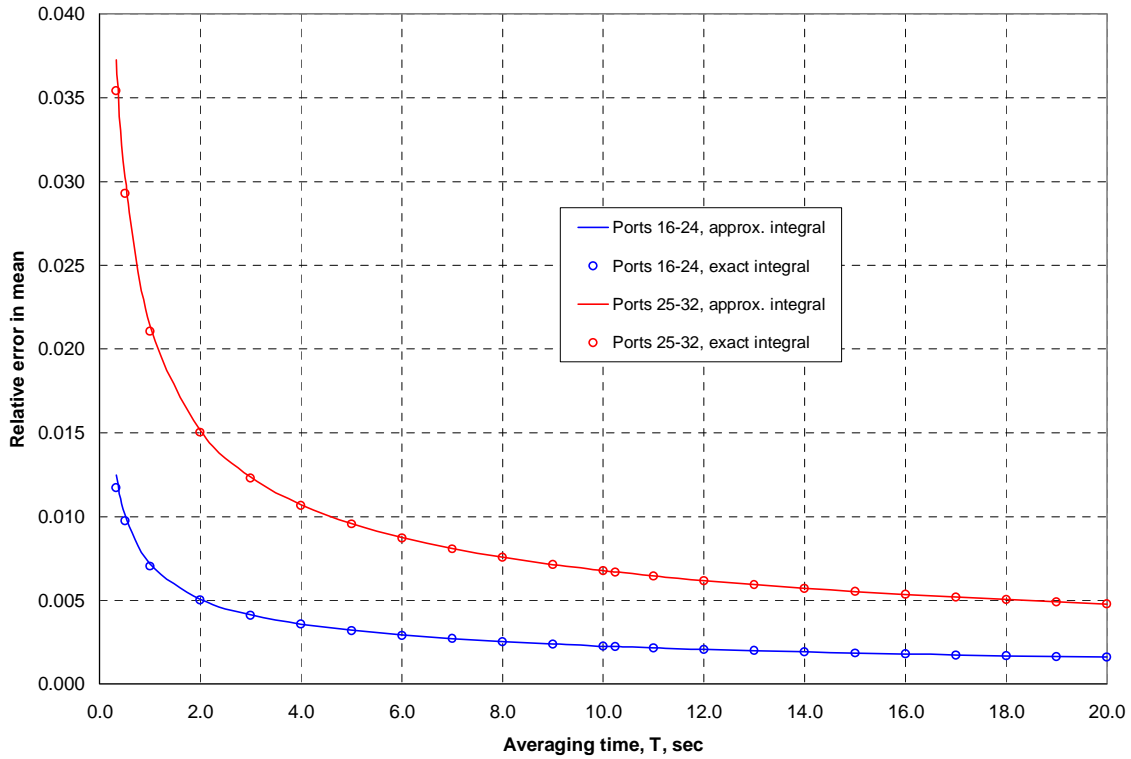


Figure B-6. Relative error in the mean

For the averaging time selected for this test,  $T = 10.24$  s, the relative uncertainty in mean values of  $C_p$  are given in Table B-3:

Table B-3. Relative Uncertainty in  $\bar{C}_p$

	Windward ports	Leeward ports
$s_{\bar{x}}/s_x(T), T = 10.24$ s	0.0695	0.0775
Basic data		
$\varepsilon_{\bar{C}_p}/\bar{C}_p$	0.00223	0.00668
Reconstructed data		
$\varepsilon_{\bar{C}_p}/\bar{C}_p$	0.00291	0.00779

It should be noted that this uncertainty is related to the ability of the average to produce an accurate mean value from noisy data. Although averaging also reduces the measurement precision errors in the data, which are addressed in Appendix F, these errors are small compared to the variance caused by flow dynamics. Three sets of repeat runs, each consisting of five to six runs, were analyzed for the uncertainty in the mean pressure coefficients,  $\bar{C}_p$ . For each set of runs, the mean, standard deviation, and relative uncertainty (0.99 probability) of

the  $\overline{C}_p$  values were calculated. Relative uncertainties in the 17 windward means varied from 0.0007 to 0.0074. For the leeward side, the relative uncertainties in the 20 means varied from 0.0027 to 0.0096. Although these estimates exceed the expected uncertainties given above, they may have been exaggerated by using the standard deviations of only five or six values.

An obvious question is, how did we know the number of samples to average a priori. Sample data must be available for the analysis described above. Prior to the test, the time series (Endevco) data sampling rate was selected as 800 samples/s with a total of 8192 samples. Thus the pre-test estimate of total acquisition time was  $8192/800 = 10.24$  seconds. Our goal was to obtain  $C_p$  with a relative uncertainty of 0.01 or less. Immediately following the first test run (Run 1, ribbon configuration 213 and dynamic pressure = 11.89 psf), an analysis similar to that described above was performed. This analysis indicated that an acquisition and averaging time of 10.24 seconds would be adequate for the desired  $C_p$  accuracy.

For the PSI pressure data, the analysis is slightly different. Two hundred sets of data were acquired with a delay of 1.0 s between each set. Each set consisted of 127 samples averaged over approximately 0.33 s. From Figure B-5,  $s_{\bar{x}}/s_x = 0.3646$  and  $0.4110$  for the windward and leeward sides, respectively, at  $T = 0.33$  s. The autocorrelation curves in Figures B-1 and B-3 indicate that the data correlation after one second is negligible. Therefore, Equation (B-1) can be used to estimate the additional reduction in standard deviation of the mean at  $T = 200$  seconds ( $n = 200$ ). Multiplying the  $T = 0.33$  s values of  $s_{\bar{x}}/s_x$  by  $1/\sqrt{200}$  gives  $s_{\bar{x}}/s_x = 0.0258$  and  $0.0291$ . Applying Equation (B-9) with a confidence level of 0.99 gives a relative uncertainty in the mean of approximately 0.00083 and 0.00251 for the windward and leeward sides, respectively. Thus, the averaged PSI data should have a standard deviation of about 40% of that for the averaged Endevco data.

Finally, it is necessary to evaluate the effects of averaging on the tunnel reference differential pressure,  $p_r - p_{sr}$ . The autocorrelation function is shown in Figure B-7 and the normalized autocorrelation function is shown in Figure B-8. This pressure is correlated over a much longer time (0.65 s compared to approximately 0.2 s for the model pressures), almost certainly the result of the large manifolds associated with the two reference pressures. For this differential pressure,  $s_{\bar{x}}/s_x = 0.6618$  for  $T = 0.33$  s and  $0.0480$  for  $T = 10.24$  s.

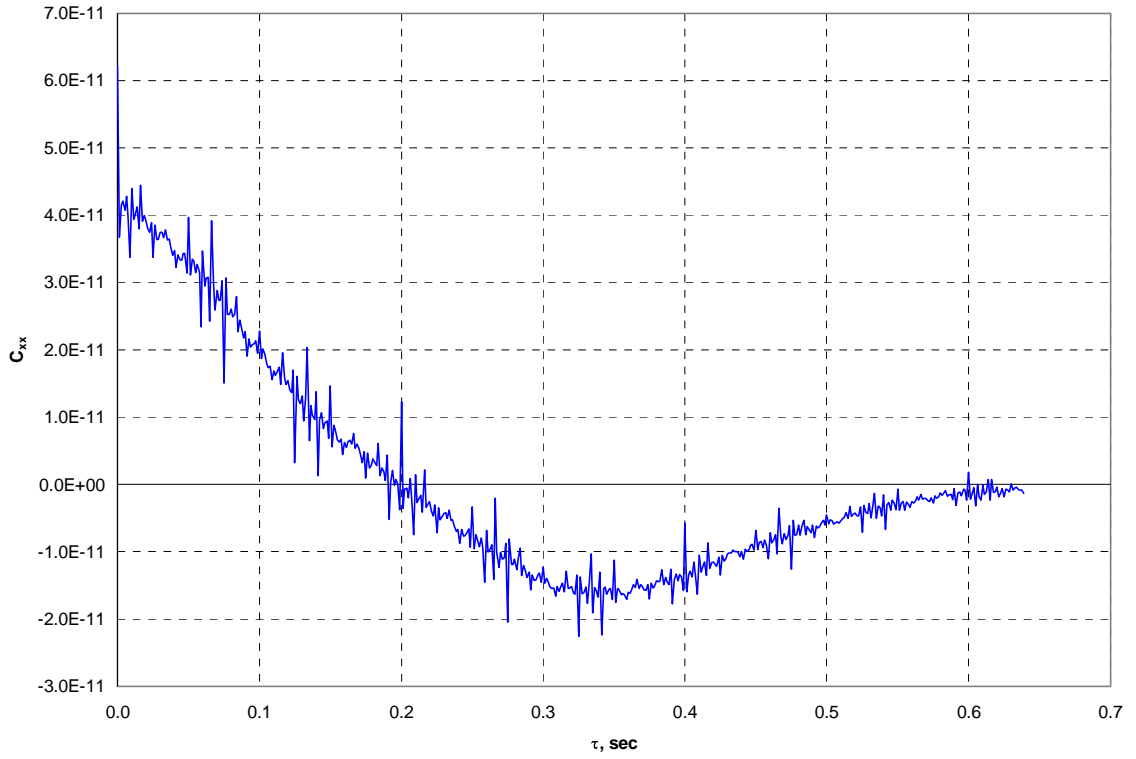


Figure B-7. Autocorrelation function for  $p_r - p_{sr}$ , Run 9

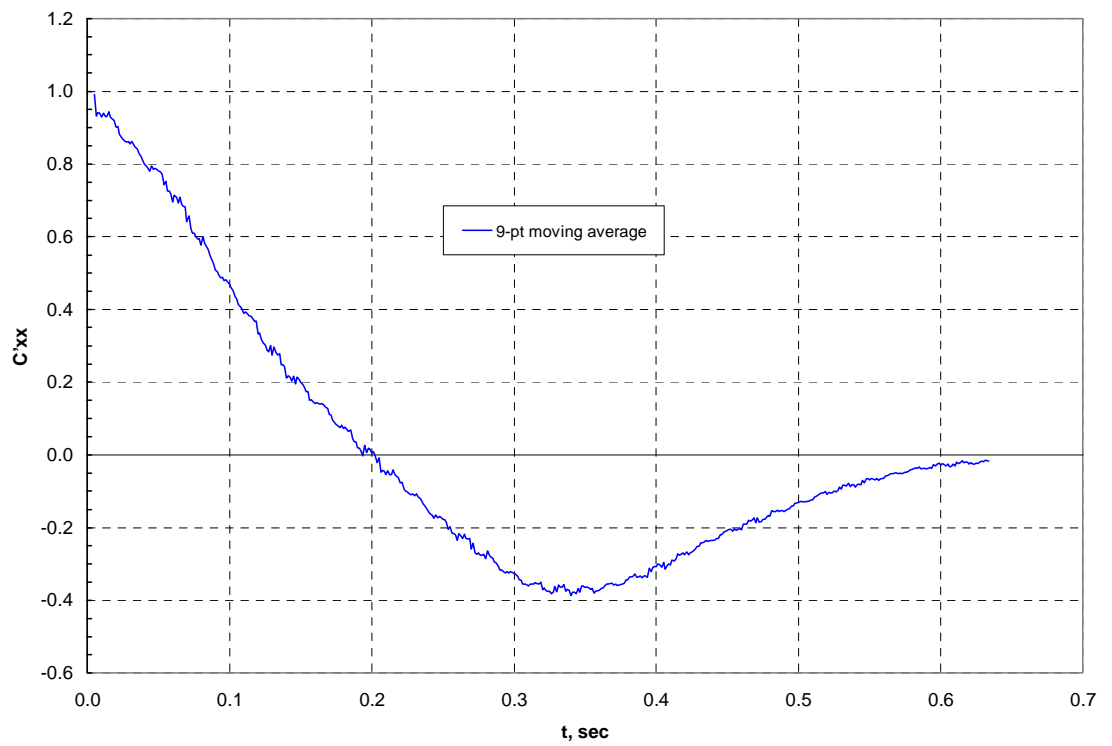


Figure B-8. Normalized autocorrelation function for  $p_r - p_{sr}$

A summary of the standard deviation reduction ratios,  $s_{\bar{x}}/s_x$ , is given below. As was mentioned above, for the Endevco data, these factors apply to both the measured and reconstructed pressures.

Table B-4. Standard Deviation Reduction Ratios

	Endevco	PSI	
	$T = 10.24 \text{ s}^*$	$0.33 \text{ s}^*$	$200 \text{ s}^{**}$
$\Delta p_i$ , windward ports	$s_{\bar{x}}/s_x = 0.0695$	0.3646	0.0258
$\Delta p_i$ , leeward ports	0.0775	0.4110	0.0291
$p_r - p_{sr}$	0.0480	0.6618	0.0468

\* Correlated samples

\*\* Uncorrelated samples

### REFERENCES

- B-1 J. S. Bendat and A. G. Piersol, *Random Data—Analysis and Measurement Procedures*, 2<sup>nd</sup> ed., Section 8.2, John Wiley & Sons, New York, 1986.
- B-2 E. L. Clark, “Arithmetic Averaging—Effects of Data Correlation on Variance Reduction”, Paper No. 95-3004, *ISA 41<sup>st</sup> International Instrumentation Symposium*, Denver, CO, May 1995.
- B-3 E. L. Clark, “Arithmetic Averaging—A Versatile Technique for Smoothing and Trend Removal”, Paper No. 94-2004, *ISA 40<sup>th</sup> International Instrumentation Symposium*, Baltimore, MD, May 1994.

## APPENDIX C

### CALCULATION OF THE POWER SPECTRAL DENSITY FUNCTION

The power spectral density (PSD) function,  $S_{xx}(f)$ , also referred to as the autospectral function, estimates the distribution of power with frequency for a time series. Thorough discussions of this function can be found in digital signal analysis textbooks (for example, see Stearns and Hush<sup>C-1</sup>.) It was calculated in the present test for two reasons. First, it clearly defines significant frequency components present in the data. This is important because it is nearly impossible to visually identify frequency components in a signal which contains a significant random component. Second, the PSD was required to calculate the autocorrelation function, which was needed for estimating averaging time, see Appendix B. The method used in our data reduction is frequently called a modified periodogram and is attributed to Welch<sup>C-2</sup>.

It was anticipated that the only significant periodic component in the measured pressures would have a frequency equal to the vortex shedding frequency. This frequency was expected to be less than 100 Hz. To be conservative, we selected a frequency analysis range of 0 - 400 Hz. This defined the sampling frequency as 800 samples/s. During preliminary studies of the pressure measurement system transfer function, it was found that signal amplitudes at frequencies greater than 400 Hz were attenuated at the transducer to less than 25% of their initial amplitude. Therefore, any frequency components present in the data, with  $f > 400$  Hz, which might be aliased into the frequencies of interest, would be significantly attenuated. The signal conditioning incorporated a 600-Hz, 4-pole, Butterworth low pass filter. This further reduced the effects of data aliasing, but had no significant effect on frequencies less than 400 Hz. To provide accurate estimates of the mean pressure coefficients, it is necessary to calculate the average value from data acquired over several seconds. From experience with similar data, we decided that a 10-second average should be sufficient. For the PSD calculations, it was desirable to have the number of samples be an integer power of 2. Therefore, the number of samples to be acquired was selected as 8192 which gives a 10.24-second averaging period. Results from one of the first test runs verified that the averaging time was adequate (see Appendix B).

The basic procedure for the modified periodogram is to break the data set into smaller subsets, which may be overlapping; multiply each subset by a window function; calculate the PSD elements,  $S_{xx}(f)$ , of each subset; then average all of the PSDs. Merely calculating the PSD of the entire data set results in a statistically inconsistent spectrum (one whose variance is not limited as the number of samples is increased) which has unacceptable variance. The first step in the process was to divide the data set (8192 samples) into  $M$  smaller subsets or segments of length,  $L$ . The subset size was selected as  $L = 1024$  samples which would give  $M = 8$  subsets (the subset length,  $L$ , must be a power of 2 for FFT analysis). For simplicity in analysis, it was decided to not overlap the subsets. This results in increased uncertainty in the results. For each subset, the mean was calculated and subtracted from the data. The purpose of this operation is to reduce the DC ( $f = 0$  Hz) component of the PSD. Otherwise, the DC component may be so large that other components are obscured. Next, the subset was windowed with a Hanning window. That is, each sample was multiplied by a corresponding weight,  $w_i$ , which is given by,

$$w_i = 0.5 [1 - \cos(2i\pi/L)], i = 0, L-1 \quad (C-1)$$

The shape of the window weights is shown in Figure C-1 below. The purpose of windowing the data is to reduce “leakage,” that is, to reduce spurious side lobes which appear adjacent to a main lobe when windowing is not used. There are two undesirable effects of the window. First, it broadens the main lobe, this was not felt to be significant for the present data. Second, the mean of the data set is no longer zero. The mean could be removed again, but this would force the windowed data to be offset from zero at the endpoints. We ignored this effect.

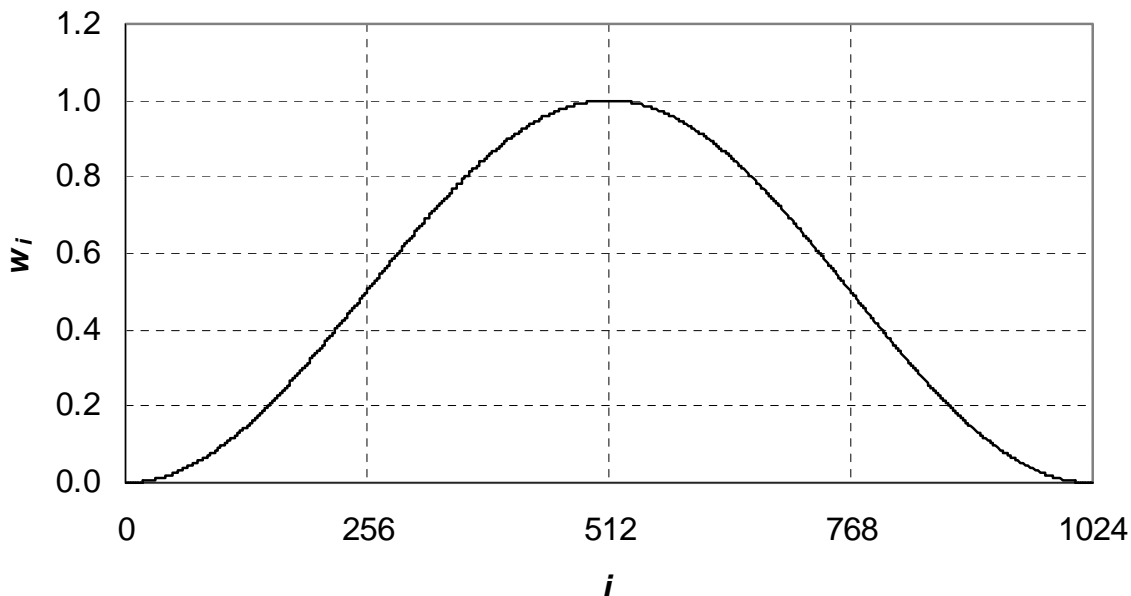


Figure C-1. Hanning weights

The next step is to calculate the Fourier transform of the subset, using an FFT. The squared magnitude of the coefficient is calculated at each frequency value by summing the squares of the real and imaginary parts of the transform. The time span of each segment is  $1024/800 = 1.28$  seconds. Then, the frequency interval of the PSD is  $\Delta f = 1/1.28 = 0.78125$  Hz. The squared magnitudes of the PSD at each frequency value are summed for the 8 segments. Finally, the summed PSD values are normalized by multiplying by the factor,

$$u = \frac{T}{\left( M \sum_0^{L-1} w_i^2 \right)} \quad (C-2)$$

where  $T$  is the sampling interval,  $T = 1/800 = 0.00125$  second. The sum of the weights squared,  $\sum w_i^2$  is equal to  $3/4 * (L/2) = 384$ . Then  $u = 4.069 \times 10^{-7}$ . The purpose of this normalization is to scale the PSD values so that the integral of  $S_{xx}(f)$  will equal the variance of the data set as it should. That is,

$$V(x) = \int S_{xx}(f) df . \quad (C-3)$$

As a check on the scaling, the integral of the PSD was estimated, using the trapezoidal method, and compared to the actual calculated variance of the data set. The agreement was good.

Bendat and Piersol<sup>C-3</sup> show that  $S_{xx}(f)$  has a chi-squared distribution and an estimate of its confidence interval is given by

$$\mathbf{P} \left[ LCL \times \hat{S}_{xx}(f) \leq S_{xx}(f) \leq UCL \times \hat{S}_{xx}(f) \right] = 1 - \alpha \quad (\text{C-4})$$

where the lower confidence limit,  $LCL = n / \chi_{n, \alpha/2}^2$ , and the upper confidence limit,  $UCL = n / \chi_{n, 1-\alpha/2}^2$ ; the degrees of freedom,  $n = 2M$ ;  $\hat{S}_{xx}(f)$  is the estimated PSD; and  $S_{xx}(f)$  is the actual PSD (infinite number of samples). Two values of probability often used for spectral analyses are 80% and 90%, that is,  $\alpha = 0.2$  and  $0.1$ , respectively. The lower and upper confidence limits,  $LCL$  and  $UCL$ , are given in Table C-1:

Table C-1. Confidence Limits on  $S_{xx}$

$\alpha$	Probability, $\mathbf{P}$	No. of segments, $M$	$LCL$	$UCL$
0.2	80%	1	0.434	9.49
		8	0.680	1.72
0.1	90%	1	0.334	19.5
		8	0.608	2.01

Expressing Equation (C-4) in words: For  $\alpha = 0.1$  and 8 segments, it is expected that for 90% of the calculated values of  $\hat{S}_{xx}(f)$  the actual value of  $S_{xx}(f)$  will fall between  $0.608 \hat{S}_{xx}(f)$  and  $2.01 \hat{S}_{xx}(f)$ . Note the significant improvement in confidence interval limits resulting from averaging eight segments. The  $LCL$  is reduced by a factor of almost two, and the  $UCL$  by a factor of almost ten. Although some authors imply that windowing the data will further reduce the uncertainty, Smallwood<sup>C-4</sup> states that “for non-overlapped windowed data the statistical degrees of freedom,  $n$ , for a PSD estimate is very close to 2 for each segment of data, independent of the window used.”

The final step in this section of the data reduction is to calculate the autocorrelation function,  $C_{xx}(\tau)$ . This is accomplished by calculating the inverse Fourier transform of the  $S_{xx}(f)$  array and multiplying the resulting magnitude by  $\Delta f$ .

## REFERENCES

- C-1 S. D. Stearns and D. R. Hush, *Digital Signal Analysis*, 2<sup>nd</sup> ed., Prentice Hall, Englewood Cliffs, New Jersey, 1990.
- C-2 P. D. Welch, "The Use of Fast Fourier Transform for the Estimation of Power Spectra: A Method Based on Time Averaging Over Short, Modified Periodograms," *IEEE Transactions on Audio and Electroacoustics*, Vol. AU-15, No. 2, June 1967.
- C-3 J. S. Bendat and A. G. Piersol, *Random Data – Analysis and Measurement Procedures*, 2<sup>nd</sup> ed., Section 8.5, John Wiley & Sons, New York, 1986.
- C-4 D. O. Smallwood, "Note on the Variance of Autospectral Density Processed Using Welch's Method," *Proceedings of the IES*, Vol. 2, pp. 273-280, April 1994.

## APPENDIX D

### TIME-ACCURATE PRESSURE RECONSTRUCTION

Measurement of unsteady pressures is best accomplished with in situ, high-frequency response, flush-diaphragm pressure transducers. However, in this experiment the pressures were being measured across thin, stainless steel, simulated ribbons that had no space for in-situ transducers. As a result, it was necessary to locate the transducers at some distance from the pressure tap. This results in the pressure measurement system—orifice, tubing, and transducer cavity—creating a pneumatic filter which alters the amplitude and phase of pressures measured as time series. The time-accurate pressure signature at the orifice can be reconstructed using a method first outlined by Irwin, Cooper, and Girard<sup>D-1</sup> and used most recently by Sims-Williams and Dominy<sup>D-2</sup>. Sims-Williams and Dominy describe a method in which an experimentally obtained transfer function was used to correct signal distortion caused by pressure tubing.

#### **Pressure Reconstruction Using a Transfer Function**

Consider a linear, time-invariant system (that is, one where the system characteristics do not change with time — our pressure system is an example). Let a time-varying pressure at the orifice,  $x(t)$ , be input to the system. Then, the output of the system, the pressure at the transducer,  $y(t)$ , will be related to the input by the transfer function. Let  $X(f)$  and  $Y(f)$  be the Fourier transforms of  $x(t)$  and  $y(t)$ , respectively. Then,

$$Y(f) = X(f) H(f) \quad (\text{D-1})$$

where the transfer function,  $H(f)$ , is given by

$$H(f) = Y(f)/X(f) . \quad (\text{D-2})$$

$H(f)$  was obtained experimentally in the lab prior to tunnel entry. Considerable effort was directed towards duplicating the pressure measurement system on all channels in the wind tunnel and assuring that it in turn duplicated the lab experimental arrangement. Thus we are confident that the transfer function measured in the lab was representative of all channels during the test. Since

$$X(f) = Y(f)/H(f) , \quad (\text{D-3})$$

and

$$x(t) = \mathfrak{S}^{-1}[X(f)], \quad (\text{D-4})$$

$x(t)$  can be obtained by dividing the Fourier transform of the measured pressure by the transfer function and then taking the inverse transform of the result. Labview was programmed to accomplish this during the data reduction.

#### **Experimental Determination of Transfer Function**

There are two components of the transfer function. First, there is amplitude gain, which is the ratio of output signal amplitude to input signal amplitude. Second is the phase shift of the output relative to the input, always a lag for our system.

Writing  $H(f)$  in its complex form,

$$H(f) = R(f) + jI(f) . \quad (\text{D-4})$$

Then the amplitude response, or gain, is

$$|H(f)| = [R^2(f) + I^2(f)]^{1/2} \quad (D-5)$$

and the phase shift is,

$$\phi(f) = \tan^{-1} \left[ \frac{I(f)}{R(f)} \right]. \quad (D-6)$$

The purpose of our measurements was to determine the gain and phase shift as functions of frequency.

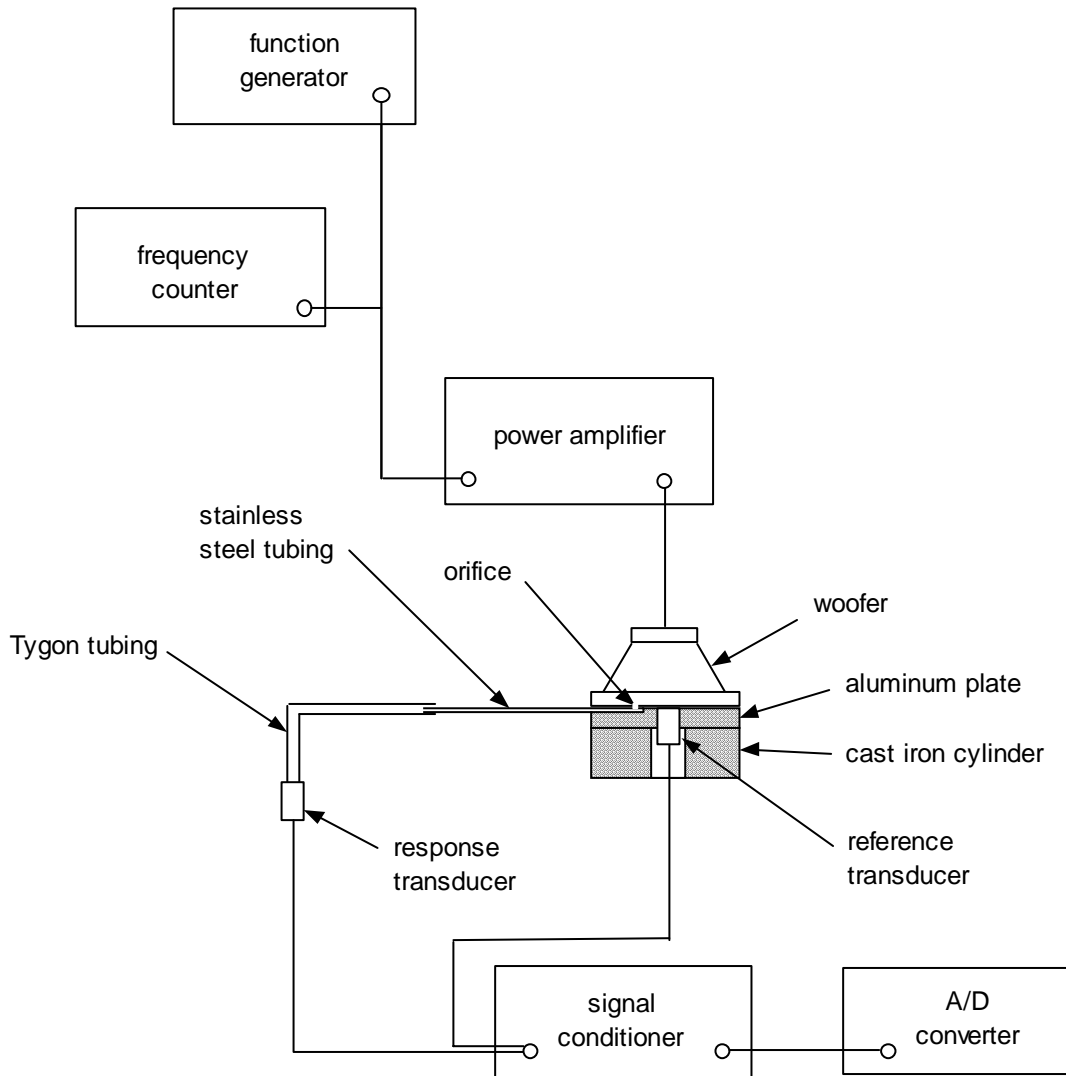


Figure D-1. Schematic of setup for transfer function determination

A schematic of the test setup is shown in Figure D-1. The test fixture was a 0.44-inch thick aluminum plate, 8 inches in diameter. The reference transducer (Endevco Model 8510B-1) was threaded into the center of the plate so its diaphragm was flush with the top surface of the plate. A 20-inch long, 0.03-inch i.d. stainless steel tube was epoxied into a slot in the top surface of the plate. A 0.02-inch diameter orifice, matching those used in the model, was located 0.06 inch

from the closed end of the tube and 0.3 inches from the reference transducer diaphragm. Tygon tubing, 11.5 inches long and 0.03-inch i.d., attached the stainless tubing to the same transducer block which would be used in the wind tunnel test. The response transducer (another Endevco Model 8510B-1) was threaded into the block. The tubing geometry between the orifice and the response transducer was identical to that used in the wind tunnel. The vent tubes on both transducers were open to atmosphere. During the tunnel tests, the vent side was attached with Tygon tubing to a manifold. Therefore, the test setup did not exactly match the tunnel setup. However, it was felt that this was not a significant factor. As a check of this assumption, several transfer function measurements were made with 10 feet of 0.02-inch i.d. Tygon tubing attached to the response transducer vent tube. No effect of the tubing was seen for either gain or phase shift. Early in the measurements, a resonant frequency was detected at about 240 Hz with both the reference and response transducers. It was felt that the aluminum plate could be “oil canning” at that frequency, so it was stiffened by bolting it to a 20-lb cast iron calibration weight. This did not affect the resonance, so we concluded that it was probably the resonant frequency of the speaker cavity. The resonance did not significantly affect the transfer function measurements.

The system was excited with an 8-inch, high quality, woofer having a frequency response of 30 – 700 Hz. “High quality” is emphasized because early efforts with an inexpensive speaker gave poor results because of speaker distortion at the sound levels used to match pressures expected in the tunnel test. The speaker was driven by a Wavetek<sup>®</sup> Model 185 Function Generator. Continuous, fixed-frequency sine waves were used in the measurements. An HP<sup>®</sup> Model 5334B Counter was used to accurately determine the signal frequency. Finally, a Denon<sup>®</sup> Model POA-2400 audio power amplifier was used to drive the speaker. Frequency response of the amplifier is 1 Hz to 300 kHz, +0, -3 dB at 1 watt. Power input was adjusted so that the reference pressure was constant at all frequencies, at 0.012 or 0.095 psi rms for most measurements. Transducer signal conditioning and A/D conversion hardware were the same that would be used in the tunnel test.

Initially, several attempts to determine the transfer function were made using white noise and swept sine waves as the input signals. This approach would greatly reduce the effort required to measure the transfer function, since only a single run would be required to obtain data at all frequencies. However, the results were noisy and were unusable for frequencies greater than 300 Hz. We then tried averaging the results from multiple runs. This reduced the noise in the transfer function, but the results were still far from acceptable. Therefore, we decided to use single-frequency sine waves for the measurements. The frequency range was 0.5 through 400 Hz and 50 cycles of data were acquired for each measurement. The pressure system is linear. That is, only the amplitude and phase of the signal are changed, the frequency is not influenced by the filter. This is a very important factor for data reduction. Data reduction was accomplished with a code which calculated least squares fits with the model,

$y = B + A \sin(2\pi f t + \phi)$ , for the two signals. Frequency of the signals ( $f_{output} = f_{input}$ ), as measured by the frequency counter, was input to the code, and amplitude,  $A$ , and phase,  $\phi$ , of the input and output signals were calculated. Gain and phase shift are then given by

$$gain = \frac{A_{output}}{A_{input}}, \quad (D-7)$$

and

$$phase\ shift = \phi_{output} - \phi_{input}. \quad (D-8)$$

The calculated phase shift was corrected for the inter-channel delay in the A/D converter, 20  $\mu$ s. This delay is twice that described in the *Instrumentation, ...* section because the measurement channels were separated by a common channel to increase settling time. This approach was very accurate, even for low-level response signals.

An interesting phenomenon was noticed during the measurements. The gain and phase shift were dependent on the pressure level at the reference transducer. Over much of the frequency range, the gain decreased by 0.02 to 0.04 and the phase shift varied by  $-0.07$  to 1.6 degree as the reference pressure amplitude was increased from 0.017 psid to 0.134 psid. The variations were linear with pressure over this pressure range. The cause of the pressure dependency is unknown, but it is suspected that it may be the result of gas compressibility or Tygon tube elasticity. Since it was expected that test pressure fluctuations would be less than  $\pm 0.02$  psid,

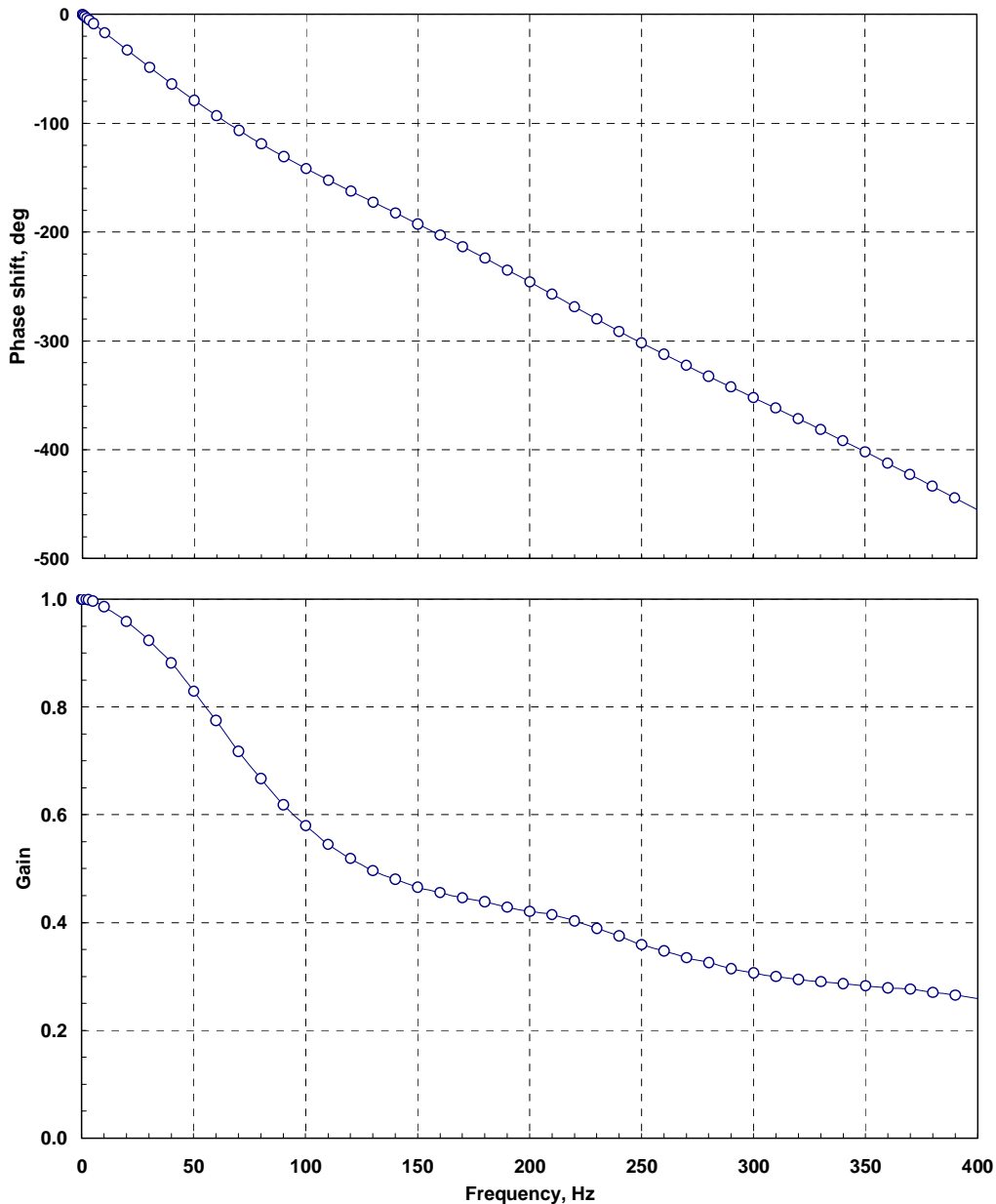


Figure D-2. Experimentally determined transfer function.

the transfer function determined with the lower pressure was used in the pressure reconstruction. The phase shift and gain measurements are presented in Figure D-2.

### **Proof of Principle Test**

It was essential that we verify the reconstruction method prior to conducting the tunnel tests. This verification was accomplished through a series of “proof of principal” tests. The test setup was similar to that described above for measurement of the transfer function, with two significant additions (see Figure D-3).

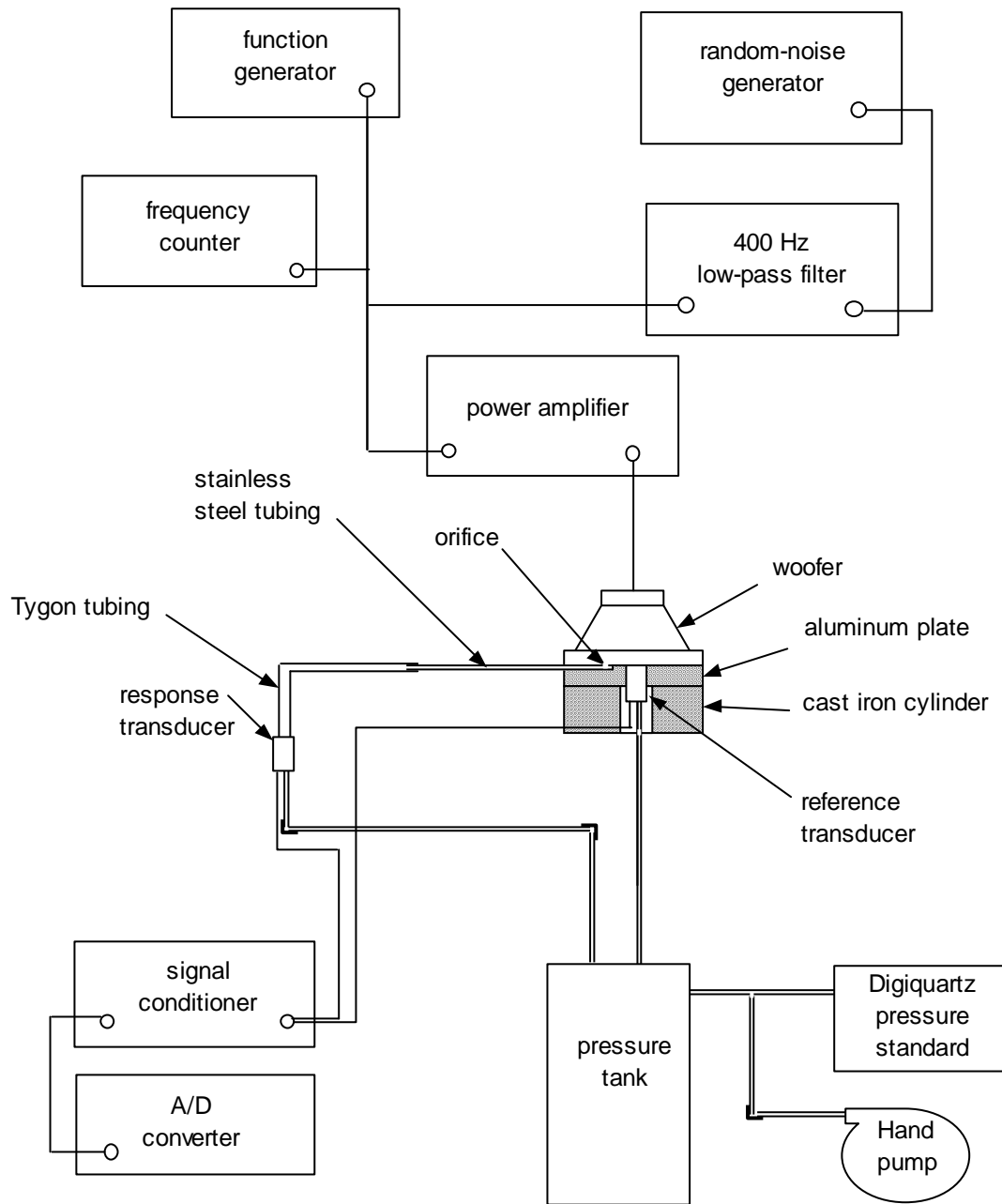


Figure D-3. Schematic of experimental setup for proof of principle test

First, the output of a random noise generator was added to the function generator output (sine wave) to create a complex waveform which would closely simulate the actual pressure waveform anticipated in tunnel testing. The sine wave had a frequency of 80 Hz with a magnitude of 0.5 v rms ( $\approx 0.012$  psi rms). The random component was generated with a GenRad<sup>®</sup> Model 1381 random-noise generator. The generated signal had a 5kHz bandwidth with  $3\sigma$  clipping and a magnitude of 0.5 v rms. This signal was filtered to eliminate high frequencies by using a Krohn-Hite<sup>®</sup> Model 3342 maximally-flat low-pass filter with a cutoff frequency of 400 Hz. The sine wave and random-noise signals were combined and input to the power amplifier. The resultant combined signal had a magnitude of  $\sim 0.016$  psi rms. Second, to complete the simulation, it was necessary to provide a bias pressure. This could not be accomplished electronically because the power amplifier could not pass a DC voltage and the speaker cone was porous and could not maintain a bias pressure resulting from a DC input voltage. Therefore, the vent tubes on the two transducers were connected to a sealed tank which could be pressurized to create a positive or negative bias. Three runs were made with bias pressures of  $-0.08$ ,  $0.0$ , and  $+0.08$  psig.

Results of the test run with a positive bias of 0.08 psig are presented in Figures D-4 through D-7. In Figures D-4 and D-5, the first and last 128 samples are plotted as a function of time. It can be seen that the response pressure, that is, the pressure measured at the transducer end of the tubing system, is attenuated and lags the reference (orifice) pressure. The lag is approximately 120 degrees, which is the phase shift corresponding to the transfer function at  $f = 80$  Hz. However, the reconstructed pressure is in very close agreement with the reference pressure. The power spectral density function (PSD) for the reference pressure is shown in Figure D-6. This PSD is the average of two PSDs calculated from 4096-point, non-overlapping, data segments. The dominant frequency occurs at 80 Hz, as would be expected, and the PSD has an amplitude of 662 at this frequency (the vertical scale has been expanded to better show the noise components). The increased amplitude centered around a frequency of approximately 240 Hz is believed to be the speaker cavity resonance. In Figure D-7, the reconstruction error (i.e., reconstruction pressure – reference pressure) is plotted as a function of the reference pressure. The figure shows that there is essentially no correlation of error with pressure level ( $R^2 = 3.5 \times 10^{-5}$ ), and very little absolute error: mean error =  $-0.00004$  psi and one standard deviation of the error is 0.000662 psi. A histogram of the errors indicate that they form a very nearly normal distribution. Error parameters for the three runs are summarized in the table below. For the three runs the ratio of error standard deviation to signal standard deviation (0.016 psid) was only 0.04 or 4% error.

Table D-1 Reconstruction Error Summary

bias pressure, psid	correlation coefficient squared, $R^2$	mean error, psid	standard deviation, psid
+0.08	0.000035	-0.000040	0.000662
-0.08	0.0285	0.000198	0.000642
0	0.0154	0.000011	0.000661

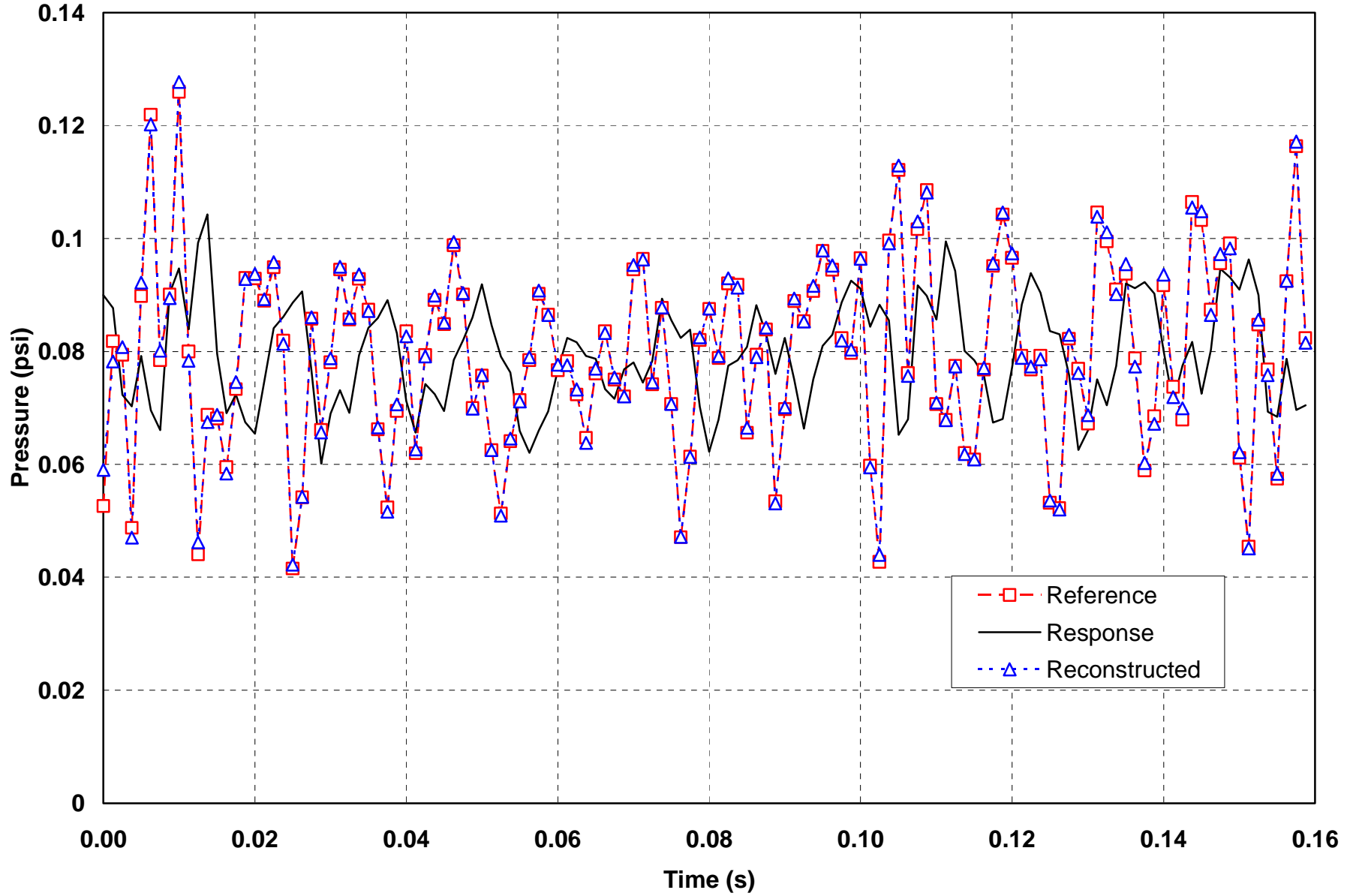


Figure D-4. Reconstruction of pressure during initial moments of positive bias proof of principle test

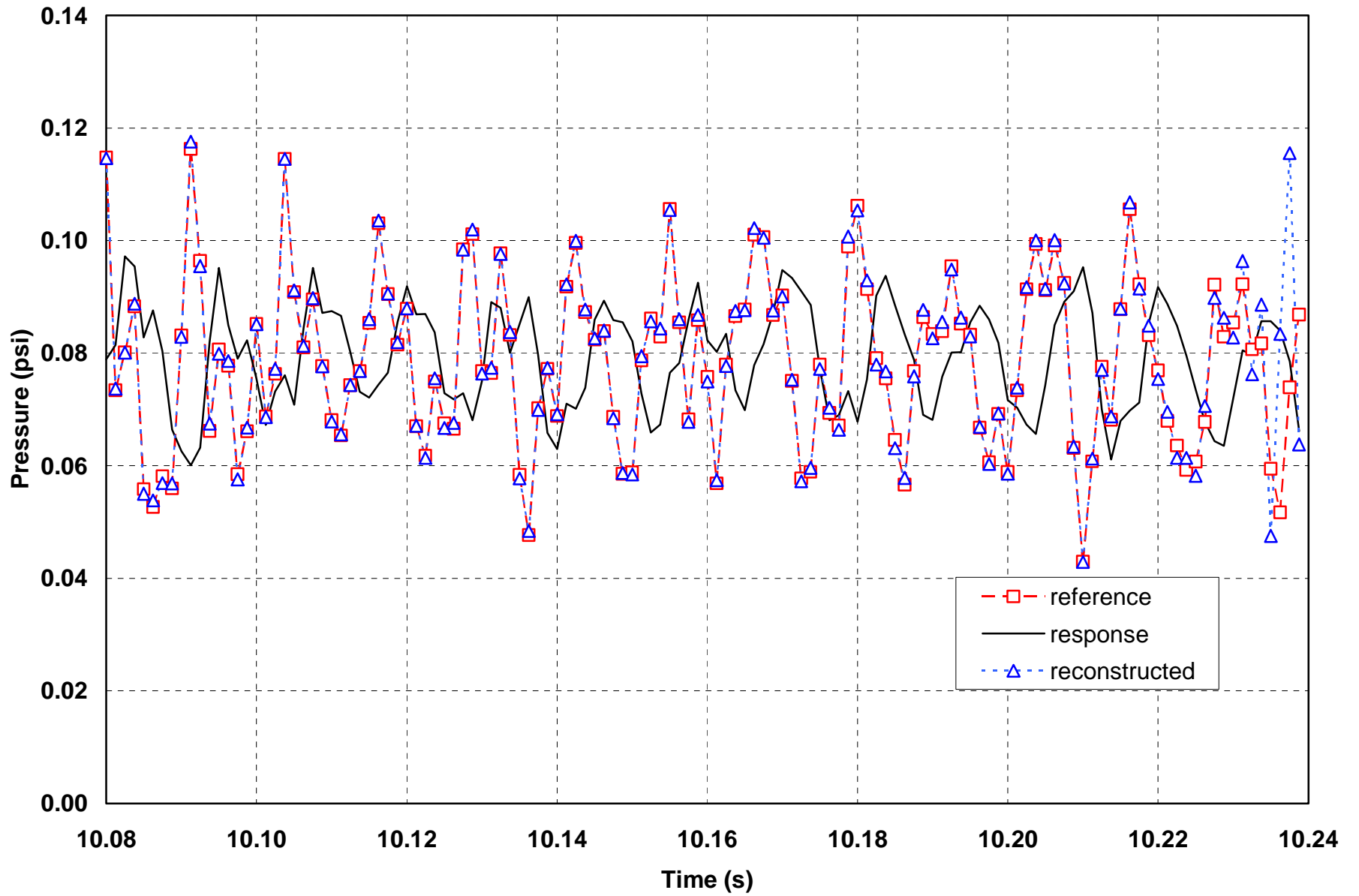


Figure D-5. Reconstruction of pressure during final moments of positive bias proof of principle test

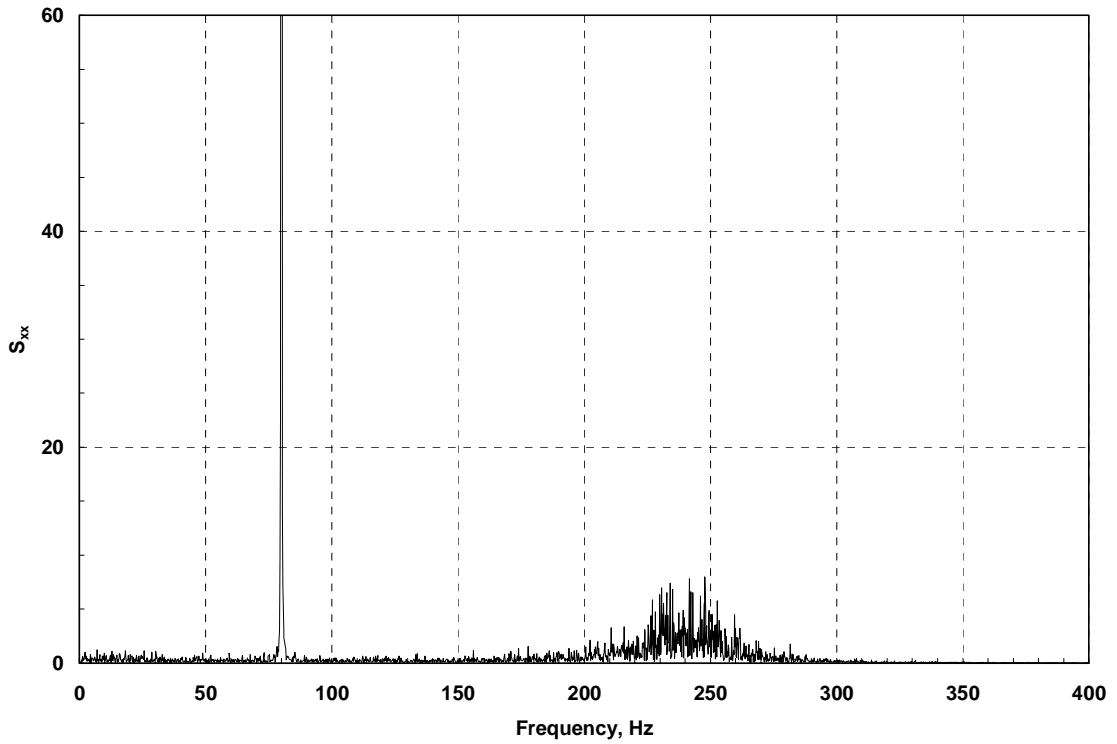


Figure D-6. Power spectral density for positive bias proof of principle test

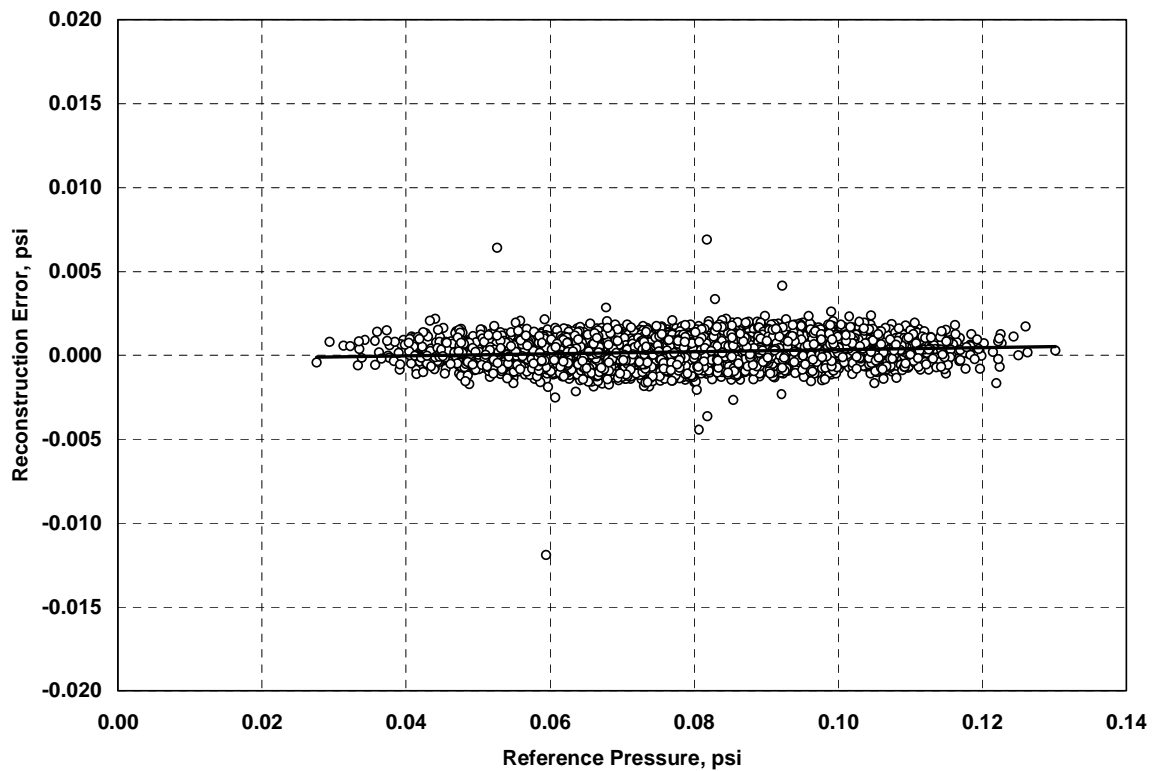


Figure D-7. Correlation of error with pressure level for positive bias proof of principle test

Although the reconstruction error was not correlated with pressure level, there was some correlation with time. Relatively small errors ( $< 0.007$  psig) occurred at the start of the reconstructed series (note Figure D-4) and lasted for as much as 16 samples. Much larger errors (0.06 psig), involving fewer samples, occurred at the end of the series (see Figure D-5). Since Fourier transformation operations are periodic, it is suspected that these errors, which appear to be primarily related to phase errors (the last few samples in Figure D-5 appear to be 180 degrees out of phase), are the result of using a discontinuous phase function in the calculations. It is recommended that the first and last few (~20) samples of the reconstructed pressures be discarded. It should be noted that the values in Table D-1 reflect error parameters with these points discarded.

## REFERENCES

- D-1 Irwin, H. P. A. H., Cooper, K. R., and Girard, R., "Correction of Distortion Effects Caused by Tubing Systems in Measurements of Fluctuating Pressures," *Journal of Industrial Aerodynamics*, Vol. 5, pp. 93-107, 1979.
- D-2 Sims-Williams, D. B. and Dominy, R. G., "Experimental Investigation in Unsteadiness and Instability in Passenger Car Aerodynamics", SAE Paper 98031, Detroit, MI, 1998.

## APPENDIX E

### TEST CONDITIONS

#### Unsteady Pressure Runs

Test conditions for the unsteady pressure runs (1 – 35) made with the Endevco transducers are given in Table E-1. The parameters listed are dynamic pressure,  $q_p$ , total temperature,  $T_o$ , static pressure,  $p_{sp}$ , velocity,  $V$ , and Reynolds number (based on ribbon width),  $Re_h$ . With the exception of  $T_o$ , all test conditions are based on pitot-static probe calibrations 18 inches upstream of the model.

Table E-1. Unsteady Pressure Runs

Run no.	$q_p$ (psi)	$T_o$ (deg R)	$p_{sp}$ (psia)	$V$ (ft/s)	$Re_h$ ( $h = 2$ in.)
1	0.08223	523.7	14.6771	100.269	104677
2	0.08240	524.2	14.6763	100.420	104652
3	0.08236	524.4	14.6766	100.418	104582
4	0.08223	524.6	14.6761	100.355	104441
5	0.08222	524.6	14.6769	100.349	104440
6	0.08217	524.8	14.6760	100.340	104353
7	0.05384	509.3	14.7327	79.884	87881
8	0.06742	509.5	14.7190	89.435	98273
9	0.08165	514.0	14.7181	98.849	106976
10	0.08240	514.7	14.7177	99.368	107278
11	0.08215	515.2	14.7176	99.263	106979
12	0.08196	515.6	14.7179	99.192	106755
13	0.08203	515.8	14.7177	99.251	106745
14	0.05309	516.3	14.7488	79.826	85800
15	0.05316	516.5	14.7483	79.894	85811
16	0.05326	516.5	14.7490	79.962	85889
17	0.05308	516.5	14.7490	79.830	85746
18	0.05307	516.5	14.7490	79.822	85738
19	0.08255	518.1	14.8292	99.412	106878
20	0.08291	518.3	14.8276	99.654	107055
21	0.08263	518.5	14.8263	99.505	106811
22	0.08243	518.6	14.8244	99.405	106653
23	0.08266	518.6	14.8226	99.549	106795
24	0.08217	518.8	14.8215	99.272	106416
25	0.05370	518.8	14.8230	80.274	85975
26	0.05374	518.8	14.8276	80.293	86022
27	0.05385	519.2	14.8316	80.392	86034
28	0.05375	519.2	14.8372	80.305	85972
29	0.05387	519.4	14.8408	80.398	86035
30	0.08270	528.7	14.7027	100.944	103802
31	0.08271	529.1	14.7029	100.991	103712
32	0.08264	529.3	14.7026	100.965	103614
33	0.05330	529.6	14.7334	81.048	83181
34	0.05320	529.3	14.7334	80.947	83160
35	0.05329	529.3	14.7327	81.018	83229

Average test conditions for the two test velocities are given in Table E-2.

Table E-2. Average Test Conditions for Unsteady Pressure Runs

$q_p$ (psi)	$T_o$ (deg R)	$P_{sp}$ (psia)	$V$ (ft/s)	$Re_h$ ( $h = 2$ in.)
0.08236 (11.860 psf)	521.0	14.7354	99.889	105681
0.05438 (7.830 psf)	519.0	14.7704	80.889	86316

### Steady-State Pressure Runs

Unfortunately, the absolute static ring pressure,  $p_{sr}$ , was not recorded during steady-state pressure measurements made with the PSI system. Also,  $T_o$  was not recorded for runs 47 – 50. This precluded calculation of the static pressure,  $p_{sp}$ , velocity,  $V$ , and Reynolds number,  $Re_h$ . Values given in Tables E-3 and E-4 below are based on actual  $q_p$ , actual  $T_o$  for runs 51 – 56, estimated  $T_o$  for runs 47 – 50, and estimated  $p_{sp}$  for all runs (average values from runs 1 – 35). Estimated values are shown in italics.

Table E-3. Steady-State Pressure Runs

Run no.	$q_p$ (psi)	$T_o$ (deg R)	$p_{sp}$ (psia)	$V$ (ft/s)	$Re_h$ ( $h = 2$ in.)
47	0.05485	520.1	14.7704	81.374	86300
48	0.05473	520.1	14.7704	81.287	86207
49	0.05467	520.1	14.7704	81.240	86158
50	0.05447	520.1	14.7704	81.090	85998
51	0.05451	520.3	14.7704	81.135	85987
52	0.08311	519.9	14.7354	100.236	106125
53	0.08293	520.1	14.7354	100.147	105958
54	0.08260	520.1	14.7354	99.950	105749
55	0.08257	520.4	14.7354	99.958	105650
56	0.08261	520.4	14.7354	99.982	105675

Average test conditions for the two test velocities are given in Table E-4.

Table E-4. Average Test Conditions for Steady-State Pressure Runs

$q_p$ (psi)	$T_o$ (deg R)	$P_{sp}$ (psia)	$V$ (ft/s)	$Re_h$ ( $h = 2$ in.)
0.05465 (7.869 psf)	520.1	14.77040	81.225	90095
0.08276 (11.918 psf)	520.2	14.73540	100.055	105758

Intentionally Left Blank

## APPENDIX F

### MEASUREMENT UNCERTAINTY ANALYSIS

The first step is to identify and quantify the elemental errors which influence each measurement. Obviously, it is impossible to even identify all elemental errors, let alone to quantify them. It is important that the experimenters try to at least identify the significant errors. The errors are then categorized as bias errors,  $B$ , or precision errors,  $S$ . In general, precision errors contribute to noise in the test data and bias errors do not. More precisely, precision errors affect the standard deviation of the data and bias errors affect the mean of the data. This step is definitely the most difficult part of the analysis. The elemental errors are then combined for each measurement by calculating the root-sum-square value, for example, with precision errors attributed to “nonlinearity”, “hysteresis,” and “nonrepeatability,”

$$S_{RSS} = (S_{nl}^2 + S_h^2 + S_{nr}^2)^{1/2}. \quad (F-1)$$

Results of following this process for the current test will be shown later in Table F-2. Considerable caution must be exercised in categorizing the errors. For example, during pressure measurements in the test, transducer hysteresis errors are precision. However, these same errors occurring during the transducer calibration are “fossilized” and become bias errors, that is, they cannot contribute to increased standard deviation in the test measurements. At this stage of the analysis, the bias and precision errors are kept separate for use in estimating the uncertainty in calculated results. If uncertainty in a measurement is required, for example, for  $\Delta p_i$  in the present report, it is calculated with the 95-percent confidence method which defines uncertainty,  $U$ , as

$$U = [B^2 + (2S)^2]^{1/2}. \quad (F-2)$$

With this definition,  $B$  is the maximum expected bias error and  $S$  is the standard deviation.

The next step is to identify nominal (i.e., average) values for the principal variables. These values will be required to estimate the error in calculated results such as  $C_p$ . For a calculated result,  $R$ , it is necessary to propagate errors from the basic measurements into the uncertainty for the result. Let the result,  $R$ , be represented by the function

$$R = f(x_1, x_2, \dots, x_i). \quad (F-3)$$

Using the Taylor series method of propagation, the bias limit,  $B$ , for  $R$  is given by,

$$B_R^2 = \left( \frac{\partial R}{\partial x_1} B_{x_1} \right)^2 + \left( \frac{\partial R}{\partial x_2} B_{x_2} \right)^2 + \dots + \left( \frac{\partial R}{\partial x_i} B_{x_i} \right)^2 + 2 \frac{\partial R}{\partial x_1} \frac{\partial R}{\partial x_2} B_{x_1}' B_{x_2}' + \dots \quad (F-4)$$

where  $B_{x_1}'$  and  $B_{x_2}'$  are the portions of the bias limits for measurements of  $x_1$  and  $x_2$  that arise from the same sources and are assumed to be perfectly correlated. A similar relation is used to propagate the precision error in  $R$ ,

$$S_R^2 = \left( \frac{\partial R}{\partial x_1} S_{x_1} \right)^2 + \left( \frac{\partial R}{\partial x_2} S_{x_2} \right)^2 + \dots + \left( \frac{\partial R}{\partial x_i} S_{x_i} \right)^2 + 2 \frac{\partial R}{\partial x_1} \frac{\partial R}{\partial x_2} S_{x_1}' S_{x_2}' + \dots \quad (F-5)$$

Uncertainty in the result is calculated with the 95-percent confidence method,

$$U_R = [B_R^2 + (2S_R)^2]^{1/2}. \quad (\text{F-6})$$

In the present test, several averaged results were used. Averaging reduces the precision error, but does not affect bias error. If the standard deviation reduction due to averaging is denoted as  $S_{\bar{R}}/S_R$ , then the uncertainty is given by

$$U_R = \left\{ B_R^2 + \left[ 2 \left( \frac{S_{\bar{R}}}{S_R} \right) S_R \right]^2 \right\}^{1/2}. \quad (\text{F-7})$$

For independent (uncorrelated) measurements,  $S_{\bar{R}}/S_R = 1/\sqrt{n}$ , where  $n$  is the number of measurements averaged. For correlated data, evaluation of  $S_{\bar{R}}/S_R$  is more complicated and is described in Appendix B. Although it might appear that the measurement precision errors are independent, they are driven by the fluctuating pressures and are, therefore, correlated like the pressures.

A brief bibliography of selected references on measurement uncertainty is given at the end of this appendix.

### **Nominal Test Conditions**

Nominal test conditions are required in the uncertainty analysis. Measured test conditions were: tunnel reference differential pressure,  $p_r - p_{sr}$  (denoted as  $\Delta p_r$  in the uncertainty analysis), static ring pressure,  $p_{sr}$ , and total temperature,  $T_o$ . From these measured conditions, static pressure,  $p_{sp}$ , dynamic pressure,  $q_p$ , and velocity,  $V$ , were calculated. Average values of these parameters were used to reduce the pressure coefficient data for each run. Average values of  $C_p$  from run 52 were used to define the nominal  $C_p$ . Because of the large difference in windward and leeward  $C_p$  values, two values will be used. Nominal values of the model differential pressure,  $\Delta p_i = p_i - p_{sr}$ , were calculated from  $C_p$ . Finally, the tunnel test condition calibration factors,  $k_1$  and  $k_2$ , appear in many of the uncertainty calculations. A summary of the nominal test conditions, for  $V \approx 100$  ft/s, is presented in Table F-1.

Table F-1 Nominal Test Conditions ( $V = 100$  ft/s)

Parameter	Symbol	Value
Reference differential	$\Delta p_r \equiv p_r - p_{sr}$	0.1033 psid
Total temperature	$T_o$	61 deg F = 521 deg R
Static pressure	$p_{sp}$	14.735 psia
Dynamic pressure	$q_p$	0.0824 psi
Velocity	$V$	99.89 ft/s
Pressure coefficient	$C_p$ (windward)	0.84
	$C_p$ (leeward)	-1.25
Differential pressure	$\Delta p_i$ (windward)	0.0922 psid
	$\Delta p_i$ (leeward)	-0.0811 psid
	$\Delta p_i$ (average)	$\pm 0.085$ psid
Static pressure calib.	$k_1$	0.2148
Dynamic pressure calib.	$k_2$	0.797

### **Differential Pressure Errors (Endevco Transducers)**

The pressure errors are summarized in Table F-2. Details are given in the sections below, and except where noted, apply to both model and tunnel reference pressures since all were measured with the same type of transducer.

#### **Calibration error**

The calibration error (bias) is the result of fossilized precision error in the standard (Paroscientific Digiquartz Pressure Standard, 15 psia full scale). The manufacturer's error specifications for repeatability and hysteresis are both  $\pm 0.005\%$  of full scale. This results in a combined error of 0.00707% of full scale. Thus,

$$B = (0.00707/100) (15) = 0.00106 \text{ psid.}$$

This error applies to both model and reference pressure measurements.

#### **Zero shifts**

Efficient operation of the tunnel required that several runs be made (as many as 11 in one series) between acquiring air-off zeros. These zero shifts produce a bias error in both the model pressures,  $\Delta p_i$ , and the tunnel reference pressure,  $\Delta p_r$ . Analysis of the zero shifts from 14 transducers and six sets of test runs (84 samples) gave a standard deviation of the zero shifts as 0.00028 psid. Since this is a bias error, the maximum will be approximated by two standard deviations,

$$B = 0.00056 \text{ psid.}$$

For the reference transducer,

$$B = 0.00016 \text{ psid.}$$

This error is significantly smaller than that for the model pressures. The difference is believed to be a result of the much lower magnitude of pressure fluctuations experienced by this transducer during testing.

### Transducer error

Transducer error results from three sources: nonlinearity, hysteresis, and nonrepeatability. Temperature error is believed to be insignificant since the transducers were mounted in a steel heat sink and were insulated from the tunnel flow. Also, any thermal shifts should be included in the zero shifts. Unknown errors include model orifice irregularities (care was taken during fabrication to insure that the orifices were smooth, circular, and normal to the surface), vibration of the transducer (alleviated by positioning the transducer diaphragms for minimum effect), and variation in analog/digital conversion. These errors are believed to be insignificant. The 14 transducers used to measure model pressures,  $\Delta p_i$ , will be considered first. Errors will be estimated from the six calibrations made at NASA Ames during March, 1999.

Our calibrations used a least squares fit of the function,  $e = bp$ , where  $e$  is the output of the signal conditioner in volts and  $p$  is the applied pressure in psid. Although this model usually increases the error over that for the standard linear model,  $e = a + bp$ , it was felt that it would provide a more realistic estimate of the error since this is the model used in data reduction, that is,  $p = e/b$ , so  $p = 0$  for  $e = 0$ .

Nonlinearity and hysteresis will be combined and are represented by the maximum deviation from the calibration regression line. The maximum deviation, without regard to sign, in volts was converted to psid by multiplying by the scale factor,  $1/b$ . One transducer (channel 5) had a deviation which exceeded the average by more than  $2\sigma$  and was deleted. For the remaining 13 transducers which measured model pressures,

$$\text{maximum deviation} = 0.00066 \text{ psid.}$$

This is the maximum error, not the standard deviation. Treating this uncertainty as random, since the pressure at which the maximum error occurs is variable, the value should be divided by 2 since it will later be combined with standard deviations and multiplied by 2 in the uncertainty calculation. Thus, the precision error attributed to nonlinearity and hysteresis is

$$S_{nl,h} = 0.00033 \text{ psid.}$$

Repeatability is defined as the ability of the transducer to repeat an output value when the same pressure is applied repeatedly. As a measure of the nonrepeatability, the standard deviation of the calibration slopes ( $1/b$ ) will be used. This should provide more accurate results than simply checking the output at a single pressure. Nonrepeatability is calculated at the nominal test pressure of 0.085 psid. This pressure corresponds to a nominal output voltage,  $e_{nom}$ , of

$$\begin{aligned} e_{nom} &= b \Delta p_{nom} \\ &= (1/0.02347)(0.085) \\ &= 3.622 \text{ volts.} \end{aligned}$$

Then, error in  $\Delta p$  due to nonrepeatability is,

$$S_{nr} = S_{1/b} e_{nom} .$$

The pooled average of the standard deviations of the calibration slopes is 0.0000494 psid/volt, so

$$S_{nr} = (0.0000494) (3.622) = 0.00018 \text{ psid.}$$

For the tunnel reference differential pressure,  $\Delta p_r$ , the analysis is somewhat different. First, individual measurements of  $\Delta p_r$  are never used in calculating pressure coefficients, only the average of 8192 samples. Therefore, errors in  $\Delta p_r$  are bias, not precision. Second, only a single calibration was made with the transducer used to measure  $\Delta p_r$ . From this calibration, the maximum deviation from the regression line was 0.00338 psid. This can be treated as a precision error for each sample recorded during a test run. Averaging the samples will greatly reduce this error. It is shown in Appendix B, that for a sampling duration of 10.24 s, the ratio of the standard deviation of the average to the standard deviation of the samples,  $S_{\bar{R}}/S_R$ , was 0.048 (see Table B-4). Then the nonlinearity and hysteresis error is

$$B_{nl,h} = (0.00338) (0.048) = 0.00016 \text{ psid}$$

where the error is now classified as a bias error since the average is a constant and has no precision error.

Because only a single calibration was made on the  $\Delta p_r$  transducer, the repeatability cannot be estimated from the standard deviation of the slopes as was done for the other transducers. However, since the transducers are similar (same model number and range) they should have similar repeatability. It was assumed that the ratio of standard deviation to the mean of  $1/b$  would be the same,

$$\frac{S_{1/b}}{1/b} = \frac{0.0000494}{0.02347} = 0.002105 .$$

That is, the uncertainty in the slope is approximately 0.2%. Multiplying this ratio by the  $\Delta p_r$  scale factor provides an estimate of the repeatability of the  $\Delta p_r$  slope,

$$S_{1/b} = (0.002105) (0.1962) = 0.000413 .$$

Finally, for the nominal pressure of 0.1033 psid, the nominal voltage is

$$e_{nom} = (1/0.1962) (0.1033) = 0.527 \text{ volt}$$

and the nonrepeatability error is,

$$S_{nr} = (0.000413) (0.527) = 0.000217 \text{ psid.}$$

Reducing the error for the effects of averaging gives the bias error due to nonrepeatability,

$$B_{nr} = (0.000217) (0.048) = 0.00001 \text{ psid.}$$

Finally, the pressure measurement elemental errors described above can be combined by category, using the root-sum-square method defined in Equation (F-1), to give the overall bias and precision errors. The uncertainty is estimated with Equation (F-2).

Model differential pressures,  $\Delta p_i$ :

$$B_{\Delta p_i} = (0.00106^2 + 0.00056^2)^{1/2} = 0.00120$$

$$S_{\Delta p_i} = (0.00033^2 + 0.00018^2)^{1/2} = 0.00038$$

$$U_{\Delta p_i} = [0.00120^2 + (2 \times 0.00038)^2]^{1/2} = 0.00142 \quad .$$

Reference differential pressure,  $\Delta p_r$ :

$$B_{\Delta p_r} = (0.00106^2 + 0.00016^2 + 0.00016^2 + 0.00001^2)^{1/2} = 0.00108$$

$$S_{\Delta p_r} = 0$$

$$U_{\Delta p_r} = [0.00108^2 + (2 \times 0.0)^2]^{1/2} = 0.00108 \quad .$$

The manufacturer's error specifications for combined nonlinearity, hysteresis and nonrepeatability is 1.5% full scale, which equals 0.015 psid. This error is much larger than our estimates. It should be noted that this is not at all an uncommon result for any experimentalist who does his own careful calibrations and his own uncertainty analysis. The manufacturer's specification may be conservative to include a larger population of transducers and may include the uncertainty for transducers which are not calibrated by the user. Also, since we calibrated the transducers to only 20% of full scale rating, nonlinearity and hysteresis errors were significantly reduced.

The major source of uncertainty in our pressure measurements is the calibration standard. In future tests, use of a 1-psid standard should significantly improve the accuracy of  $\Delta p_i$ .

### **Tunnel Freestream Conditions Calibration Errors (Endevco Transducers)**

As described in Appendix A, the tunnel freestream conditions were calculated from constants obtained during pitot-static tube calibrations upstream of the model. The two calibration equations are

$$p_{sp} - p_{sr} = k_1 \Delta p_r$$

and

$$q_p = k_2 \Delta p_r$$

where  $p_{sp}$  and  $q_p$  are the probe static and dynamic pressures, respectively. Because only the average values of  $\Delta p_r$  are used in calculating average freestream conditions, the errors associated with  $k_1$  and  $k_2$  are bias. Errors in the calibration standard do not influence these calculations—bias errors in the standard are eliminated during transducer calibration and precision errors cancel since both the dependent and independent variables are calibrated with the same standard. The first source of error is the result of zero shifts that occurred during the probe calibration runs. For the three parameters, the shifts were

$$\begin{aligned}\Delta p_r &= 0.000032 \text{ psid} \\ p_{sp} - p_{sr} &= -0.000083 \text{ psid} \\ q_p &= 0.000121 \text{ psid}.\end{aligned}$$

Because the calibration model,  $y=bx$ , forces the linear curve through the origin, bias errors (zero shifts) in any of the parameters will change the values of  $k_1$  and  $k_2$ . An estimate of the error resulting from zero shifts was made by comparing the basic data fits to ones with the data perturbed by the  $x$  and  $y$  errors listed above. The results gave maximum bias errors in  $k_1$  and  $k_2$  as follows:

$$B_{k_1} = 0.00096 \text{ and } B_{k_2} = 0.00115 .$$

A second source of error for the calibration constants  $k_1$  and  $k_2$  is derivative uncertainty due to precision errors in the basic data. From Ref. F-1, the combined precision error in a derivative estimate is

$$S_i = (S_{\Delta p}^2 + b_i^2 S_{\Delta p_r}^2)^{1/2}, \quad i = 1, 2 \quad (\text{F-8})$$

where  $\Delta p$  is the dependent variable,  $\Delta p_r$  the independent variable, and  $b_i$  the derivative. Then, the precision error in the derivative is given by

$$S_{k_i} \equiv S_{b_i} = S_i / \sqrt{\sum (\Delta p_r)^2} . \quad (\text{F-9})$$

For the pitot-static tube calibrations, the differential pressures are averages of 8192 samples (10.24 s). Assuming that the pitot-static tube measurements have an autocorrelation function similar to that for the windward model pressures, the precision error is reduced by a factor of 0.0695 for the average (see Table B-4). Earlier it was shown that  $S_{nl,h,\&nr}$  for the transducers was equal to 0.00038 psid, then the precision error for the average is

$$S_{\Delta p} = (0.0695) (0.00038) = 0.00003 \text{ psid}.$$

For the average reference differential pressure, combining nonlinearity and hysteresis error with nonrepeatability error,

$$S_{\Delta p_r} = (0.00016^2 + 0.00001^2)^{1/2} = 0.00016$$

(actually, this was typed as a bias error, but the magnitude is the same). Finally,

$$\sqrt{\sum (\Delta p_r)^2} = 0.2012 .$$

Then,

$$S_{k_1} = \frac{[(0.00003)^2 + (0.2148)^2 (0.00016)^2]^{1/2}}{0.2012} = 0.00023$$

and

$$S_{k_2} = \frac{[(0.00003)^2 + (0.797)^2 (0.00016)^2]^{1/2}}{0.2012} = 0.00065 .$$

As might be expected, since the derivative errors are based on heavily averaged pressures, the errors due to zero shifts are much larger than the derivative errors. Because these errors do not contribute to the noise in the  $C_p$  calculations, they are fossilized as bias errors.

Finally, combining the zero shift and derivative errors gives the overall bias error which is also equal to the uncertainty since the precision error is zero.

$$U_{k_1} = B_{k_1} = (0.00096^2 + 0.00023^2)^{1/2} = 0.00099$$

$$U_{k_2} = B_{k_2} = (0.00115^2 + 0.00065^2)^{1/2} = 0.00132$$

### **Differential Pressure Errors (PSI System)**

#### **Calibration error**

The calibration standard (PCU) used for this test had a full scale range of 1.0 psid and an accuracy of 0.01% of full scale. Therefore, the calibration error (bias) is

$$B = 0.00010 \text{ psid.}$$

#### **Zero shifts**

Calibration procedures are different for the two systems. For the Endevco transducers, multiple pre-test calibrations were made and the results were averaged for use in data reduction. The calibration equation is linear with zero intercept. Therefore, frequent zeros are required to insure that the data conforms to this model. Zero shifts then become a source of bias error. For the PSI system, a calibration is usually performed immediately before the data are acquired, and the transducers can even be calibrated while the tunnel is running. The calibration equation is fourth-order, calculated from five calibration points. The equation has an offset term at zero voltage, so zeros are not necessary. For the current test, calibrations were performed only before each of the two series of five runs. Each series required about 22 minutes of elapsed time. Any transducer shifts during this period would create bias error, however changes in the calibration were not determined since the calibration coefficients were not recorded. The major source of calibration shift during the runs would be temperature changes. However, temperature changes are felt to be insignificant because the ESP module was mounted in a temperature-controlled oven and shielded from the tunnel flow. In any case, although shifts are an error source, they cannot be quantified. These comments also apply to the five runs used to determine the tunnel condition constants,  $k_1$  and  $k_2$ .

#### **Transducer error**

Transducer error (nonlinearity, hysteresis, and nonrepeatability) could not be evaluated for the PSI module as it was for the Endevco transducers. Therefore, we will use the manufacturer's specification for worst error with a 5-point calibration, which is  $\pm 0.10\%$  full scale. For the ESP module's full scale pressure of 10" WC (0.36 psi) the error is then

$$S_{nl,h,\&nr} = \pm 0.00036 \text{ psid.}$$

The pressure coefficients were calculated using the average tunnel reference differential pressure,  $\Delta p_r$ . Two hundred sets of 127 samples were averaged. It is shown in Appendix B that the precision error is reduced by a factor of 0.0468 as a result of the averaging operation and becomes a bias error,

$$B_{nl,h,&nr} = (0.0468)(0.00036) = 0.00002 \text{ psid.}$$

Combining the elemental errors to obtain overall bias and precision errors, and calculating the uncertainty gives

Model differential pressures,  $\Delta p_i$ :

$$B_{\Delta p_i} = 0.00010$$

$$S_{\Delta p_i} = 0.00036$$

$$U_{\Delta p_i} = [0.00010^2 + (2 \times 0.00036)^2]^{1/2} = 0.00073 \text{ .}$$

Reference differential pressure,  $\Delta p_r$ :

$$B_{\Delta p_r} = (0.00010^2 + 0.00002^2)^{1/2} = 0.00010$$

$$S_{\Delta p_r} = 0$$

$$U_{\Delta p_r} = [0.00010^2 + (2 \times 0.0)^2]^{1/2} = 0.00010 \text{ .}$$

### **Tunnel Freestream Conditions Calibration Errors (PSI System)**

Zero shift error should be negligible. The derivative error (see explanation under Endeveco transducers) is based on average measurements of  $\Delta p$ , so the error is reduced for this measurement by 0.0258 (see Table B-4). Then

$$S_{\Delta p} = (0.0258)(0.00036) = 0.00001 \text{ psid.}$$

For the reference transducer,

$$S_{\Delta p_r} = 0.00002 \text{ psid.}$$

Since an additional calibration point was taken with the PSI system,

$$\sqrt{\sum (\Delta p_r)^2} = 0.2733.$$

Then

$$S_{k_1} = \frac{[(0.00001)^2 + (0.2148)^2 (0.00002)^2]^{1/2}}{0.2733} = 0.00004$$

$$S_{k_2} = \frac{[(0.00001)^2 + (0.7865)^2 (0.00002)^2]^{1/2}}{0.2733} = 0.00007 \text{ .}$$

Because  $k_1$  and  $k_2$  do not introduce noise, the errors are treated as bias. It should be noted that  $k_1$  and  $k_2$  are independent of the measuring system, they depend only on the probe position. Therefore, the two calibrations should provide an indication of accuracy. Results of the calibrations with the two systems are shown in the following table:

System \ Derivative	$k_1$	$k_2$
Endevco	0.2148	0.7970
PSI	0.2148	0.7865

There is no difference in the values of  $k_1$ , but there is a  $\pm 0.0052$  difference in the  $k_2$  values. This difference is considerably larger than the estimated uncertainty in  $k_2$  and may be the result of neglected errors or, more likely, small differences in locating and aligning the pitot-static probe for the two measurements. Also, the pressure sensitive paint (PSP) box was not present in the tunnel for the Endevco calibration, but was present for the PSI calibration. However, comparison of  $k_2$  values obtained with the Endevco transducers, with and without the PSP box, showed a difference in  $k_2$  of only 0.0009.

Table F-2. Measurement Error Summary

Parameter	Error source	Endevco		PSI	
		Bias limit, $B$	Precision error, $S$	Bias limit, $B$	Precision error, $S$
$\Delta p_i$	calibration	0.00106 psid		0.00010 psid	
	zero shifts	0.00056 psid		unknown	
	nl & h		0.00033 psid		0.00036 psid
	nr		0.00018 psid		
	RSS	0.00120 psid	0.00038 psid	0.00010 psid	0.00036 psid
	uncertainty	0.00142 psid		0.00073 psid	
$\Delta p_i$	reconstruction	0.00020 psid	0.00066 psid		
(reconstructed)	RSS*	0.00122 psid	0.00076 psid		
	uncertainty*	0.00144 psid			
$\Delta p_r$	calibration	0.00106 psid		0.00010 psid	
(averaged)	zero shifts	0.00016 psid		unknown	
	nl & h	0.00016 psid		0.00002 psid	
	nr	0.00001 psid			
	RSS	0.00108 psid		0.00010 psid	
	uncertainty	0.00108 psid		0.00010 psid	

Table F-2 (cont.)

Parameter	Error source	Endevco		PSI	
		Bias limit, $B$	Precision error, $S$	Bias limit, $B$	Precision error, $S$
$k_1$	zero shifts	0.00096		unknown	
	derivative unc.	0.00023		0.00004	
	RSS	0.00099		0.00004	
$k_2$	zero shifts	0.00115		unknown	
	derivative unc.	0.00065		0.00007	
	RSS	0.00132		0.00007	

Notes:

nl & h – nonlinearity and hysteresis errors

nr – nonrepeatability error

RSS – root-sum-square error

$$\text{uncertainty} = [B^2 + (2S)^2]^{1/2}$$

RSS\*, uncertainty\* = root-sum-square error and uncertainty for basic  $\Delta p_i$  with reconstruction error

### Propagation of Error—Pressure Coefficient, $C_p$

Having defined the precision and bias errors for the pressure measurements, it is now necessary to propagate these errors into the calculation of pressure coefficient. Precision and bias errors are propagated separately and then combined for the uncertainty. The definition of  $C_p$  for this test was (see Appendix A),

$$C_p = \frac{\Delta p_i - k_1 \Delta p_r}{k_2 \Delta p_r} \quad (\text{F-10})$$

where

$$\begin{aligned} \Delta p_i &= p_i - p_{sr} \\ \Delta p_r &= (p_r - p_{sr})_{avg} \\ k_1 &= \frac{d(p_{sp} - p_{sr})}{d\Delta p_r} \\ k_2 &= \frac{dq_p}{d\Delta p_r} \end{aligned} \quad (\text{F-11})$$

The four parameters used to calculate  $C_p$  —  $\Delta p_i$ ,  $\Delta p_r$ ,  $k_1$ , and  $k_2$ , are independent which makes the evaluation much simpler since cross-product terms are not required. Although  $k_1$  and  $k_2$  are functions of  $\Delta p_r$ , their errors are fossilized as bias errors, making them independent, that is, they are simply numbers with bias errors.

Using the Taylor series method,

$$S_{C_p} = \left[ \left( \frac{\partial C_p}{\partial \Delta p_i} S_{\Delta p_i} \right)^2 + \left( \frac{\partial C_p}{\partial \Delta p_r} S_{\Delta p_r} \right)^2 + \left( \frac{\partial C_p}{\partial k_1} S_{k_1} \right)^2 + \left( \frac{\partial C_p}{\partial k_2} S_{k_2} \right)^2 \right]^{1/2} \quad (\text{F-12})$$

Calculating the indicated partial derivatives gives

$$\begin{aligned} \frac{\partial C_p}{\partial \Delta p_i} &= \frac{1}{k_2 \Delta p_r} \\ \frac{\partial C_p}{\partial \Delta p_r} &= - \left( \frac{k_1}{k_2 \Delta p_r} + \frac{\Delta p_i - k_1 \Delta p_r}{k_2 \Delta p_r^2} \right) \\ \frac{\partial C_p}{\partial k_1} &= - \frac{1}{k_2} \\ \frac{\partial C_p}{\partial k_2} &= - \frac{\Delta p_i - k_1 \Delta p_r}{k_2^2 \Delta p_r} \end{aligned} \quad (\text{F-13})$$

In addition to these analytical expressions, the partial derivatives were checked numerically by using a centered-difference perturbation technique. Substituting the derivatives into the equation for precision error gives,

$$S_{C_p} = \frac{1}{k_2 \Delta p_r} \left[ S_{\Delta p_i}^2 + (k_1 + k_2 C_p)^2 S_{\Delta p_r}^2 + (\Delta p_r)^2 S_{k_1}^2 + (\Delta p_r C_p)^2 S_{k_2}^2 \right]^{1/2} \quad (\text{F-14})$$

The bias error is similar,

$$B_{C_p} = \frac{1}{k_2 \Delta p_r} \left[ B_{\Delta p_i}^2 + (k_1 + k_2 C_p)^2 B_{\Delta p_r}^2 + (\Delta p_r)^2 B_{k_1}^2 + (\Delta p_r C_p)^2 B_{k_2}^2 \right]^{1/2}. \quad (\text{F-15})$$

The uncertainty,  $U_{C_p}$ , is given by,

$$U_{C_p} = \left[ B_{C_p}^2 + (2S_{C_p})^2 \right]^{1/2}. \quad (\text{F-16})$$

### Evaluation—Endevco transducers

Using the propagation equations above, and error values listed in Table F-2, the uncertainty in  $C_p$  is calculated below for both windward and leeward pressures.

#### Unaveraged $C_p$ , windward side (nominal $C_p = 0.84$ ):

$$S_{C_p} = 0.00462$$

$$B_{C_p} = 0.01872$$

$$U_{C_p} = \left\{ (0.01872)^2 + [(2)(0.00462)]^2 \right\}^{1/2} = 0.02087.$$

#### Unaveraged $C_p$ , leeward side (nominal $C_p = -1.25$ ):

$$S_{C_p} = 0.00462$$

$$B_{C_p} = 0.01798$$

$$U_{C_p} = \left\{ (0.01798)^2 + [(2)(0.00462)]^2 \right\}^{1/2} = 0.02021.$$

#### Averaged $C_p$ , windward side:

For the average, the precision error is reduced by  $S_{\bar{x}}/S_x$  which is equal to 0.0695 (see Table B-4) for a 10.24-second averaging time. The bias error is not affected. Then,

$$U_{\bar{C}_p} = \left\{ (0.01872)^2 + [(2)(0.0695)(0.00462)]^2 \right\}^{1/2} = 0.01873.$$

#### Averaged $C_p$ , leeward side:

The precision error reduction factor is 0.0775,

$$U_{\bar{C}_p} = \left\{ (0.01798)^2 + [(2)(0.0775)(0.00462)]^2 \right\}^{1/2} = 0.01800.$$

Although not a measurement error, there is additional uncertainty in the averaged  $C_p$  which results from data variance caused by fluctuations in the flow. This is discussed in detail in Appendix B. For the Endevco transducers, the relative uncertainty in averaged  $C_p$  is 0.00223 for the windward side and 0.00668 for the leeward side. Then, uncertainty in average  $C_p$  is 0.00187 for the windward pressures and 0.00835 for the leeward pressures. The leeward pressure uncertainty is significantly larger than the windward because the variance was much

larger in the leeward pressures and increased correlation in the leeward data reduced the effect of averaging.

### **Evaluation—PSI system**

#### **Unaveraged $C_p$ , windward side (nominal $C_p = 0.84$ )**

$$S_{C_p} = 0.00437$$

$$B_{C_p} = 0.00163.$$

Because the “unaveraged”  $C_p$  values measured with the PSI system are actually averages of 127 frames (0.33 s), a variance reduction factor of 0.3646 (see Table B-4) must be included in the uncertainty estimate,

$$U_{C_p} = \left\{ (0.00163)^2 + [(2)(0.3646)(0.00437)]^2 \right\}^{1/2} = 0.00358.$$

#### **Unaveraged $C_p$ , leeward side (nominal $C_p = -1.25$ )**

$$S_{C_p} = 0.00437$$

$$B_{C_p} = 0.00155.$$

For the leeward side, the variance reduction factor is 0.4110,

$$U_{C_p} = \left\{ (0.00155)^2 + [(2)(0.4110)(0.00437)]^2 \right\}^{1/2} = 0.00391$$

#### **Averaged $C_p$ , windward side**

For the average, the precision error is reduced by  $S_{\bar{x}}/S_x$  which is equal to 0.0258 (see Table B-4) for a 200-set average. The bias error is not affected. Then,

$$U_{\bar{C}_p} = \left\{ (0.00163)^2 + [(2)(0.0258)(0.00437)]^2 \right\}^{1/2} = 0.001645.$$

#### **Averaged $C_p$ , leeward side**

The precision error reduction factor is 0.0291,

$$U_{\bar{C}_p} = \left\{ (0.00155)^2 + [(2)(0.0291)(0.00437)]^2 \right\}^{1/2} = 0.001571.$$

Again, there is uncertainty in the averaged  $C_p$  which results from data variance caused by fluctuations in the flow. For the PSI system, the uncertainty in average  $C_p$  is 0.00070 for the windward pressures and 0.00314 for the leeward pressures.

### **Propagation of Error—Test Conditions**

The two test conditions of interest are dynamic pressure,  $q$ , and velocity,  $V$ .

#### **Dynamic pressure**

The average dynamic pressure was calculated from

$$q = k_2 \Delta \bar{p}_r . \quad (\text{F-17})$$

The bias error for  $q$  is,

$$B_q = \left[ \left( k_2 B_{\Delta \bar{p}_r} \right)^2 + \left( \Delta \bar{p}_r B_{k_2} \right)^2 \right]^{1/2} . \quad (\text{F-18})$$

Endevco transducers:

$$U_q = B_q = 0.00087 \text{ psi.}$$

PSI system:

$$U_q = B_q = 0.00008 \text{ psi.}$$

### Static Pressure and Velocity

The average velocity was calculated from

$$V = \left( \frac{2RTq}{p_{sp}} \right)^{1/2} . \quad (\text{F-19})$$

Since

$$T = \frac{T_0}{1 + 0.2M^2} \quad (\text{F-20})$$

and

$$M^2 = \frac{q}{0.7 p_{sp}} , \quad (\text{F-21})$$

then

$$V = \left( \frac{7RqT_0}{q + 3.5 p_{sp}} \right)^{1/2} . \quad (\text{F-22})$$

The bias error propagation equation is,

$$B_V = \left[ \left( \frac{\partial V}{\partial q} B_q \right)^2 + \left( \frac{\partial V}{\partial T_0} B_{T_0} \right)^2 + \left( \frac{\partial V}{\partial p_{sp}} B_{p_{sp}} \right)^2 \right]^{1/2} . \quad (\text{F-23})$$

The partial derivatives are, (verified with perturbation method)

$$\begin{aligned} \frac{\partial V}{\partial q} &= \frac{V}{2} \left( \frac{1}{q} - \frac{1}{q + 3.5 p_{sp}} \right) \\ \frac{\partial V}{\partial T_0} &= \frac{V}{2T_0} \\ \frac{\partial V}{\partial p_{sp}} &= -\frac{3.5V}{2(q + 3.5 p_{sp})} . \end{aligned} \quad (\text{F-24})$$

To evaluate the uncertainty in velocity, the bias errors in two additional measurements are needed. First, the bias error in total temperature, based on manufacturer's specifications is  $\pm 1.8$  deg F. Second, the uncertainty in static pressure,  $p_{sp}$ , must be estimated by the error propagation technique since it is a calculated result.

$$p_{sp} = p_{sr} + k_1 \Delta p_r \quad (\text{F-25})$$

$$B_{p_{sp}} = \left[ \left( \frac{\partial p_{sp}}{\partial p_{sr}} B_{p_{sr}} \right)^2 + \left( \frac{\partial p_{sp}}{\partial k_1} B_{k_1} \right)^2 + \left( \frac{\partial p_{sp}}{\partial \Delta p_r} B_{\Delta p_r} \right)^2 \right]^{1/2} \quad (\text{F-26})$$

The partial derivatives are,

$$\begin{aligned} \frac{\partial p_{sp}}{\partial p_{sr}} &= 1 \\ \frac{\partial p_{sp}}{\partial k_1} &= \Delta p_r \\ \frac{\partial p_{sp}}{\partial \Delta p_r} &= k_1 \end{aligned} \quad (\text{F-27})$$

Then,

$$B_{p_{sp}} = \left[ B_{p_{sr}}^2 + \Delta p_r^2 B_{k_1}^2 + k_1^2 B_{\Delta p_r}^2 \right]^{1/2} \quad (\text{F-28})$$

### Evaluation—Endevco transducers

Bias errors for  $k_1$  and  $\Delta p_r$  were evaluated previously and are listed in Table F-2. The absolute pressure measurement,  $p_{sr}$  was made with a 15 psia Paroscientific pressure standard and has a bias error of 0.01% of full scale which translates to 0.0015 psi. Then,

$$U_{p_{sp}} = B_{p_{sp}} = 0.001521 \text{ psia}$$

$$U_V = B_V = 0.5549 \text{ ft/s.}$$

### Evaluation—PSI system

$$U_{p_{sp}} = B_{p_{sp}} = 0.001500 \text{ psia}$$

$$U_V = B_V = 0.1793 \text{ ft/s.}$$

### Reconstruction Errors

Finally, the reconstructed  $\Delta p_i$  values (Endevco data) have an error due to the reconstruction process. From the three proof of principal tests, it is estimated that the bias error in  $\Delta p_i$  is approximately 0.00020 and the precision error is 0.00066 (see Appendix D). For the reconstructed pressure data, the reconstruction process error is combined with measurement errors by the root-sum-squared method. As seen in Table F-2, the reconstructed pressure has essentially the same bias error as the basic data, but the precision error is twice that of the basic data. The uncertainty in the reconstructed pressures is approximately 25% greater than that for

the basic data. The uncertainty in reconstructed  $C_p$  values is calculated with the propagation equation just as it was for the basic data:

**Unaveraged  $C_p$ , windward side:**

$$S_{C_p} = 0.00923$$

$$B_{C_p} = 0.01891$$

$$U_{C_p} = \left\{ (0.01891)^2 + [(2)(0.00923)]^2 \right\}^{1/2} = 0.02643.$$

**Unaveraged  $C_p$ , leeward side:**

$$S_{C_p} = 0.00923$$

$$B_{C_p} = 0.01818$$

$$U_{C_p} = \left\{ (0.01818)^2 + [(2)(0.00923)]^2 \right\}^{1/2} = 0.02591.$$

These values are approximately 17% greater than the uncertainty for the basic  $C_p$  values.

**Averaged  $C_p$ , windward side:**

$$U_{\bar{C}_p} = \left\{ (0.01891)^2 + [(2)(0.0695)(0.00923)]^2 \right\}^{1/2} = 0.01895.$$

**Averaged  $C_p$ , leeward side:**

$$U_{\bar{C}_p} = \left\{ (0.01818)^2 + [(2)(0.0775)(0.00923)]^2 \right\}^{1/2} = 0.01824.$$

Since the largest difference is in precision error, which is reduced by averaging, the uncertainty in average  $C_p$  is essentially the same for both basic and reconstructed values.

## BIBLIOGRAPHY

Selected references for measurement uncertainty analysis are listed below.

1. R. B. Abernathy, J. W. Thompson, Jr., et al, *Handbook - Uncertainty in Gas Turbine Measurements*, AEDC-TR-73-5, Arnold Engineering Development Center, Feb. 1973. Also published as *Measurement Uncertainty Handbook*, Instrument Society of America, 1980.
2. American Society of Mechanical Engineers, *Measurement Uncertainty*, ANSI/ASME PTC 19.1-1985, April 1986.
3. American Society of Mechanical Engineers, *Measurement Uncertainty for Fluid Flow in Closed Conduits*, ANSI/ASME MFC-2M-1983, Aug., 1984.
4. American Institute of Aeronautics and Astronautics, *Assessment of Experimental Uncertainty With Application to Wind Tunnel Testing*, AIAA S-071A-1999.
5. H. W. Coleman and W. G. Steele, Jr., *Experimentation and Uncertainty Analysis for Engineers*, John Wiley & Sons, 1989.

## REFERENCES

- <sup>1</sup> E. L. Clark, "Uncertainty Estimates for Derivatives and Intercepts," Paper No. 91-061, *ISA 37<sup>th</sup> International Instrumentation Symposium*, San Diego, CA, May 5-9, 1991

## EXTERNAL DISTRIBUTION

- 5 D. D. McBride  
41 Rock Ridge Dr., NE  
Albuquerque, NM 87122
- 3 E. L. Clark  
9800 Karak Rd., NE  
Albuquerque, NM 87122
- 1 James C. Ross, MS260-1  
Experimental Physics Branch  
National Aeronautics and Space  
Administration  
Ames Research Center  
Moffett Field, CA 94035-1000
- 1 James T. Heineck, MS260-1  
Experimental Physics Branch  
National Aeronautics and Space  
Administration  
Ames Research Center  
Moffett Field, CA 94035-1000
- 1 Stephen M. Walker, MS260-1  
Experimental Physics Branch  
National Aeronautics and Space  
Administration  
Ames Research Center  
Moffett Field, CA 94035-1000
- 1 Prof. Christine Hailey, UMC4130  
Mechanical and Aerospace Engineering  
Utah State University  
Logan, UT 84322
- 1 Theo Knacke  
4609 Santa Lucia Dr.  
Woodland Hills, CA 91364

## SANDIA DISTRIBUTION

- 1 MS0841 9100 T. Bickel  
Attn: 9103 M. A. Robertson  
9113 W. L. Hermina  
9114 J. E. Johannes  
9116 E. S. Hertel  
9117 R. O. Griffith  
9120 H. S. Morgan  
9122 M. S. Garrett  
9124 D. R. Martinez  
9125 T. J. Baca  
9126 R. A. May  
9134 S. R. Heffelfinger  
9140 J. M. McGlaun  
9142 J. S. Peery  
9143 J. D. Zepper
- 1 MS0841 9100 C. W. Peterson  
1 MS0824 9110 A. C. Ratzel  
1 MS0834 9112 M. Prairie  
1 MS0834 9112 V. A. Amatucci  
1 MS0834 9112 S. J. Beresh  
1 MS0834 9112 J. F. Henfling  
1 MS0825 9115 W. H. Rutledge  
1 MS0825 9115 R. Brazfield  
1 MS0825 9115 L. D. Whinery  
5 MS0825 9115 W. P. Wolfe  
1 MS0836 9116 J. M. Nelsen, Jr.  
1 MS0824 9130 J. L. Moya  
1 MS0828 9133 M. Pilch  
1 MS0835 9141 S. N. Kempka  
1 MS0835 9141 A. A. Gossler  
1 MS0835 9141 G. F. Homicz  
1 MS0835 9141 J. H. Strickland  
1 MS9018 8945-1 Central Technical Files  
2 MS0899 9616 Technical Library  
1 MS0612 9612 Review & Approval  
Desk for DOE/OSTI